AXIAL COMPRESSION BEHAVIOUR OF REINFORCED CONCRETE COLUMNS WITH 3D-PRINTED CONCRETE AS PERMANENT FORMWORK

SUBAKARAN RAJENTHIRAKUMAR

A THESIS SUBMITTED TO THE FACULTY OF GRADUATE STUDIES

IN PARTIAL FULFILMENT OF THE REQUIREMENTS

FOR THE DEGREE OF MASTER OF APPLIED SCIENCE

GRADUATE PROGRAM IN CIVIL ENGINEERING

YORK UNIVERSITY

TORONTO, ONTARIO

August 2026

©Subakaran, 2026

Abstract

This study investigated the axial compressive behaviour of reinforced concrete columns using 3D-printed concrete (3DPC) as permanent formwork, focusing on load sharing among materials and 3DPC behaviour. It included three phases: Phase 1 assessed 3DPC material behaviour under compression using cubes and prisms saw-cut from a 3DPC wall, revealing isotropic compressive behaviour in the two tested directions through statistical analysis. The prism's strength was 21% lower than the cubes, with a modulus of elasticity differing by only 3%. Phase 2 compared the theoretical axial stiffness derived using the modulus of elasticity determined through cubes and prisms to the axial stiffness of 320 mm tall 3DPC cylindrical shell specimens. This resulted in an overestimate of axial stiffness by 73% and 79% for cubes and prisms, respectively, compared with the experimental axial stiffness determined from the load-deformation response of the cylindrical shells under uniaxial compression. Phase 3 examined small-scale circular columns (250 mm diameter, 240 mm height) and large-scale square columns (350 mm section width, 1040 mm height), with similar conventionally cast specimens made from the same concrete mix proportion. Due to the capacity of the hydraulic actuator used for the setup, the square columns were loaded to 1000 kN, while circular columns were tested to failure. The circular 3DPC columns maintained intact printed formwork up to failure but had compressive strengths 4.5% lower than cast-in-place columns, with 35% reduced initial axial stiffness compared with cast-in-place columns. Two print layouts for the square columns (47PC with 47% printed concrete and 60PC with 60% printed concrete) showed initial stiffness reductions of 47.5% and 45.4%, respectively, compared to control specimens. A modified fibre section model predicted axial load resistance and was validated against cast-in-place specimens, with a maximum error of 2.1%. Three constitutive models for printed concrete were evaluated, with the cylindrical shell model showing the most accuracy, yielding maximum errors of 8.1% for 47PC and 5.4% for 60PC. These findings indicate that 3DPC as permanent formwork is a viable alternative to conventional methods and remains structurally intact up until failure. Further investigations are recommended to validate the proposed model across the complete load–deformation response.

Acknowledgments

I would like to thank my supervisor and principal investigator, Dr Liam J. Butler, for the opportunity to conduct this research on 3D-printed concrete structures and for believing in my ability to complete this project successfully. I am also grateful for the guidance and assistance in defining my project objectives, for lending a hand during the experiment, for arranging group gatherings, and for support throughout my two years of study at York University. I would also like to thank my committee member, Dr Pantazopoulou, for sharing her knowledge not only in the two courses I took but also whenever I had questions or needed clarification about the research. I would like to acknowledge the industry partner Aretek for sponsoring this research and for allowing us to use the facility and printer to fabricate all the specimens.

My gratitude also goes to my co-team members, Buddhi, Osama, and Ryan, for their extensive help with the DFOS and data collection, as well as during preparation and testing. I am also deeply grateful to my friend and team member, Maryam, for her invaluable support, guidance, and help, and for the many hours we shared together in and out of the lab. Further thanks to the lab technicians, Riad Rajab and Kunjan Rupakheti, for all their assistance with experiments. I would also like to mention the friends I made, Pina, Karen, Nazareth, Pedro, Clearance, and Khayyam, who travelled with me during these years at York University.

Finally, my amma and appa for being supportive, understanding the pressure I went through, and being my backbone and moral support; my therapists and my best friends, for listening to my thesis issues without much understanding, and for helping me in every possible way since day one.

"Well, there are 5 billion people on this planet, and you're the perfect mom (and dad) for me. What are the odds of that?" – Young Sheldon

Table of Contents

Abstract ii

Acknowledgement iii

Table of Contents iv

List of Tables viii

List of Figures x

1 Introduction 1

1.1 Evolution of Additive Concrete Construction 1

1.2 Recent Developments on Additive Concrete Construction 2

1.3 Research Objectives 4

1.4 Structure of the thesis 5

2 Literature Review 7

2.1 Evolution of 3D Concrete Printing Technology 7

2.2 Characteristics of 3D Printed Concrete 9

2.2.1 Process Parameters 9

2.2.2 Interlayer Adhesion 9

2.2.3 Print Time Interval 10

2.2.4 Flowability and Pumpability 10

2.3 Mechanical Charecterization of 3D Printed Concrete 11

2.3.1 Compressive Strength of 3D Printed Concrete 11

2.3.2 Modulus of Elasticity of 3D Printed Concrete 14

2.4 Challenges in 3D Concrete Printing Technology 15

2.4.1 Layer reinforcements in 3DPC 16

2.4.2 Testing standards and design codes . . . 19
2.4.3 Incorporation of vertical reinforcement . . . 21
2.5 3D Printed Reinforced Concrete Columns . . . 23
2.6 Fibre Section Analysis . . . 27
2.6.1 Overview of Fibre Section Analysis . . . 27
2.6.2 Material Constitutive Models . . . 29
2.7 Digital Image Correlation . . . 31
2.8 Distributed Fibre Optic Sensors . . . 33
2.9 Summary of research gaps . . . 37

3 Mechanical Properties of 3DPC and Printed Cylindrical Shells 39
3.1 Introduction . . . 39
3.2 Experimental Plan . . . 40
3.2.1 Material and Concrete Printer . . . 40
3.2.2 Specimen Preparation . . . 41
3.2.3 Uniaxial Compressive Response and Modulus of Elasticity . . . 42
3.2.4 Uniaxial Compression Test – Cylindrical Shells . . . 45
3.3 Experimental Results . . . 46
3.4 Compressive Strength Test Results . . . 46
3.5 Modulus of Elasticity . . . 49
3.6 Compression test results of cylindrical shells . . . 50
3.7 Experimental Analysis . . . 52
3.7.1 Compressive Stress Results . . . 52
3.7.2 Statistical Analysis of Compressive Strength Results of Cubes . . . 52
3.7.3 Axial Stiffness – Experimental and Theoretical Estimate . . . 52
3.8 Discussion . . . 53
3.8.1 Variability in compressive strength . . . 53
3.8.2 Anisotropy and loading direction in cubes . . . 54

3.8.3 Behavior of prisms and cubes . . . 54
3.8.4 Axial stiffness of 3DPC shells . . . 54
3.9 Conclusion . . . 55

4 Axial Testing of Reinforced 3DPC Columns 57
4.1 3D-Printed Reinforced Concrete Column Design . . . 57
4.1.1 Square Reinforced 3DPC Columns . . . 57
4.1.2 Circular Reinforced 3DPC Columns . . . 60
4.2 Specimen Fabrication and Printing Parameters . . . 61
4.3 Instrumentation and Test setup . . . 64
4.3.1 Large-Scale Square Columns . . . 64
4.3.2 Small scale circular columns . . . 67
4.4 Experimental results and discussion . . . 68
4.4.1 Axial load response of small-scale circular columns . . . 68
4.4.2 Failure mechanism of circular columns . . . 71
4.4.3 Axial load response of large-scale square columns . . . 74
4.4.4 Strain distribution along the ties . . . 77
4.4.5 Strain distribution along the vertical reinforcing bars . . . 80
4.5 Summary and conclusions . . . 83

5 Fibre Section Analysis 86
5.1 Methodology . . . 86
5.2 Material Constitutive Models . . . 87
5.2.1 Discretization of cross-section and fibre sectional analysis . . . 90
5.3 Modelling Results and Discussion . . . 94
5.3.1 Estimation of accidental eccentric moments . . . 94
5.3.2 Comparison of experimental and predicted axial loads . . . 95
5.3.3 Estimation of load sharing . . . 100

5.4 Prediction of the ultimate axial capacity of the columns 101
5.5 Summary and conclusion 104

6 Conclusions and Future Work **105**
6.1 3DPC Material Behaviour 105
6.2 Behaviour of 3D printed concrete cylindrical shell 107
6.3 Reinforced 3D printed concrete columns 107
6.4 Future Directions 110

References **112**

Appendices **122**

A Design Calculation of Axial Load Resistance of Cast-in-Place Rectangular Column **122**

B Appendix 2: Design Calculation of Axial Load Resistance of Circular Cast-in-Place Column **124**

C Stress – Strain response of Hydro-Stone Gypsum Cement **127**

D Modified fibre section analysis for cast-in-place columns - MATLAB script **128**

E Modified fibre section analysis for 47PC printed columns - MATLAB script **135**

F Modified fibre section analysis for 60PC printed columns - MATLAB script **141**

G Potentiometer and load response of small circular columns **153**

List of Tables

2.1 The 28-day compressive strength and the modulus of elasticity obtained using the saw-cut samples of 3DPC in the same direction of orientation (Colyn et al., 2024) . 15

2.2 The compressive strength and modulus of elasticity values of printed and cast specimens tested in similar orientations (Huang et al., 2026) 15

2.3 Mix design constituents of the concrete (values are mass ratios to the binder except additives, which are g per kg of binder) (Marchment and Sanjayan, 2020) 18

2.4 The compressive strength and modulus of elasticity of the tested specimens in the two tested directions and comparison to the cast specimen 18

2.5 The available standards that are developed and published, and under development for 3D-printed concrete structures 19

2.6 The axial load obtained from the experimental testing of the columns and the simulation results along with the percentage difference, adapted from Nguyen-Van et al. (2026) 26

3.1 Mixture ratios of proprietary concrete mixture 41

3.2 Compression strength test results summary 48

3.3 Modulus of elasticity results 50

3.4 Summary statistics of compressive stress 52

3.5 Axial stiffness determined from the load-displacement response 53

4.1 Initial stiffness of the small-scale circular columns 71

4.2 Initial stiffness of the square columns was determined using the load-deformation response 76

5.1 Mechanical properties of specimens used to determine the constitutive model . . . 89

5.2 Predicted and experimental loads with the percentage error for the square cast concrete columns (CCC) 96

5.3 Predicted and experimental loads with the percentage error of the square columns using the cube stress-strain response (approach 1) as the printed concrete constitutive model 97
5.4 Predicted and experimental loads with the percentage error of the square columns using the cylinder stress-strain response (approach 2) as the printed concrete constitutive model 98
5.5 Predicted and experimental loads with the percentage error of the square columns using the shell stress-strain response (approach 3) as the printed concrete constitutive model 98
5.6 Percentage load contribution from infill concrete, 3DPC, and reinforcing bars towards the axial contribution obtained from fibre section model 101
5.7 Estimated axial load-carrying capacity using the fibre section model 103

List of Figures

2.1 (a) Working principle of contour crafting (the current 3D printing concrete) adapted from (Hwang and Khoshnevis, 2005) and (b) extruder and a mixer attached to a print head of the printing system used in this study, COBOD BOD2 8

2.2 Schematic of the definition of standoff distance referred in 3D printing concrete, adapted from (Panda et al., 2018) 10

2.3 Orientation of specimen and loading directions, adapted from Gu and Khayat (2024) 11

2.4 The pore structure distribution in 3D printed concrete with low- and high-quality printing and in the cast specimen, adapted from (Pham et al., 2020) 12

2.5 100 mm cubes sourced from a printed strip for compressive strength testing, adapted from (Wang et al., 2024) 13

2.6 (a) Schematic of the apparatus used to extrude micro cable during the printing process and (b) Different printing paths: Path A: Inclined deposition, Path B: Orthogonal deposition, and Path C: Rectangular deposition of micro cable, adapted from Ma et al. (2019) 17

2.7 (a) Schematic of the proposed methodology to penetrate reinforcing bars into printed layers at equal intervals; (b) Schematic of penetrating different lengths through equal layer thickness on a sandbed, adapted from (Marchment and Sanjayan, 2020) 22

2.8 (a) Final printed specimen with reinforcing bars placed perpendicular to the printed layers and (b) Broken sample with exposed macroscopic voids around the reinforcing bars, adapted from (Baz et al., 2020) 22

2.9 (a) Photograph of the square stirrup (b) Schematic of the printing process incorporating the stirrup in the middle of printing, adapted from (Chen et al., 2023) 24

2.10 (a) Different parametric print designs to obtain lightweight reinforced concrete 3DPC columns; (b) Different sections of the proposed reinforced concrete columns, adapted from Nguyen-Van et al. (2026) 25

2.11 Sequence of segmental construction of a pier, adapted from (Raza et al., 2024) . . . 27
2.12 Discrete fibre section mesh for the fibre section analysis 27
2.13 General procedure for the fibre section modelling 28
2.14 Stress-strain model for confined and unconfined concrete, adapted from Mander et al. (1988) 30
2.15 The elastic, perfectly plastic steel stress-strain constitutive model for steel 31
2.16 Constitutive materials of a typical distributed fibre optic cable, adapted from (Bai et al., 2022) 34
2.17 Schematic of the OFDR sensing principle of how the light travels through different components, adapted from (Tang et al., 2021) 35
3.1 (a) Cross-section and elevation of the 3DPC cylindrical shell; (b) 3DPC cylindrical shell 42
3.2 (a) Strain gauge shall be attached in the required position using the adhesive, (b) conducting wires shall be soldered to the conducting pins on the strain gauge, and (c) the connecting wires are soldered to the wire attached to the conducting pin . . 43
3.3 Compression loading setup of the printed concrete shells 45
3.4 Failure pattern of the cylinders tested under compression loading, which falls under category 2 as per ASTM standards 47
3.5 50 mm cube specimens tested in the direction perpendicular to the interlayer plane 48
3.6 Stress-strain response of the saw-cut cubes and the cast cylinders from the 3DPC and infill concrete mixture 49
3.7 Load-displacement response using the left, right, and average displacements. . . . 51
3.8 Failure pattern of the concrete shells under axial compression. 51
4.1 Elevation and cross-sections of all the reinforced concrete columns and the DFOS routing path 58

4.2 (a) Corner pieces attached along the vertical height of the formwork to support the sonotube from buckling and (b) the attached sonotubes to form the fillet corners of the cast concrete columns 59
4.3 The fully assembled formworks for the cast-in-place concrete with the additional supports in the lateral direction 60
4.4 (a) Elevation and cross section of cast-in-place circular column and (b) Elevation and cross section of reinforced 3DPC column 61
4.5 (a) Alignment jig fabricated to hold the reinforcing bars in exact positions for the small reinforcing bar cage and (b) completed circular reinforcing bar cage for the circular columns 62
4.6 (a) The facility where the specimens were ready to be printed with the plastic wrap on the floor and (b) the printed specimens 63
4.7 Process of fabricating the optimised reinforced 3DPC columns: (a) the first layer is printed, (b) ties are placed on the first layer, (c) layers are continuously printed while the ties are placed at the required spacing, and (d) the final 3DPC columns . . 64
4.8 (a) Epoxied DFOS cable to the vertical reinforcing bar, (b) Completed reinforcing bar cage for the square columns, and (c) the final infilled 3DPC columns with the protective sleeves for the DFOS to exit the columns 65
4.9 (a) Schematic of the test setup for the large column specimens (the potentiometer attached to the back is not shown in the schematic) and (b) the actual test setup . . 66
4.10 (a) Potentiometer attached to the circular column (b) the compression test setup with all the physical measuring devices 68
4.11 The schematic of the CONTROLS A52Z00 compression testing machine 68
4.12 Potentiometer measurement vs virtual potentiometer measurement and the percentage difference of VP measurement to potentiometer readings 69
4.13 Axial load vs overall shortening measured using the VP for both circular and 3DPC columns 70

4.14 Failure mechanism and crack propagation in cast circular columns under uniaxial compression loading 72
4.15 Failure mechanism and crack propagation in circular columns with 3DPC as permanent formwork 73
4.16 Post-failure state of the cast-in-place columns (a) CCC_1, (b) CCC_2, and (c) CCC_3 . 73
4.17 Post-failure state of the 3DPC columns (a) $3DPC_1$, (b) $3DPC_2$, and (c) $3DPC_3$ . . . 74
4.18 Images of the columns that were cut open to inspect any causes for reduced axial load capacity of the small-scale circular columns 75
4.19 Axial load - average displacement response of CCC, 47PC, and 60PC columns . . 75
4.20 Strain distribution around the tie placed at the mid height of column CCC_1 and the average strain values over the bonded length at each loading step 78
4.21 Strain distribution around the tie placed at the mid height of column CCC_2 and the average strain values over the bonded length at each loading step 78
4.22 Strain distribution around the tie placed at the mid height of 3DPC column $47PC_1$ and the average strain values over the bonded length at each loading step 79
4.23 Strain distribution around the tie placed at the mid height of 3DPC column $47PC_2$ and the average strain values over the bonded length at each loading step 79
4.24 Strain distribution around the tie placed at the mid height of the 3DPC column $60PC_2$ and the average strain values over the bonded length at each loading step . . 80
4.25 Strain distribution along the two diagonal vertical reinforcing bars in Cast Concrete Column (CCC_1) 81
4.26 Strain distribution along the two diagonal vertical reinforcing bars in $47PC_1$ 82
4.27 Strain distribution along the two diagonal vertical reinforcing bars in $47PC_2$ 82
4.28 Strain distribution along the vertical reinforcing bar of $60PC_2$ 83
5.1 Flowchart for the modified fibre section analysis 87

5.2 Schematic of the correction and new origin definition for the average load-deformation response of 3DPC cylindrical shells using the tangent drawn to the loading part of the 89
5.3 Stress-strain response of concrete obtained using shell, cube, and cylinder specimens for both infill and printed concrete 90
5.4 Meshconvergence analysis conducted for the fibre section model used in this study 91
5.5 The discretised fibre elements of each cast control specimen, standard permanent formwork concrete column, and optimised permanent formwork concrete column . 91
5.6 (a) the location of the potentiometers and the measured displacements and (b) a sample of the fitted strain plane through the strain values obtained from those potentiometers 92
5.7 Accidental eccentric moments in the x and y directions 95
5.8 Predicted and experimental load-deformation response of cast concrete columns (CCC) 99
5.9 Predicted and experimental load-deformation response of standard printed columns (SPC) 99
5.10 Predicted and experimental load-deformation response of optimised printed columns (OPC) 100
5.11 Uniaxial compression load-deformation response of cast-in-place (control) column obtained from the fibre section model 102
5.12 Predicted axial load vs displacement of the reinforced concrete columns using the fibre section model for concentric loading case 103
C.1 Average stress - strain response of hydrostone cement cylinders 127
G.1 Load and potentiometer response of cast-in-place column - specimen 3 (CCC1) . . 153
G.2 Load and potentiometer response of cast-in-place column - specimen 2 (CCC2) . . 154
G.3 Load and potentiometer response of cast-in-place column - specimen 1 (CCC3). This column was tested multiple times. 154

G.4 Load and potentiometer response of 3D printed column - specimen 1 (3DPC1) . . . 155
G.5 Load and potentiometer response of 3D printed column - specimen 2 (3DPC2) . . . 155
G.6 Load and potentiometer response of 3D printed column - specimen 3 (3DPC3) . . . 156

Chapter 1 Introduction

1.1 Evolution of Additive Concrete Construction

From ancient construction marvels like the Parthenon in Greece, Chand Baori in India, and the Great Wall of China, the construction industry has evolved over time, contributing approximately US$11.39 trillion globally in 2024 and is forecast to contribute US$16.11 trillion by 2030 (Deloitte, 2025). The construction industry, often called the "Backbone of the Economy" (Odoko et al., 2018), began as a labour-intensive, rudimentary task and has evolved into a modern industry through the development of engineered materials, mechanisation, digitisation, and automation.

The construction industry has begun to face critical issues due to a surging global population and rising demand for infrastructure in recent decades. Alsharef et al. (2024) identified the three biggest current challenges of the construction industry as a skilled labor shortage and an aging workforce (Akomah et al., 2020), disruptions in the supply chain of resources, including labor (Bolomope et al., 2025), and lastly, the slow integration and maturity of emerging technologies such as 3D printing, augmented reality, LIDAR, and Building Information Modeling (BIM). Other challenges in the construction industry include high labour costs (Baz et al., 2021), material waste, lack of on-site quality control, and limited architectural freedom (Baz et al., 2021). In addition, formwork represents a significant portion of construction costs. Formwork costs can account for 80–90% of total construction costs when formwork is not reused, and approximately 50% in typical projects (Nodehi et al., 2022; Ahmed, 2023).

Additive Concrete Construction (ACC), or 3D Concrete Printing (3DCP), began as a proof of concept, first explored by Pegna (1997), who laid the foundation for today's industry. The study involved selectively depositing cementitious material on a sand bed to form masonry blocks. The study not only demonstrated the feasibility of additive manufacturing using cement mortar, but material testing of the bulk material also revealed anisotropic behaviour, which had not been reported

previously. Following these initial findings, Khoshnevis (2004) further explored automation in construction and its applications. The application of automation in 3D printing was explored using a printer designed for ceramic paste extrusion with attached trowels to obtain a smooth finish, and the very first explorations of using coil reinforcements during extrusion to improve the tensile strength of the printed structures.

1.2 Recent Developments on Additive Concrete Construction

3DCP-related research can be broadly grouped into two primary branches: one focusing on the structural performance of 3D-printed concrete (3DPC), and the other dedicated to process parameters and material optimisations to ensure reliable extrusion and post-print properties. For clarity in this thesis, 3DPC refers specifically to the printing process, whereas 3DPC refers to the resulting printed concrete. These parallel research streams have identified many practical benefits of this evolving material technology, with recent studies estimating that construction waste could be reduced by up to 60%, production time by up to 70%, and labour costs by up to 80% (Nodehi et al., 2022), thereby positioning 3DCP as an alternative solution to construction industry challenges such as labour shortages, project delays, and material inefficiency.

Despite the proven feasibility of 3DCP technology, it faces challenges. Some of these gaps have been addressed in recent studies, while others require further systematic investigation. From a fabrication standpoint, critical process parameters including print speed, interlayer interval time, standoff distance, nozzle design and geometry, early-age strength and stiffness, and pumpability have been identified as primary influencers of both print quality and the resulting mechanical properties of 3DPC. Although numerous researchers have developed recommendations and optimisation frameworks for these parameters to achieve stable printing and optimal post-print performance, a key limitation persists. These values depend heavily on the specific print system and material composition used in those studies, which complicates direct scalability and standardisation across systems (Taborda-Llano et al., 2025).

From a structural engineering perspective, recent work has increasingly proposed 3DPC as an innovative permanent formwork solution for load-bearing elements, in which forms are printed and then infilled with concrete and steel reinforcement. Applications have included walls (Delavar et al., 2024), beams (Wang et al., 2025), and columns (Zhu et al., 2021), with examples spanning academia and industrial-scale projects. These applications address key issues related to traditional formwork, including costs of up to 60% of the construction cost of reinforced concrete structures (Menon and Varghese, 2018) and up to 60% of construction time (Perng et al., 2005). Meanwhile, these applications leverage 3DPC's ability to create complex geometries and freeform construction practices. Although the 3DPC is used to fabricate permanent formwork for the infilled structural elements, the 3DPC and infilled concrete together behave as a composite structure to resist loads.

Meanwhile, the current literature (at the time of writing this thesis) includes only a limited number of studies that have explored 3DPC as a permanent formwork for reinforced concrete columns. Six studies were found to use 3DPC as permanent formwork for reinforced concrete columns. Zhang et al. (2023) conducted an experimental study on segmental columns fabricated with 3DPC as permanent formwork, stacked to a total height of 1800 mm, focusing mainly on the cyclic behaviour of post-tension columns fabricated with 3DPC compared with traditional segmental reinforced concrete columns. Silfwerbrand (2024b) studied the form pressure induced by infill concrete on the permanent formwork and extended the study to understand the compression behaviour of 3DPC permanent formwork columns infilled with self-consolidating concrete, comparing the performance against cast-in-place self-consolidating reinforced concrete columns. The results indicate that composite reinforced concrete columns using 3D-printed concrete as permanent formwork can resist the full hydrostatic pressure developed during casting without leakage or crack development. Liu et al. (2025) studied the effect of confinement on the strength of short columns by embedding carbon fibres in the printed layers, and Chen et al. (2023) conducted experimental and numerical studies on square columns 3D-printed using coarse aggregate as the permanent formwork and infilled with conventional concrete. None of these studies proposed a design methodology that could be widely adopted.

Despite this, to understand the composite behaviour of reinforced concrete columns using 3DPC as permanent formwork and to propose a rational design method, it is essential to understand the material behaviour. Several studies have concluded that measuring the mechanical properties of 3DPC using cast specimens and methods developed for cast or conventionally produced concrete often overpredicts its actual mechanical performance owing to the material's layered structure (Yerikania et al., 2025)(Yerikania et al., 2025). Many studies, including the first ever recorded 3DPC study by (Pegna, 1997), reported anisotropic behaviour because of the layer-by-layer nature of 3DPC (Marchment and Sanjayan, 2019, 2020; Singh et al., 2023).

This study focused on improving understanding of 3DPC material behaviour by proposing and evaluating specimens extracted from printed structures to better represent its intrinsic behaviour. In particular, compressive strength and elastic modulus of 3DPC were evaluated. The mechanical properties of extracted specimens were tested and compared with those of 3DPC shells printed with the same mixture proportions and printing parameters. Following this, full-scale columns (based on cross-sectional dimensions) with 3DPC as permanent formwork were tested under service loads (i.e., not to failure) to assess the relative contributions of the 3DPC, infill concrete, and reinforcing steel to the axial load. Based on these tests, models were developed and compared with both code-based equations and past studies in the literature.

1.3 Research Objectives

Although multiple studies have examined various aspects of 3DPC, few have critically evaluated the methodology used to determine the modulus of elasticity. Furthermore, most research on 3DPC has been conducted using lab-scale 3D printers, and few studies have examined the behaviour of large reinforced concrete columns printed with commercial printers. In addition, quantifying load sharing among the 3DPC, infill concrete, and vertical rebars would help develop models to estimate the load-carrying capacity of axially loaded reinforced-concrete 3DPC columns.

Based on the gaps identified in the current state-of-the-art, the research conducted as part of this

MASc thesis has several objectives:

Objective 1 - To propose specimens that could be extracted from 3DPC structures to represent the intrinsic behaviour of 3DPC material and to recommend a specimen geometry that better estimates the mechanical properties such as compressive strength and modulus of elasticity of printed structures, while also evaluating the anisotropic behaviour reported in the literature.

Objective 2 - To establish a relationship between the initial stiffness values obtained from load–deformation curves of 3DPC cylindrical shell specimens and the theoretical axial stiffness obtained from modulus of elasticity measurements on cube and prism specimens.

Objective 3 - To understand the behaviour of reinforced 3DPC columns under uniform compression loading and to compare the performance to similar cast-in-place reinforced concrete columns.

Objective 4 - To compare the structural behaviour (under service loading) of different square 3DPC column designs fabricated using similar concrete mixture proportions and reinforcement ratios. This research study utilised a Distributed Fibre Optic Sensor (DFOS) to capture the strain distribution along the vertical reinforcing bars and stirrups, as well as in the printed layer.

Objective 5 - To establish a model for reinforced 3DPC columns to predict the load sharing between the 3DPC, infill concrete, and steel reinforcement under uniaxial loading at different load levels and to validate the model using experimental data.

1.4 Structure of the thesis

Chapter 2 presents the literature review conducted for this research study, which includes the background and presents the available knowledge based on current studies on 3DCP, current explorations of reinforced 3DPC columns, reinforcement methodologies for columns, instrumentation techniques for proper data collection, available standards and methodologies for material characterisation tests, and fibre section analysis for concrete elements.

Chapter 3 presents the characterisation of 3DPC materials using two proposed specimen types to determine the modulus of elasticity and compressive strength of 3DPC and to evaluate its behaviour under compression loading, primarily to assess anisotropy and the consistency of the test methodology.

Chapter 4 describes the experimental methodology and specimen preparation for the small-scale circular and large-scale square reinforced concrete columns. It then presents and discusses all experimental results collected during testing of the small and large columns.

Chapter 5 describes the formulation of a fibre section analysis conducted in this research study, including the constitutive material models used for the infill concrete, 3DPC, and vertical steel reinforcing bars. Finally, it presents all fibre-section results and analyses and discusses the comparison between predictions and experimental test results.

Chapter 6 presents the results of the Distributed Fibre Optical Sensor (DFOS) measurements, which were used to capture the evolution of longitudinal and transverse strains during the large-scale column tests. This chapter compares the distributed strain behaviour of the 3DPC columns with that of conventional cast-in-place (control) columns.

Chapter 7 presents the summary of the conducted research study and the conclusions drawn from the data collected and analysed. This chapter also presents recommended future studies to formulate and validate the model, develop rational design procedures to guide practitioners in designing column sections, and extend the proposed model to other column designs not considered in this study.

Chapter 2 Literature Review

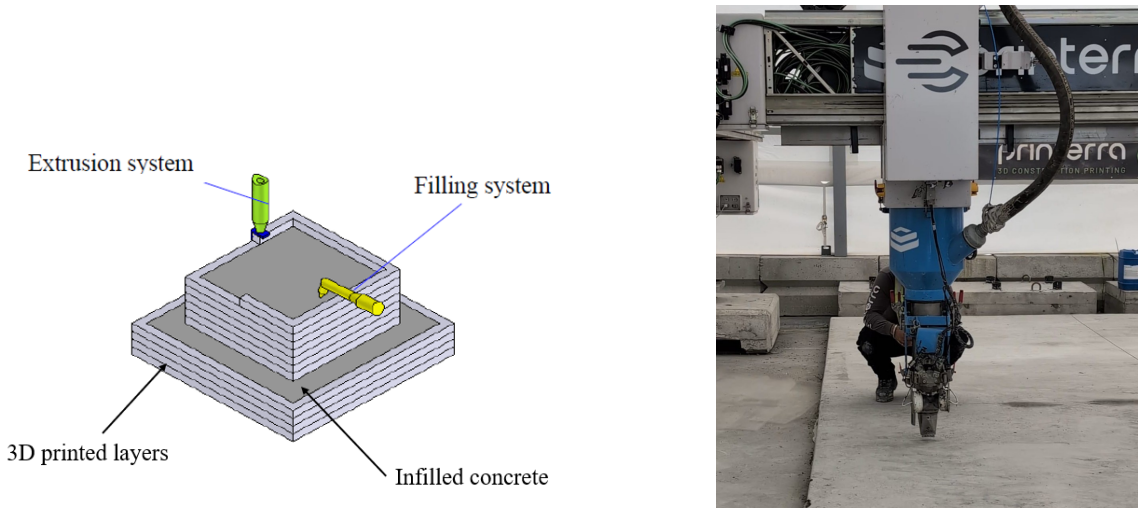
This literature review begins by introducing the growing 3D printing concrete technology and its fundamental working principle, followed by the characteristics of 3D-printed concrete and how it differs from traditional concrete construction technology due to the interlayers introduced during the printing process. The review also covers current studies on reinforced concrete columns fabricated using this technology to identify the state of the technology for fabricating such load-bearing columns and the gaps in the studies. In addition, this chapter outlines the working principles and analysis methods used in this study and concludes with the identified gaps.

2.1 Evolution of 3D Concrete Printing Technology

The earliest form of 3D-printed concrete (3DPC) dates back to 1997, using selective deposition of sand and cement, which were then activated by steam to form masonry bricks. Some prototypes smaller than one metre in length were printed; however, studies conducted in 1997 and later focused on larger prototypes, which became the cornerstone of future innovations in 3DCP (Pegna, 1997).

The construction industry has lagged in adopting automation and technology. As a result, the industry faced multiple issues, such as low labour efficiency, high safety concerns and on-site accident rates, and an inability to control on-site quality. In 2004, with the development of Contour Crafting (CC) as a new branch of additive manufacturing, printing concrete became feasible at the industrial level and began to address industry issues (Khoshnevis, 2004). CC utilised a two-stage system in which one extrudes the outer layer, which acts as structural formwork, while the other extrudes the infill, which is filled with concrete. A simplified working principle of CC is shown in Figure 2.1.

The extruder and a mixer attached to the nozzle head of the gantry-type printer, COBOD BOD2, which is used in this study, are shown in Figure 2.1b and can print support-free free-form constructions. This development in nozzle design enables continuous 3D printing by depositing cementi-



(a) (b)

Figure 2.1: (a) Working principle of contour crafting (the current 3D printing concrete) adapted from (Hwang and Khoshnevis, 2005) and (b) extruder and a mixer attached to a print head of the printing system used in this study, COBOD BOD2

tious material layer by layer and is being explored as an alternative concrete construction technique in the industry. To date, two printing systems are used: 1-component (1K) and 2-component (2K). In the 1K system, the material is mixed prior to being transported to the nozzle, whereas in the 2K system, it follows a similar procedure to the 1K system, but additionally, there is another mixing process of admixtures to the concrete mixture that happens before the material is extruded out of the nozzle. The 2K system exacerbates material-related challenges in buildability and workability (Farra et al., 2024; Dahlenburg et al., 2022), which are discussed later in this chapter.

A few of the advantages of 3DCP are that it reduces the need for formwork in reinforced concrete structures (Ahmed, 2023), automates the process with higher precision and accuracy (Zhang et al., 2019), offers geometric flexibility and freeform construction (Perkins and Skitmore, 2023), and can improve the sustainability of concrete mixtures (Hager et al., 2016; Mim et al., 2025; Panda et al., 2017).

Meanwhile, researchers have explored the use of 3DPC as a permanent formwork for reinforced concrete columns (Chen et al., 2023; Nguyen-Van et al., 2026; Phadnis et al., 2020; Raza et al., 2024; Bates and Aslani, 2025), beams (Wang et al., 2024, 2025), and structural wall elements

(Delavar et al., 2024; Silveira et al., 2024; Wolfs et al., 2018).

2.2 Characteristics of 3D Printed Concrete

2.2.1 Process Parameters

3DPC poses unique challenges, including poor inter-layer adhesion, shrinkage due to the lack of coarse aggregates, nozzle blockage, cold joint formation, void content and distribution, and rheological properties. To print effectively and avoid these challenges in 3DPC, it is essential to precisely control process parameters such as inter-layer interval time, standoff distance, printing speed, and nozzle diameter, and to select appropriate printing paths, nozzle designs, and shapes (Pan et al., 2023; Sahin and Mardani, 2023; Singh et al., 2023).

2.2.2 Interlayer Adhesion

One of the key issues discussed in various studies on 3DPC is interlayer adhesion. This adhesion determines the degree of monolithic behaviour of the printed structures. Among the many factors that affect adhesion, several studies have investigated the effect of standoff distance. Standoff distance is the height at which the nozzle prints relative to the bottom (printed) layer, not the printing layer. For example, setting the nozzle height (standoff distance) to 10 mm would result in 10 mm-thick layers (Baz et al., 2020). According to Bos et al. (2016), setting the standoff distance equal to the width of the nozzle would result in smooth deposition of the print filament and avoid (pressure) interaction between the filament and the print head. In a study by Panda et al. (2018) assessing the effect of standoff distance, 0 mm, 2 mm, and 4 mm were selected as alternatives (see Figure 2.2). The tensile bond strength test was carried out using a dual-column tensile test machine under direct tension, and the results show a significant reduction as the standoff distance increases, attributed to the interlayer adhesion strength developed at different standoff distances.

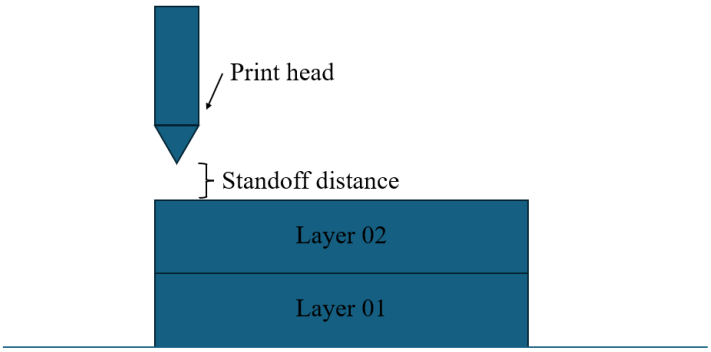


Figure 2.2: Schematic of the definition of standoff distance referred in 3D printing concrete, adapted from (Panda et al., 2018)

2.2.3 Print Time Interval

Print time interval is another process parameter that affects the interlayer adhesion strength of 3DPC. The study aimed to evaluate the effect of the delay time between two concrete layers at 10-, 20-, and 30-minute intervals. Uniaxial tensile strength, a representative of interlayer adhesion, showed that concrete printed at 10- and 30-min intervals had higher adhesion than at 20 min. However, the reason for this pronounced behaviour was not identified until concrete bleeding was observed on printed layers. Concrete bleeding is a phenomenon in which excess water rises to the surface in fresh concrete. Experiments were conducted to measure surface moisture content at corresponding delay times. The experiments showed that bleeding in concrete is directly correlated with interlayer adhesion.

2.2.4 Flowability and Pumpability

Flowability and pumpability of the concrete is based on the amount of water in the cement or concrete mixture, which determines the ability of the concrete to spread on its own and through experiments, it has been observed that this influences the mechanical properties and porosity in the printed concrete mixture, whicle pumpability is the ability of the concrete to be pumpd through the hoses to be delivered via the nozzles. Extrudability is another property very similar to pumpability, but it assesses the concrete's ability to be extruded through a nozzle without disruption. A visual

difference in the quality of extrudability, from limited tears to increased density of tears in the printed concrete for different concrete mixtures, is shown in Figure 2.3, which is observed in a study conducted by Gu and Khayat (2024).

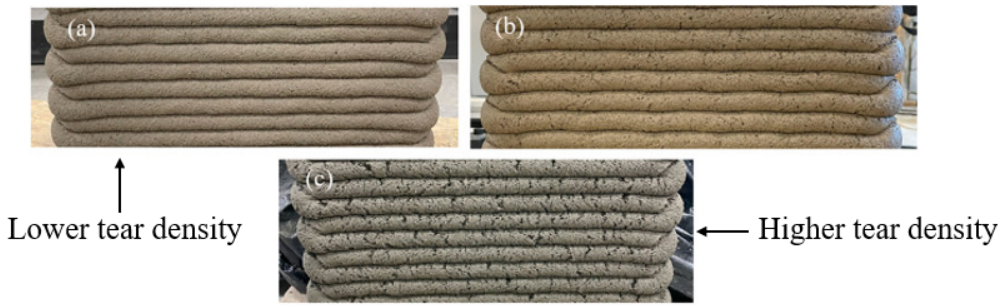


Figure 2.3: Orientation of specimen and loading directions, adapted from Gu and Khayat (2024)

2.3 Mechanical Charecterization of 3D Printed Concrete

2.3.1 Compressive Strength of 3D Printed Concrete

Most published studies on 3DPC have evaluated compressive strength, as it remains one of the most crucial parameters in concrete structural design. However, because of the many variables in the printing process and the rapid early-age strength development of 3DPC, compressive strengths often vary between cast-in-place and printed specimens (Zhang et al., 2024). In addition, recent studies aimed at understanding the root cause of anisotropic behaviour have shown that the printing process introduces distinct porosity characteristics at interlayer interfaces compared with those within a single deposited filament.

Pham et al. (2020) studied the effects of different steel fibre lengths (3 mm and 6 mm) and volume fractions on the mechanical properties of 3DPC. Compressive strength tests on cast specimens fabricated with 3 mm steel fibres showed an 8 to 22% increase, and those with 6 mm steel fibres showed a 17 to 26% increase. They also found that porosity, measured by micro computed tomography (CT), was inversely correlated with fibre volume content. They also reported that porosity depends on print quality and that high-quality printing can yield lower porosity than in cast concrete

specimens, as shown in Figure 2.4.

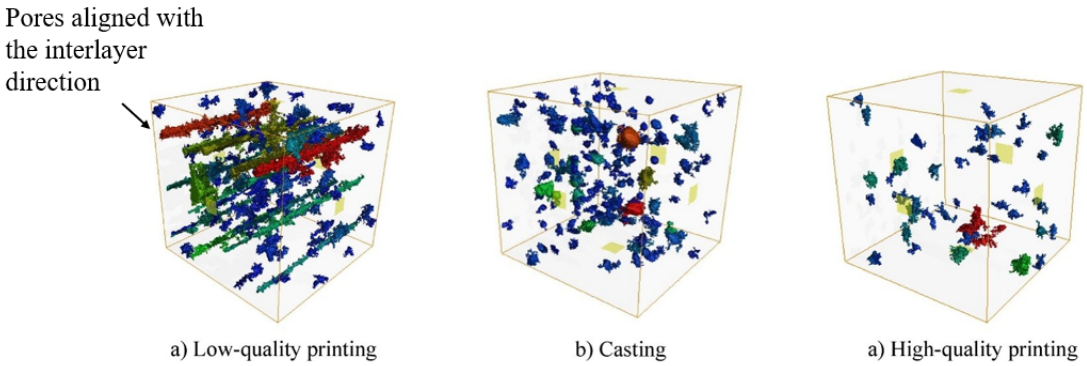


Figure 2.4: The pore structure distribution in 3D printed concrete with low- and high-quality printing and in the cast specimen, adapted from (Pham et al., 2020)

Du et al. (2023) reported that the interlayer regions exhibit approximately 10% higher porosity than the bulk material, which, in turn, leads to a 20% reduction in shear strength in both the horizontal and vertical directions. Similarly, Liu et al. (2022), using X-ray computed tomography (X-CT), demonstrated that the pore structure in the interlayer regions of 3DPC is distinct from that in cast concrete. This non-uniformity was shown to induce stress concentrations and reduce overall mechanical performance. Furthermore, their results indicated significant anisotropic behaviour in compressive strength when testing 100 mm cubes extracted from printed strips in different orientations. Notably, the tested specimens exhibited visible interlayer divisions, as shown in Figure 2.5.

Many studies have investigated the compressive behaviour of 3DPC and have consistently reported differences between printed and cast-in-place concrete. Lee et al. (2019) evaluated the mechanical properties of 3DPC and found that the compressive strength measured from cast-in-place specimens was approximately 30% higher than that of specimens extracted from printed concrete. However, no significant difference was observed between cube and cylinder specimens extracted from the printed elements. These findings suggest that the printing process itself, rather than the specimen geometry, has a greater influence on the measured compressive strength.

In addition to the reduction in compressive strength, considerable attention has been given to the

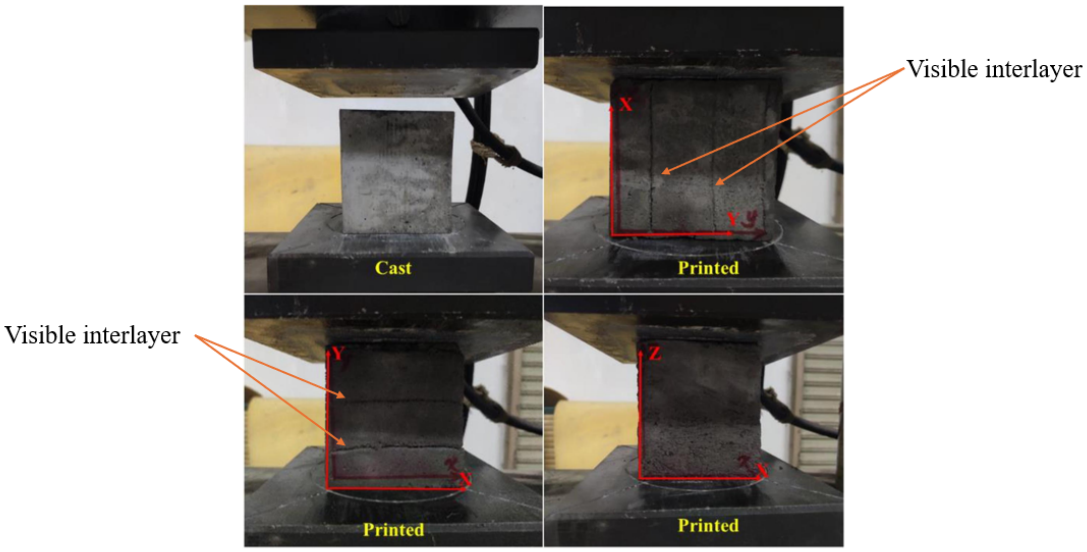


Figure 2.5: 100 mm cubes sourced from a printed strip for compressive strength testing, adapted from (Wang et al., 2024)

anisotropic behaviour of 3DPC arising from the layer-by-layer deposition process. Many studies have reported that the inter-layer bond characteristics and printing direction influence the mechanical response of printed concrete. However, contradictory findings also exist, with some researchers reporting comparable compressive strengths in all three principal directions (Panda et al., 2019). These inconsistencies indicate that the influence of printing direction on compressive strength is not yet fully understood. Interestingly there are also studies where higher compressive strengths were observed from tested 3D printed specimens compared to the cast in place counterparts, In the research conducted by Huang et al. (2026), at room temperature of 20°, the compressive strengths of prisms of dimension 100 mm x 100 mm x 300 mm were found to be ∼4% higher than the cast in place prism. In another study Zhang et al. (2021b), the compressive strengths of printed concrete were often higher than those of mould-cast specimens, by as much as ∼31% and as little as ∼6%.

To better understand these conflicting observations, Zhang et al. (2024) conducted a comprehensive review of compressive strength data reported in the literature for 3DPC and compared them with data for cast-in-place concrete. In their study, the x-, y-, and z-directions were defined as parallel to the printing direction, perpendicular to the vertical plane, and perpendicular to the horizontal

plane, respectively. Because standardised testing procedures for 3DPC are lacking, previous studies used widely varying specimen sizes and testing methods. To enable meaningful comparisons, the reported strengths were normalised using the compressive strength of cast-in-place specimens. The review showed that the normalised compressive strengths of 3DPC at both 7 and 28 days were generally lower than those of cast-in-place concrete. Nevertheless, several studies reported compressive strengths that exceeded those of cast-in-place concrete by up to 20%, further highlighting the variability in the reported behaviour of 3DPC (Zhang et al., 2024).

More recent studies have focused on identifying the factors responsible for this variability. For example, Saelens et al. (2026) reported that increasing the time interval between successive layer depositions increases porosity, alters the pore morphology, and consequently reduces the mechanical properties of 3DPC. Since the interval between deposited layers varies considerably among printing systems, ranging from approximately 10 minutes to as long as 4 hours, substantial differences in material properties can be expected. Their experimental investigation further showed that, irrespective of the printing system (1K or 2K), compressive strength was largely independent of the loading direction but exhibited a relatively high coefficient of variation, ranging from 7.6% to 25.2% across the tested specimens. The accumulation of larger pores within the printed material was identified as a likely contributor to the observed reduction in compressive strength.

2.3.2 Modulus of Elasticity of 3D Printed Concrete

Colyn et al. (2024) explored the use of fly ash, silica fume, and slag as alternative binders to reduce the proportion of Ordinary Portland Cement (OPC), thereby making a more sustainable 3D-printed concrete mixture that also meets the requirements for optimal printing quality. Cylindrical specimens, 140 mm in height and 70 mm in diameter, were cored from a printed structure with multiple vertical and horizontal layers. The modulus of elasticity was determined using the recommended procedure in EN 12390–13, a standard test for determining the secant modulus of elasticity of hardened concrete under compression. The modulus of elasticity of the concrete mixtures tested in this study, along with the 28-day compressive strength, which was also determined using specimens

similar to those used for the modulus of elasticity tests, are given in the following Table 2.1.

Table 2.1: The 28-day compressive strength and the modulus of elasticity obtained using the saw-cut samples of 3DPC in the same direction of orientation (Colyn et al., 2024)

Specimen	Compressive Strength (MPa)	Modulus of Elasticity (GPa)
50FA10SF	31.1	36.6
40FA20MK60	37.9	31.6
60GGBS	43.1	31.3

Huang et al. (2026) investigated the degradation of compressive strength and modulus of elasticity in 3DPC materials as temperature increased. To determine the mechanical properties, prism specimens measuring 100 mm x 100 mm x 300 mm were saw-cut from a printed structure. The modulus of elasticity test was conducted in accordance with the recommendations of ASTM C469/469 at a loading rate of 0.5 MPa/s. However, the modulus of elasticity was determined from the slope of the secant line between 10% and 40% of the tested specimen's compressive strength. The compressive strength and the modulus of elasticity for similar orientations at 20° are given in Table 2.2.

Table 2.2: The compressive strength and modulus of elasticity values of printed and cast specimens tested in similar orientations (Huang et al., 2026)

Specimen/testing direction	Compressive strength at 20°C (MPa)	Elastic modulus at 20°C (GPa)
C	45.5	35.5
X	47.5	31.5
Y	47.0	27.5
Z	41.5	24.0

2.4 Challenges in 3D Concrete Printing Technology

Even though 3DPC technology has partly eliminated one of the major costs in construction, namely labour and formwork, and has reduced accident rates, improved quality control, reduced material waste, and increased design freedom, it still presents its own set of challenges. One major challenge in 3D printing technology is incorporating reinforcements to enhance tensile capacity. (Sahin and Mardani, 2023).

2.4.1 Layer reinforcements in 3DPC

Multiple studies have focused on techniques for incorporating reinforcements to improve the tensile characteristics of 3DPC and enhance its ductility (Ma et al., 2019). This is achieved using materials such as chains, nails, reinforcing steel, fibres, wires, and meshes. Reinforcing concrete has been categorised into two broad topics: reinforcing before or during the printing and reinforcing after printing (Chen et al., 2023). The reinforcing after printing is generally referred to as lowering the reinforcing cage into the printed permanent formwork.

Short Glass fibres were experimentally tested as a reinforcement option by Panda et al. (2017). Fibres of 3mm, 6mm, and 8mm were added at different ratios, with a maximum limit of 1 to prevent clogging and ensure continuous extrusion from the nozzles. This study found a marginal increase in compressive strength; however, flexural and tensile strength showed good improvements. Further, the researchers recommend exploring the directional properties of the fibres and their correlation with mechanical properties.

Extruding cables and chains during printing has been explored as a viable solution for incorporating reinforcements. Ma et al. (2019) experimented with a micro cable with a diameter of 1.2mm extruded along with the concrete. Figure 2.6a shows a schematic of the printing apparatus, and Figure 2.6b shows the different printing paths used in the research.

Based on the tests conducted, incorporating cables significantly increased the specimens' flexural capacity. It was also observed that depositing cables at an angle (Path A), as shown in Figure 2.6b, has flexural strengths that are 48.9% and 200% higher than those of Paths B and C, respectively (Ma et al., 2019).

Similarly, Bos et al. (2017) investigated fishing line and steel wire with diameters of 0.35mm and 0.4mm, respectively. However, initial investigations showed that they were too small and were pulled out of the concrete under load. Later, the researchers experimented with chains as an alternative; however, it was evident that concrete with no slump would not fill all the gaps between the

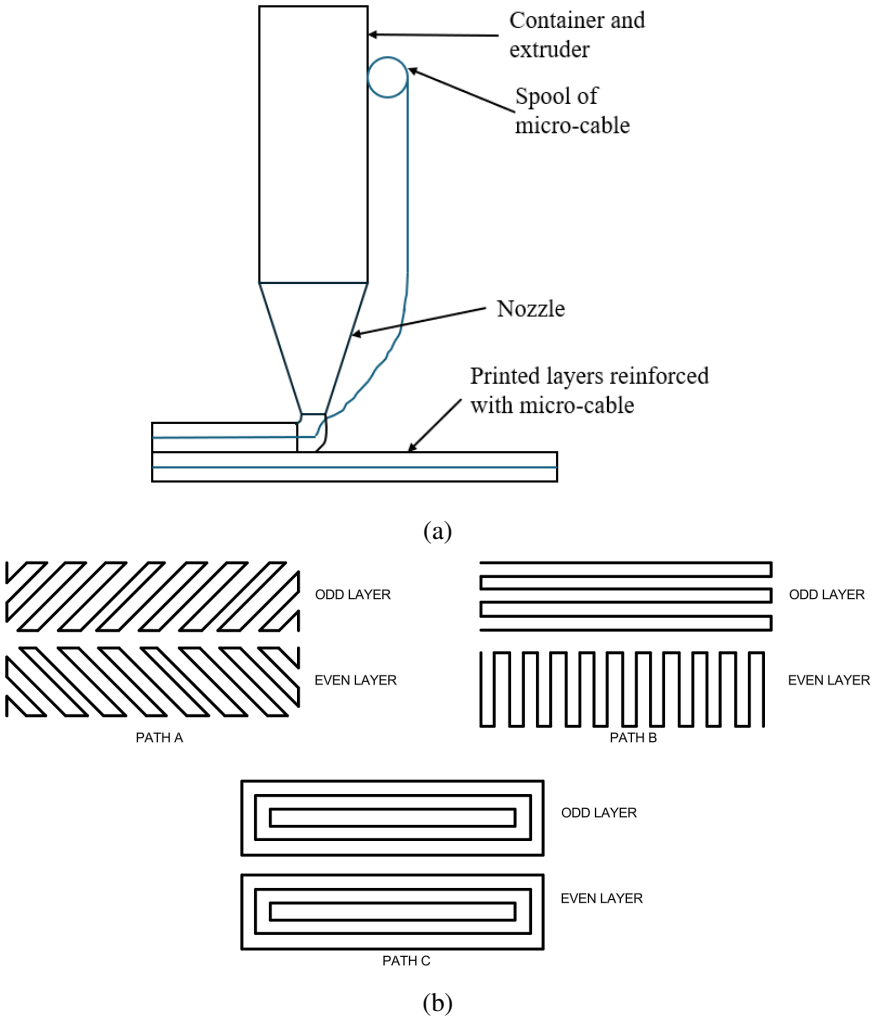


Figure 2.6: (a) Schematic of the apparatus used to extrude micro cable during the printing process and (b) Different printing paths: Path A: Inclined deposition, Path B: Orthogonal deposition, and Path C: Rectangular deposition of micro cable, adapted from Ma et al. (2019)

links. Finally, three different types of cables with diameters 0.63mm, 0.97mm, and 1.20mm were tested and results showed that incorporating cables would increase the strength characteristics of the printed concrete, however, further studies should be done to investigate possibilities of achieving failure without cable slips especially the cable with diameter 0.97mm and 1.20mm as it was seen that the lower diameter cable would not be a practically feasible solution for active reinforcing during printing.

The mix ratio used for concrete production in this experiment is given in Table 2.3. 160mm x

40mm x 40mm samples were used for the flexural and compression tests. In addition, a pullout test and yield strength were measured.

Table 2.3: Mix design constituents of the concrete (values are mass ratios to the binder except additives, which are g per kg of binder) (Marchment and Sanjayan, 2020)

Binder (1)			**Sand (1.5)**		**Water (0.3)**	**Additives**		
OPC	SF	FA	Sand 1	Sand 2		SP	RT	NC
0.8	0.1	0.1	1.0	0.5		2	3	3.4

The study showed results that were quite at odds with those of other studies conducted in the domain of 3DPC. Flexural test results showed that the cast-in-place concrete (control specimen) and the printed specimen performed; in fact, the printed specimen performed significantly better than the cast-in-place specimen. Compression test specimens showed near-isotropic behaviour in the perpendicular and lateral directions. The flexural and compression test results extracted from the research study are provided in Table 2.4.

Table 2.4: The compressive strength and modulus of elasticity of the tested specimens in the two tested directions and comparison to the cast specimen

Specimen Orientation	**Flexural Strength (MPa)**	**SD (MPa)**	**Compressive Strength (MPa)**	**SD (MPa)**
Cast	8.2	~ 0.9	64	~ 3.5
Perpendicular	7.3	~ 0.6	43	~ 3.8
Lateral	8.6	~ 0.3	38	~ 5.0

Pull-out test results at the actual penetration depth show that the pull-out resistance is similar to that of cast-in-place concrete at 40mm, but it decreases drastically with increasing penetration depth. The test results also showed cavity formation around the reinforcing bars due to particle disturbance during penetration. Due to cavity formation, the bond strength along the element's length (from bottom to top) has decreased. Future research should explore ways to provide continuous reinforcement for 3DPC elements (Marchment and Sanjayan, 2020).

2.4.2 Testing standards and design codes

Because 3DPC is an emerging discipline and research studies use a variety of printing systems and concrete mixtures, robust standards similar to those for reinforced or prestressed concrete have not yet been developed. However, to the best of the author's knowledge, a few standards related to 3DPC have been identified, and their scope is provided in Table 2.5.

Table 2.5: The available standards that are developed and published, and under development for 3D-printed concrete structures

Developed Standards or Standards under development	**Scope of the standard**
UL 3401:2022 – Outline of Investigation for 3D Printed Building Construction (UL LLC, 2022)	Covers evaluation of 3D-printed building elements and structures manufactured using additive manufacturing processes. Provides technical information to verify compliance with applicable building codes, regulations, and standards. Reports document manufacturing consistency, test ratings, material properties, durability, and performance. Includes evaluation of 3D-printed structural and non-structural building components (e.g., electrical enclosures and conduits). Does not assess structural design code compliance; tested material properties may support structural calculations. Excludes 3D-printed products unrelated to buildings or structures.

Continued on next page

Developed Standards or Standards under development	Scope of the standard
ISO/ASTM 52939:2023 – Additive Manufacturing for Construction Qualification Principles: Structural and Infrastructure Elements (International Organization for Standardization and ASTM International, 2023)	Covers quality assurance requirements for additive construction (AC) projects using additive manufacturing techniques. Requirements are independent of materials and processes but exclude metal-based additive manufacturing. Defines criteria for qualifying additive construction processes, quality-related characteristics, and system operation factors. Applies to load-bearing and non-load-bearing structural and infrastructure elements for residential and commercial applications. Establishes activities, sequences, and requirements within the additive construction site (AC cell) and project workflow. Does not address structural design approval, material property characterisation, or mechanical testing requirements.
ICC 1150:2025 (Draft) – Standard for 3D Automated Construction Technology for 3D Concrete Walls (International Code Council, 2025)	Provides structural criteria applicable to 3D automated construction technology and 3D concrete walls, including interior and exterior walls with and without steel reinforcement.

Continued on next page

Developed Standards or Standards under development	Scope of the standard
ACI CODE-ITG-12 Additively Constructed Concrete Walls for Residential Construction — Code Requirements and Commentary (Under development and out for public comments)key issue	Provides minimum requirements for the materials, design, and construction of additively constructed concrete walls (ACCW) used for residential construction designed and constructed under the requirements of the general building code. Provides structural design guidelines and equations to determine the moment and axial resistance of ACCW structures.

2.4.3 Incorporation of vertical reinforcement

Concrete, one of the many building materials used in traditional construction for ages, is renowned for its exceptional compressive strength, yet it is significantly weaker in tension. Therefore, concrete is often reinforced with materials that exhibit prominent tensile properties. As a composite material, reinforced concrete has been used effectively in construction. However, with the adoption of 3DPC, reinforcing 3D-printed concrete has become a challenge.

To simulate longitudinal reinforcing techniques in vertical elements, as in cast-in-place concrete structures, Marchment and Sanjayan (2020) introduced the ”Bar Penetration Reinforcing Technique”. The proposed methodology involves automatically inserting reinforcing bars into printed concrete layers at equal intervals using an automated system attached to the printer head. To evaluate particle distribution during rebar penetration, another study was conducted using equal layers printed on a sand bed, with rebar penetrated to varying lengths. Figure 2.7a shows the proposed methodology, and Figure 2.7b shows the schematic for studying the effect of penetration depth

using a sand bed.

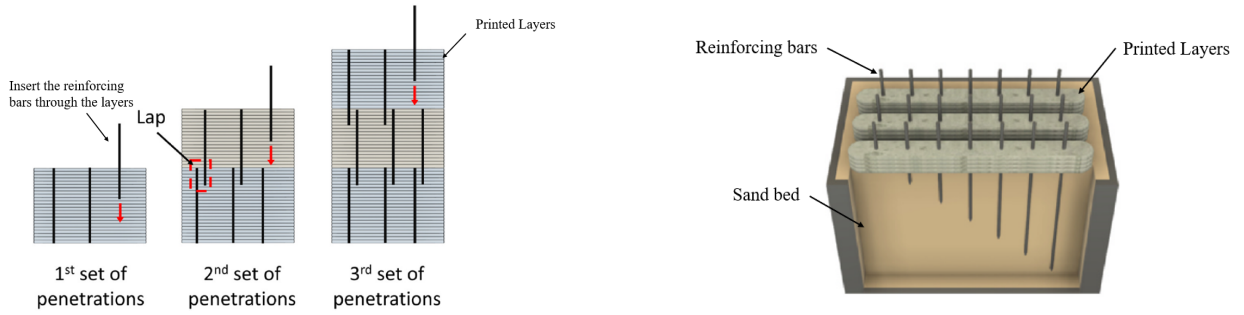


Figure 2.7: (a) Schematic of the proposed methodology to penetrate reinforcing bars into printed layers at equal intervals; (b) Schematic of penetrating different lengths through equal layer thickness on a sandbed, adapted from (Marchment and Sanjayan, 2020)

In another attempt to incorporate deformed reinforcing bars in 3DPC structures, Baz et al. (2020) studied the effect of having reinforcing bars by printing three layers and pressing reinforcing bars manually on the printed layer to half the diameter of the bar and printing subsequent layers on top of them, as shown in Figure 2.8a. To determine the bond strength between the printed concrete and rebar, pullout tests were conducted, and the results showed reductions of 13% and 22% relative to the cast-in-place sample, with an average pullout strength of 18.7 MPa. The tested samples revealed macroscopic voids created by printing on top of the reinforcing bars, with no-slump concrete used, especially in 3DPC, as shown in Figure 2.8b.

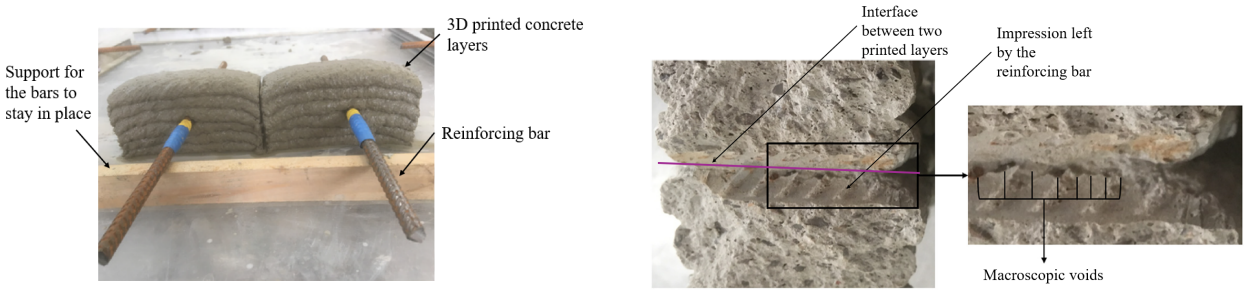


Figure 2.8: (a) Final printed specimen with reinforcing bars placed perpendicular to the printed layers and (b) Broken sample with exposed macroscopic voids around the reinforcing bars, adapted from (Baz et al., 2020)

2.5 3D Printed Reinforced Concrete Columns

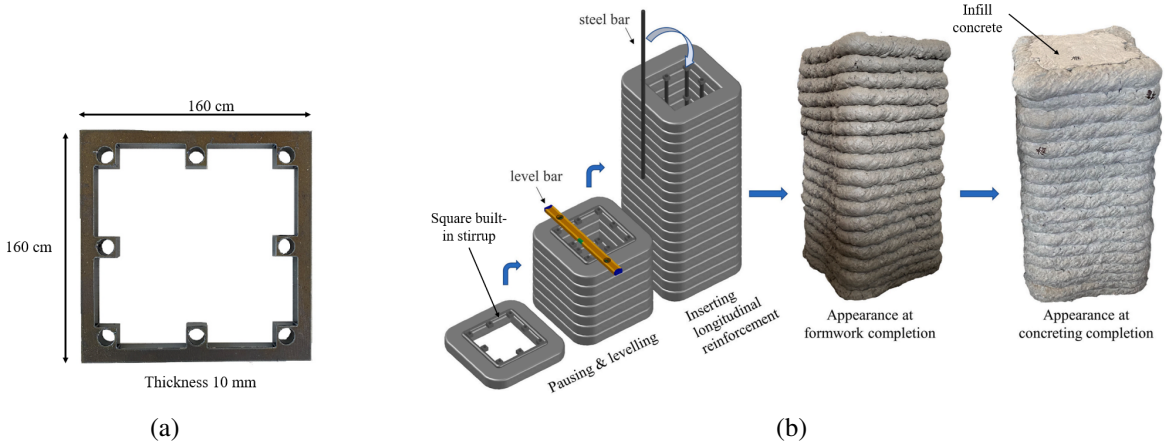
Following numerous studies on the mechanical properties and durability of 3DPC, researchers have focused on its use in fabricating structural elements. One technique for constructing reinforced columns is using 3DPC as permanent formwork (Chen et al., 2023).

To the author's knowledge, Zhu et al. (2021) was the first to explore the use of 3DPC as permanent formwork for structural columns. The study aimed to determine an optimal concrete mixture to print permanent formwork without failure during printing. Using the optimum concrete mixture identified in the study, permanent formwork was printed, and reinforcement cages with different reinforcement ratios were inserted and infilled with conventional concrete. During the experimental testing, no peeling failure of the printed concrete from the infilled concrete was observed, and the stresses were uniform across the section. The study found a positive correlation between reinforcement ratio and initial stiffness, and that all column failure modes, regardless of reinforcement ratio or column type, were due to buckling of the reinforcing bars. One major observation from the test results was that the axial compressive resistance of printed columns was 13% to 17% higher than that of cast-in-place columns, attributed to increased confinement from the printed layer.

Following the previous study Silfwerbrand (2024a), this study explored the concept of using 3DPC as permanent formwork for infilled reinforced concrete columns. One major motivation for this research is to use high-performance concrete as formwork while using moderate-strength concrete as the infill material, thereby reducing CO_2 emissions. To aid compaction during the fabrication of tall structures such as columns, Self-Consolidating Concrete (SCC) was utilised. Circular columns with a height of 3 m and a diameter of 0.3 m were fabricated and cast in place; columns of similar dimensions were fabricated using the same SCC concrete mixture. The author concluded that the compressive test results for the printed reinforced columns were similar to those of the cast-in-place counterparts.

In an attempt to investigate possible reinforcement techniques, Chen et al. (2023) introduced the

Build-in Stirrup Permanent Concrete Reinforcement Formwork (BSPCF), in addition to using reinforcing cages inserted into the printed formwork and then filled with conventional concrete. This stirrup is designed to provide the lateral confinement effect that is typically provided by the ties, and also the hoops built into the square stirrups allow the vertical reinforcing bars to be inserted after the fabrication of the printed formwork, and it also helps secure the vertical reinforcing bars to stay in place without the need for manual tying of the ties and the reinforcing bars. Axial compression tests compared BSPCF with conventional cast-in-place concrete columns, and the experiments showed similar performance. The printing process of incorporating the square stirrups (Figure 2.9a) is illustrated in Figure 2.9b.



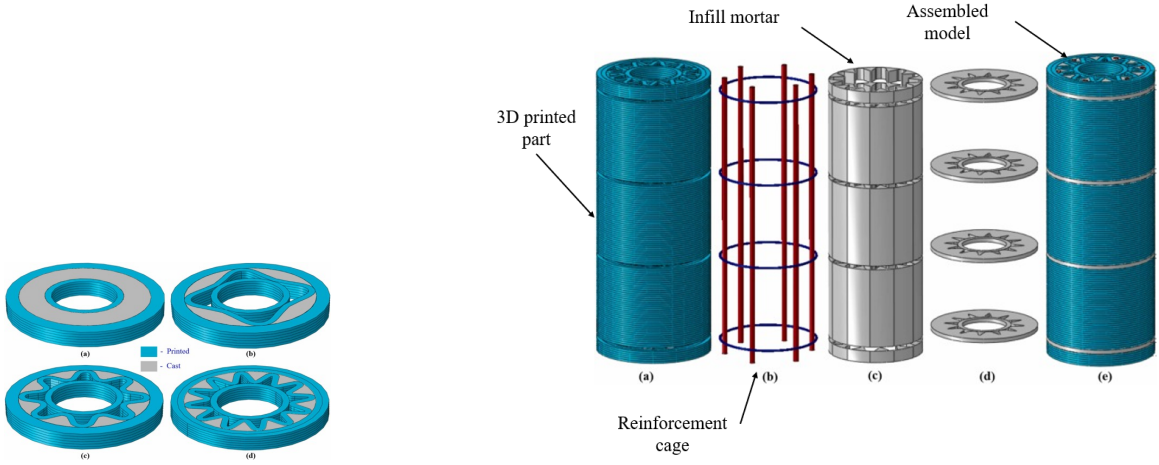
(a) (b)

Figure 2.9: (a) Photograph of the square stirrup (b) Schematic of the printing process incorporating the stirrup in the middle of printing, adapted from (Chen et al., 2023)

A similar attempt was undertaken by Bates and Aslani (2025) for reinforced concrete columns utilising 3D-printed outer shells as permanent formwork. Glass fibre-reinforced polymer reinforcing bars were used as vertical reinforcement as an alternative to conventional steel reinforcing bars. The specimens were fabricated using a small-scale desktop printer, which has an inherent height limitation for printing. Therefore, a similar approach used in the study of Raza et al. (2024), segmental construction, was implemented. Segments of height 260 mm were fabricated with overall plan dimensions of 250 mm x 250 mm with a printed layer thickness of 40 mm. The reinforcing cages were post-installed and infilled with the same concrete mixture after 28 days of curing of the printed concrete formwork. This study fabricated short and slender columns along with a con-

ventional mould-cast column as a baseline comparison. The mould-cast specimens achieved axial capacities closer to theoretical predictions. The short and long mould-cast columns failed at 242 kN and 2137 kN, respectively, while the printed columns failed at 1412 kN and 1014 kN, which is roughly 50% of the mould-cast specimens. Moreover, during testing, the printed columns failed less violently than the mould-cast specimens, and it was concluded that these printed columns could be useful in places where energy absorption or controlled failure is required.

In a recent study, Nguyen-Van et al. (2026) attempted to obtain optimised, structurally adequate lightweight reinforced concrete columns by proposing different print patterns, as shown in Figure 2.10a, which are infilled with concrete and traditional reinforcements. To obtain lateral resistance, 6-mm-diameter stirrups were used and tied to the reinforcing bars at uniform intervals, with the reinforcing bars connected by concrete layers, as shown in Figure 2.10b. The experimental results from axial compression tests on the proposed column were used to calibrate the numerical model in ABAQUS with the Simplified Cementitious Damage Plasticity (SCDP) model. One key modelling assumption is that, despite the expected anisotropic behaviour, the mortar was modelled as isotropic, justified by the reasoning that, under pure axial compression loading, the effect of anisotropy is limited.



(a) (b)

Figure 2.10: (a) Different parametric print designs to obtain lightweight reinforced concrete 3DPC columns; (b) Different sections of the proposed reinforced concrete columns, adapted from Nguyen-Van et al. (2026)

The numerical results of the proposed lightweight reinforced concrete column were compared with the experimental test results obtained in the research. Despite the assumptions, the model used in the study yielded a peak load resistance 8.75% lower than that of the experimental study, which exhibits self-centring modelling, especially in the 3DPC (Nguyen-Van et al., 2026). The percentage difference of the simulation results with the experimental results of the columns is extracted from the load-deformation graph provided in the article by Nguyen-Van et al. (2026) and are provided in Table 2.6.

Table 2.6: The axial load obtained from the experimental testing of the columns and the simulation results along with the percentage difference, adapted from Nguyen-Van et al. (2026)

Points	**Experimental Load (kN)**	**Simulation Results (kN)**	**Percentage Difference (%)**
At peak load	∼1500	∼1670	∼11.3%
At 15% reduction from the peak load	∼1280	∼1440	∼12.5%
At 50% reduction from the peak load	∼780	∼890	∼14.1%

Segmental construction using precast elements is common in bridge construction. The interface between segments in a pier acts as a pre-crack section and opens under tensile forces. Prestress forces are applied to reduce permanent opening; thus, it exhibits self-centring. However, applying the prestress has been challenging and requires heavy machinery on site. To overcome this, Fe-based Shape Memory Alloys (SMAs) have been used. The sequence of segmental construction of a bridge pier, as tested in the research reported by Raza et al. (2024), is shown in Figure 2.11.

The study was focused on evaluating the seismic performance of the bridge pier. Since the 3DPC technique was used to fabricate the column formwork and the concrete is infilled with coarse aggregate, this proposed methodology has a lower cementitious content than other 3DPC structures.

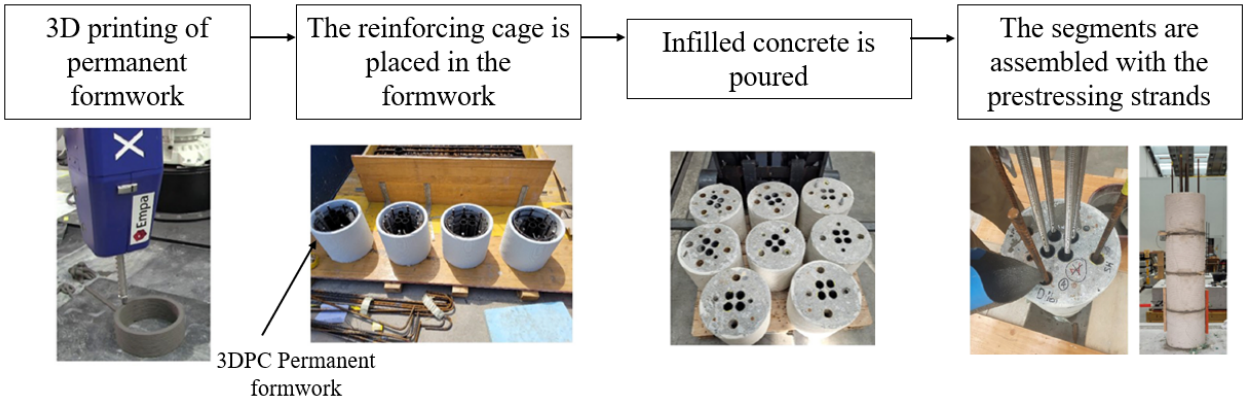


Figure 2.11: Sequence of segmental construction of a pier, adapted from (Raza et al., 2024)

2.6 Fibre Section Analysis

2.6.1 Overview of Fibre Section Analysis

Fibre section analysis is a non-linear numerical method used to predict the capacity of structural elements, such as the axial resistance of a column cross-section, the flexural capacity of a beam, or the deformation capacity of any element. A generalised approach to fibre analysis is to discretise a section into longitudinal fibre elements, and to define the positions of individual fibres using the x, y coordinates of the section (Taucer et al., 1991). A discretised section into individual fibre elements is shown in Figure 2.12.

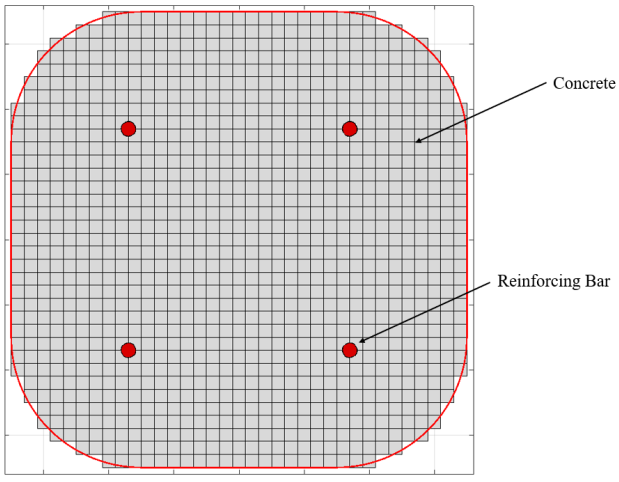


Figure 2.12: Discrete fibre section mesh for the fibre section analysis

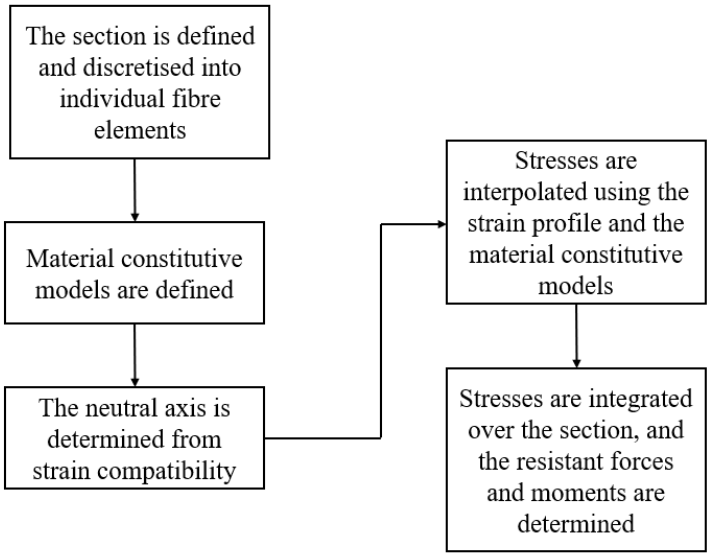


Figure 2.13: General procedure for the fibre section modelling

Several assumptions are made during this analysis. The fundamental assumptions are listed below.

- Plane sections remain plane during the element deformation history,
- There is no slip between the vertical reinforcing bar and the surrounding concrete,
- Fibre elements follow the corresponding material constitutive models (Venkateshwaran et al., 2022).

The general procedure for conducting the fibre section analysis is provided in the flowchart in Figure 2.13

Fibre section modelling is useful not only for determining axial force and moment resistance, but also for extracting the individual contributions of the constitutive materials in the section to better understand the composite behaviour of structures.

Sousa Jr and Muniz (2007) documented a proposed cross-section analysis method and outlined the overall procedure for evaluating cross-sectional properties, including section resistance and tangent modulus, in steel–concrete composite sections. The study also demonstrated the practical applica-

tion of the proposed methodology. Similarly, Lin and Liao (2004) compared experimental results for concrete confined by composite materials and extensively applied section analysis to evaluate the confinement effects provided to the infilled concrete. Marini et al. (2006), on the other hand, incorporated the effects of shear into section analysis to predict the axial and flexural behaviour of plane frame structures, with the predictions validated against experimental data from bridge piers. In addition, Shanmugam and Lakshmi (2001) compiled a wide range of research on composite columns, considering factors such as local buckling, bond strength, seismic loading, concrete confinement, and secondary stresses. Collectively, these studies demonstrate the extensive and versatile applications of section analysis, ranging from evaluating fundamental cross-sectional properties and material confinement effects to predicting the complex behaviour of composite structural systems under various loading conditions.

2.6.2 Material Constitutive Models

2.6.2.1 Concrete Stress-Strain Relation

Research studies have used crude concrete models to predict the response of reinforced concrete elements, and these studies have shown that such models are sufficient to predict experimental results, especially under monotonic loading (Taucer et al., 1991).

One of the simplest models for concrete compressive stress-strain behaviour was presented by Hognestad (1951), and the formulation is given in Equation (2.1).

$$\sigma_c = f'_c \left[2\left(\frac{\varepsilon_c}{\varepsilon_0}\right) - \left(\frac{\varepsilon_c}{\varepsilon_0}\right)^2 \right], \qquad 0 \leq \varepsilon_c \leq \varepsilon_0 \tag{2.1}$$

Where,

σ_c = compressive stress in concrete,

ε_c = concrete compressive strain,

f'_c = peak compressive strength of concrete,

ε_0 = strain corresponding to the peak compressive strength.

The transverse reinforcements that are provided in columns or beams provide lateral resistance against the lateral expansion that happens as a result of concrete dilation. The amount of confinement due to these transverse reinforcements depends on the lateral expansion. Therefore, the confinement provided is referred to as passive confinement (Hao, 2020). At low levels of strain in the concrete, the strain induced in the transverse reinforcements would be negligible, as would the confinement provided by the transverse reinforcements to the concrete core. As the concrete approaches its compressive strength and cracks develop, it induces significant strain in the transverse reinforcement, where the effect of passive confinement is pronounced (Braga et al., 2006).

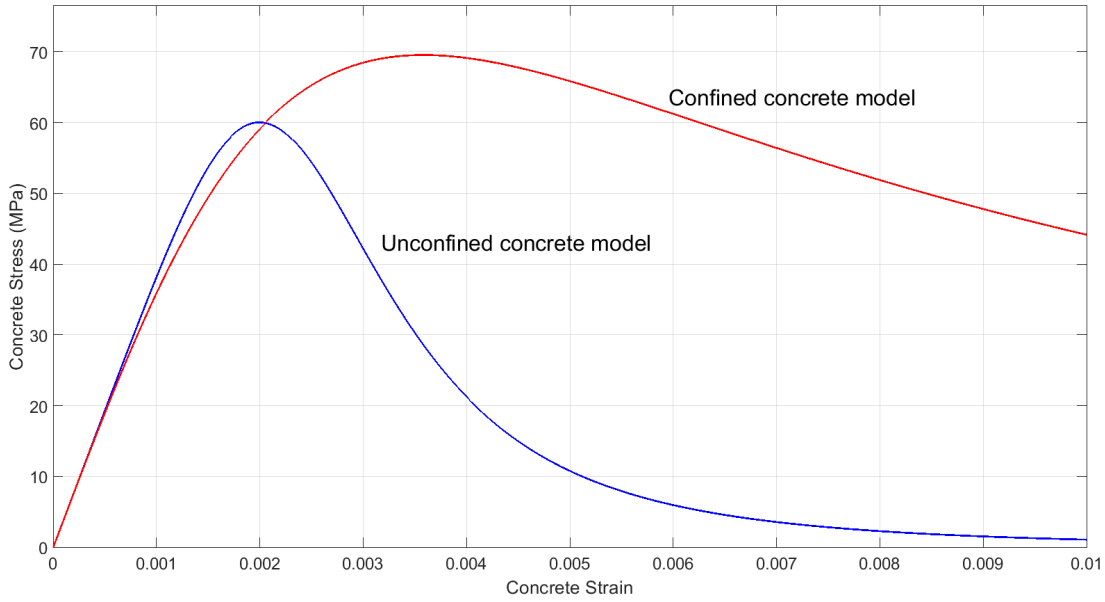


Figure 2.14: Stress-strain model for confined and unconfined concrete, adapted from Mander et al. (1988)

2.6.2.2 Steel Stress Strain Relation

Different non-linear stress-strain relationships are available for steel, including the post-peak response. However, the non-linear behaviour of the reinforcing steel used in this study was assumed to be elastic-perfectly plastic, as shown in Figure 2.15, a model used in a research study that accurately predicted the column's behaviour (Venkateshwaran et al., 2022). The model used in this

research study employs characteristic values obtained from a tension test on the steel reinforcing bars used to fabricate the rebar cages, in accordance with ASTM A370.

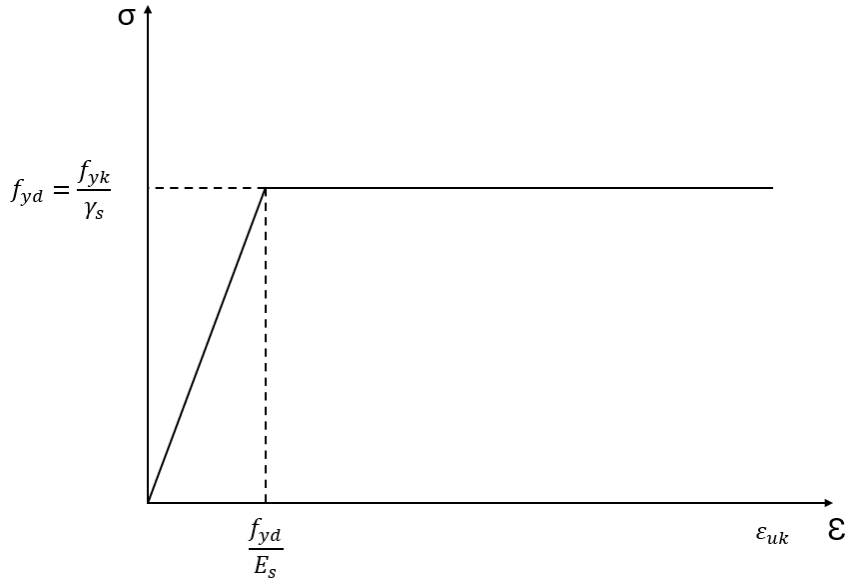


Figure 2.15: The elastic, perfectly plastic steel stress-strain constitutive model for steel

2.7 Digital Image Correlation

Digital Image Correlation (DIC) is a non-contact technique in which unique points are tracked across consecutive frames of a deforming object's surface. The initial frame serves as the baseline reference frame, where deformations are assumed to be zero, and the images captured after the object deforms are the deformed images. A fundamental working principle of DIC is that the pixels surrounding the point of interest remain unchanged during deformation. The regions tracked by DIC are called subsets (Hassan, 2021).

The subset is selected in the reference image, and to track the same subset across consecutive images, the grayscale intensity patterns of the subset in the reference image are compared with those in the deformed image. This helps the algorithm to track the subset during the deformation. This process is carried out using a correlation criterion. Multiple methods can quantify correlation. The output of the correlation coefficients ranges from -1 to 1; a value of 1 indicates a perfect match subset, and -1 indicates the poorest match subset.

However, this study did not use a traditional DIC system; instead, it employed feature tracking with the Kanade–Lucas–Tomasi (KLT) algorithm using the MATLAB Computer Vision Toolbox. The fundamental operating principles are similar to those of a traditional DIC; however, rather than tracking an entire subset of regions on the object's surface, MATLAB selects and tracks unique feature points. This algorithm is best suited for objects that do not change shape and have visual textures, which is most relevant to this research study (The MathWorks, Inc., 2024).

The KLT algorithm has two characteristics. One is tracking points within frames, and the second is how well the frame or a patch of a frame should be aligned to achieve optimal tracking. The Lucas-Kanade algorithm is used for point tracking and is also used in motion stabilisation in many applications. This algorithm works under a few assumptions, which are

- The intensity of the points does not change significantly during each frame of the motion (brightness consistency),
- The points undergo small displacements,
- The motion field within a small neighbourhood is constant.

The assumption of brightness consistency forms the fundamental equation solved in the algorithm, given in Equation (2.2).

$$I(x,y,t) = I(x+u, y+v, t+1) \tag{2.2}$$

Where,

I - intensity of the point

t, t+1 - current frame and the subsequent frame

u, v - the horizontal and vertical components of the image velocity (optical flow) x, y - position of the point at t = t

Using the second assumption, which states that the displacement between consecutive frames is

small, the brightness constancy equation can be approximated by a first-order Taylor series expansion about the current image location. By neglecting the higher-order terms, the optical flow constraint equation is obtained as

$$I_x u + I_y v + I_t = 0, \tag{2.3}$$

Where

I_x and I_y - the spatial image intensity gradients in the x- and y-directions, respectively,

I_t - the temporal image intensity gradient.

Since Equation (2.3) contains two unknowns but provides only one equation for each pixel, a unique solution cannot be obtained. To overcome this limitation, we invoke the third assumption: all pixels within a small neighbourhood undergo the same displacement. This allows us to formulate a system of linear equations using multiple neighbouring pixels, resulting in an overdetermined system that can be solved using the least-squares method to estimate the displacement vector (Suhr, 2009; Tomasi and Kanade, 1991).

2.8 Distributed Fibre Optic Sensors

Traditionally, strain gauges are used to obtain real-time strain data from structures and during testing; however, they lack the ability to provide continuous strain measurements over a specific distance and sufficient information on the development of cracks in concrete and steel elements. Distributed Fibre Optic Sensors (DFOS) have gained popularity for distributed strain measurements along a length. Key advantages of DFOS include long-distance measurements, lightweight operation, high accuracy and resolution, and, importantly, the ability to detect cracks (Xie et al., 2026).

The general construction of a DFOS array consists mainly of three components: the main sensing fibre surrounded by a cladding layer, and finally a protective layer on top of the cladding. To

ensure proper strain transfer between the substrate and the DFOS, the adhesive should be durable and sufficiently strong and stiff to prevent slippage and sliding (Abdullah et al., 2025). A typical cross-section of a DFOS cable is shown in Figure 2.16. DFOS cables are often sensitive to both strain and temperature variations, unlike optical cables with loose jackets, which are often used to measure temperature (Taborda-Llano et al., 2025).

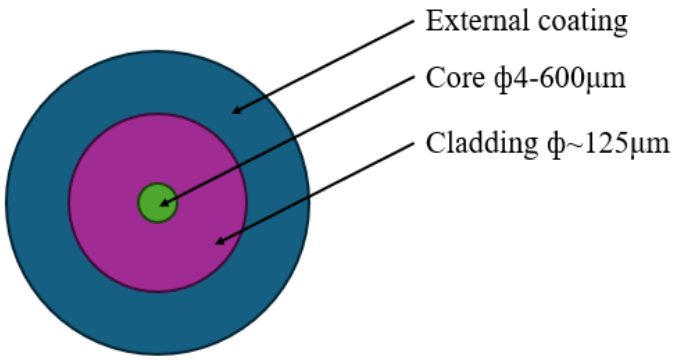


Figure 2.16: Constitutive materials of a typical distributed fibre optic cable, adapted from (Bai et al., 2022)

Typically, the core diameter ranges from 4 to 600 μm and is made of glass, which has a higher refractive index than the cladding, which is usually 125 μm m in diameter. The reduced refractive index of the cladding prevents the light from leaving the core. Finally, an external coating is applied to enhance durability and protect the fibre cable from damage. The most common material used for the outer coating is polyamide, which forms a chemical bond between the fibres, preventing slippage and improving strain transfer (Zhou et al., 2023).

The fundamental working principle of DFOS is that light of a particular wavelength is allowed to pass through, while some is reflected due to imperfections in the fibre cable. The reflected light is referred to as backscattering. Backscattered light is divided into three main categories based on wavelength: Rayleigh, Raman, and Brillouin peaks. Raman scattering is only sensitive to temperature variations and is therefore mainly used in Distributed Temperature Sensing (DTS), whereas Rayleigh and Brillouin scattering are sensitive to both temperature and strain variations. Raman and Brillouin scattering are nonlinear, inelastic processes that require higher energy and relatively

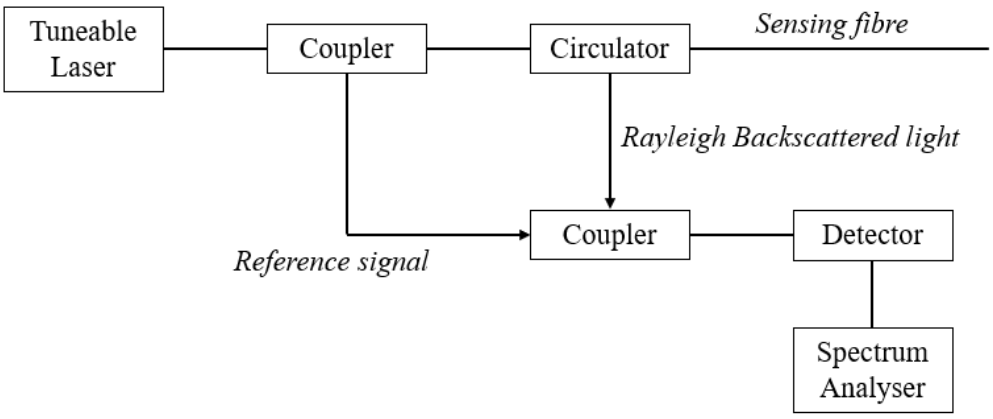


Figure 2.17: Schematic of the OFDR sensing principle of how the light travels through different components, adapted from (Tang et al., 2021)

longer measurement times. As a result, the signal-to-noise ratio (SNR) is lower for both Raman and Brillouin scattering. Rayleigh backscattering has higher SNR, which helps distinguish the actual measurement from background noise arising from laser phase noise, weak backscattering at longer distances, and environmental fluctuations. This makes Rayleigh backscattering favourable for structural monitoring and sensing applications (Palmieri et al., 2022). Sensors capable of measuring strain and temperature variations operate using two approaches. The first approach is Optical Time Domain Reflectometry (OTDR), and the second method is Optical Frequency Domain Reflectometry (OFDR) (Cooperman and Martinez, 2015). In the Rayleigh OFDR method, the backscattered light is mixed with the reference light; the schematic of the working principle is shown in Figure 2.17. Each fibre segment produces a unique fingerprint in Rayleigh backscattering, and each contains information distributed along the fibre length.

The shift in wavelength caused by variations in temperature or strain is measured, and, using the following equation (Equation (2.4)), the corresponding variations in temperature and strain can be determined (Tang et al., 2021). The OFDR technique has gained popularity in the research field for its high strain-sensing accuracy, short spatial resolution, and simultaneous high data acquisition rate. However, OFDR is commonly used for short-range sensing (10 to 35 m), while OTDR is used for 1 to 10 km (Floris et al., 2021).

$$\frac{\Delta\lambda}{\lambda} = C_T \Delta T + C_\varepsilon \Delta\varepsilon \tag{2.4}$$

Where,

$\Delta\lambda$ - backscattered spectral shift

λ - signal wavelength

C_T, C_ε - temperature and strain coefficients

ΔT - temperature variation

$\Delta\varepsilon$ - strain variation

Since the Rayleigh OFDR method is sensitive to both strain and temperature variations, two DFOS arrays are typically used to decouple their effects. One array is bonded to the substrate and captures the combined effects of temperature and strain, while the other is unbonded and measures only the strain variations due to temperature changes. When testing is conducted in a temperature-controlled environment, only a single DFOS array is required, as the effect of temperature fluctuations is assumed to be negligible (Abdullah et al., 2025).

DFOS has been used in many structural engineering studies, including crack detection and measuring strain and temperature in structures (Zhou et al., 2023). To properly transfer strain from the substrate to the fibre core, many methodologies have been proposed, including using epoxy and cyanoacrylate to attach the DFOS (Abdullah et al., 2025). Research studies that have utilised DFOS specifically in reinforced concrete applications have concluded that using epoxy to attach DFOS with a polyamide coating provides greater reliability in the bond between the DFOS and steel reinforcing bars (Zhou et al., 2023).

In a study conducted by Zhang et al. (2021a), the accuracy of DFOS was tested against measured strain values from strain gauges, and DFOS cables with different jacketing materials were also evaluated. The DFOS cables not only gave as accurate results as the strain gauge values, but it was also found that high sensitivity and low survivability do not correlate. It was also concluded that

using high-sensitivity cables would require additional care during installation.

2.9 Summary of research gaps

Although numerous studies have been conducted on 3DPC materials and structures, the reported findings are often inconsistent and, in some cases, contradictory. Differences in printing systems, materials, and process parameters have led to these varying observations regarding the mechanical behaviour of 3DPC. For example, some studies have reported pronounced anisotropic behaviour, whereas others have shown that specimens produced with certain printing systems exhibit nearly isotropic compressive strength.

Despite these differences, there is general agreement that cast specimens do not represent the intrinsic behaviour of 3DPC materials. Cast specimens tend to overestimate mechanical properties, particularly compressive strength, because they lack printed interlayers and thus do not capture the influence of layer interfaces on the overall structural response. However, some studies have reported the opposite, with extracted specimens from 3D-printed structures exhibiting higher compressive strength than mould-cast specimens. As a result, properties measured using mould-cast specimens may not accurately reflect the behaviour of actual printed structures.

Furthermore, there is currently no consensus on a standard specimen geometry for evaluating the mechanical properties of 3DPC materials. The influence of specimen geometry on the measured properties remains insufficiently understood, making comparisons between studies challenging. In addition, the effect of specimen size on the mechanical behaviour of 3DPC has received limited attention and remains an area requiring further investigation.

The use of 3DPC as a permanent formwork system for reinforced concrete structural elements, including beams, columns, and walls, has gained increasing attention in recent years. Experimental studies have demonstrated the feasibility of this approach and highlighted its potential for reducing formwork requirements and construction time. To date, much of the research has focused on

concrete-filled 3DPC walls and on developing connection mechanisms between structural elements, such as beam-column and column-wall connections. While these studies have established the viability of 3DPC as a permanent formwork solution, a comprehensive investigation of the structural behaviour of individual elements, particularly columns, remains underexplored. Such understanding is necessary before the behaviour and performance of more complex structural systems and connections can be reliably assessed.

To the author's best knowledge, only a limited number of studies have investigated the use of 3dPC as permanent formwork for reinforced concrete columns. While these studies have demonstrated the feasibility of the concept, the available knowledge remains insufficient to establish design guidelines or recommendations for the structural sizing of such columns. Consequently, practitioners tend to adopt conservative design approaches, neglecting the structural contribution of the 3DPC formwork and relying solely on the infilled concrete and longitudinal reinforcement to resist applied loads. Therefore, a comprehensive understanding of the individual and combined load-carrying contributions of the constituent materials is essential for the efficient and reliable design of 3DPC permanent formwork reinforced concrete columns.

Based on the literature reviewed, significant research efforts have focused on process parameters, material rheology, and material behaviour, and on exploring their application as permanent formwork for reinforced concrete members. However, important knowledge gaps remain regarding the representative specimen to evaluate the intrinsic behaviour and mechanical properties of printed structures, the structural behaviour of 3DPC permanent formwork reinforced concrete columns, particularly with respect to load-sharing mechanisms, the contribution of the printed shell to axial load resistance, and the implications for structural design. Addressing these gaps is necessary to support the development of rational design methodologies and facilitate the broader adoption of this construction technique in structural engineering practice.

Chapter 3 Mechanical Properties of 3DPC and Printed Cylindrical Shells[1]

3.1 Introduction

Concrete is one of the most widely used construction materials worldwide due to its high compressive strength and geometric adaptability. Despite emitting less carbon per unit volume than many alternative building materials, the extensive use of concrete in construction contributes significantly to global carbon emissions. Historically, reinforced concrete structures have predominantly adopted conventional geometries that optimise the use of standardised, reusable formwork, which remains a significant cost driver in construction projects. Although reinforced concrete elements can be structurally optimised, the high cost of custom formwork has traditionally limited the adoption of more complex, materially efficient structural forms until the incorporation of additive manufacturing using concrete (Bos et al., 2016).

3D-concrete printing (3DCP) is an extrusion-based additive manufacturing process that has developed rapidly in recent years. Numerous studies have investigated printed concrete as permanent formwork to replace traditional formwork in cast-in-place reinforced concrete construction (Raza et al., 2024; Chen et al., 2023). In contrast, another set of studies considered 3D-printed concrete as the primary load-bearing element (Ji et al., 2019; Silveira et al., 2024) and focused on developing reinforcement strategies (Li et al., 2020; Pham et al., 2020). Experiments by Panda et al. (2017) and Wang et al. (2023) concluded the presence of inherent anisotropy in the printed concrete, and Panda et al. (2017), Quah et al. (2023), and Wolfs et al. (2018) studied the influence of process parameters on the hardened properties of printed concrete. Furthermore, recent research has investigated alternative concrete materials, such as low-carbon concrete (LCC) (Natanzi and McNally, 2023), as well as alternatives to fine aggregates (Mim et al., 2025). Although numerous studies

[1] Part of this chapter has been used in the Author's publication with the supervisor, titled "Experimental Characterisation of the Modulus of Elasticity of 3D-Printed Concrete (3DPC) Utilising Full-Scale Printing Parameters (Subakaran and Butler, 2026)"

have examined various aspects of 3DCP, little effort has focused on developing a structural design framework for 3D-printed concrete (3DPC) elements. In particular, the composite structural behaviour of 3DPC when used as permanent formwork remains poorly understood. The fundamental parameters for establishing a design framework are the mechanical properties of printed concrete, which require standardised, robust testing procedures.

This research study focuses on better understanding and measuring the modulus of elasticity (MoE) of 3DPC printed on commercial-scale printers, primarily using saw-cut specimens rather than cast specimens. MoE is one of the most important mechanical properties for any structural design framework. ASTM C469 (American Society for Testing and Materials, 2022) recommends the testing procedure to determine the static MoE of concrete using concrete cylinders; however, differences in mechanical properties between cast specimens and printed specimens have been reported in the literature (Panda et al., 2017). Therefore, this chapter aims to develop a robust, reliable method for estimating the modulus of elasticity of 3DPC using two specimen sizes with width-to-height ratios of 1 and 2. A total of 25 and 8 cube specimens were tested in the directions perpendicular and parallel to the interlayer plane, respectively, and 3 prisms were tested in the direction perpendicular to the interlayer plane. The MoE values obtained with these methods were then used to calculate the axial stiffness of the 3DPC shell, which was subsequently compared with the axial stiffness derived from the load-deformation response during the uniaxial compression test.

3.2 Experimental Plan

3.2.1 Material and Concrete Printer

The concrete mixture design used in this research was a proprietary mixture developed by an industry partner. Prior experience and experiments using the same mixture design confirmed the concrete's extrudability and multilayer buildability. General-use limestone (GUL) cement was used as the binder. Manufactured sand with a maximum size of 1 mm and limestone with a maximum aggregate size of 5 mm were used as fine and coarse aggregates, respectively. To achieve the

desired workability and performance, MasterGlenium-7925 (superplasticiser), MasterAir-AE-200 (air-entraining agent), MasterRoc-AGA-41 (stiffener), and MasterKure-ER-50 (curing agent) were appropriately added to the mix. In addition, the mixture contains monofilament micro synthetic fibre (MasterFiber M 35) with a length of 19 mm and an equivalent diameter of 23 microns. The proportions of the designed concrete are listed in Table 3.1.

Table 3.1: Mixture ratios of proprietary concrete mixture

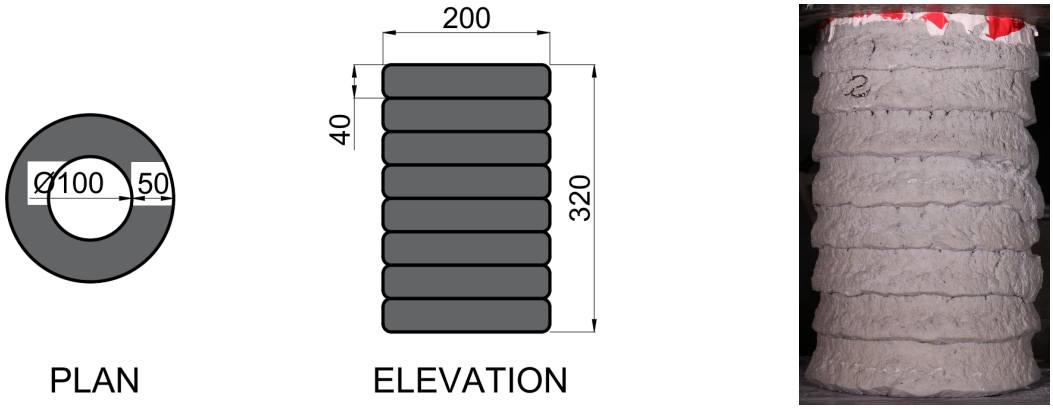
Material	**Mixture ratio**
Water/binder (l/kg)	0.27 - 0.31
Fine aggregate/binder (kg/kg)	1.6 – 1.8
5mm Coarse aggregate/binder (kg/kg)	0.6 – 0.7
Superplasticizer/binder (l/kg)	0.004 – 0.006
Air entraining admixture/binder (l/kg)	0.0007 – 0.0010
Stiffener/binder (l/kg)	0.007 – 0.011
Curing agent/binder (l/kg)	0.0015 – 0.0025
Synthetic fiber/binder (kg/kg)	0.0006 – 0.0010

A commercial, large-scale gantry-type printer, the COBOD BOD2, was used to print the 3DPC specimens and concrete was batched on-site at York University's Keele Campus in Toronto. Based on previous experience, the printing parameters were set to optimal conditions, with layer height and width set to 40 mm and 50 mm, respectively. Consistent printing was achieved by introducing a stiffening agent at the printer nozzle, thereby increasing the stiffness of the cementitious mixture just before deposition. Shear vane and slump tests were conducted prior to pumping, and the results ranged from 10 to 12 kPa and 75 mm to 130 mm, respectively. In addition, to prevent layer collapse, the print speed was adjusted so that consecutive layers were printed in 7 seconds, providing sufficient time for the green strength to develop and support the weight of adjacent layers.

3.2.2 Specimen Preparation

The cube and prism specimens required for this test were saw-cut from a single-layer-thick (50 mm) 3DPC wall specimen measuring 1000 mm x 1200 mm x 500 mm. To prevent stress localisations by

introducing layer joints along a vertical joint, the starting positions of each layer were randomised so that no consecutive layers would start at the same location. Along with the characterisation wall, three cylindrical shells with a diameter of 200 mm and an overall height of 320 mm were printed using the same concrete mixture as the walls, and three companion standard cast cylinders measuring 100 mm x 200 mm were cast in accordance with ASTM C39 (American Society for Testing and Materials, 2024). The dimensions of the 3DPC cylindrical shells and the elevation view of a 3DPC cylindrical shell are shown in Figure 3.1.



(a) (b)

Figure 3.1: (a) Cross-section and elevation of the 3DPC cylindrical shell; (b) 3DPC cylindrical shell

All the specimens were placed under a tarp for two days to prevent excessive moisture loss, then cured outdoors under natural conditions. After 28 days, the wall specimens were cut into small slab pieces for easy handling on the concrete table saw. Samples were then cut to the final required size. A total of 31 cubes (50 mm x 50 mm x 50 mm) and three prisms (50 mm x 50 mm x 100 mm) were saw-cut. It was ensured that at least one layer was captured near mid-height in all specimens.

3.2.3 Uniaxial Compressive Response and Modulus of Elasticity

The 28-day cylinder compression test was conducted in accordance with ASTM C39 (American Society for Testing and Materials, 2024), and the static modulus of elasticity of the cubes was determined based on the procedure specified in ASTM C469 (American Society for Testing and Materials, 2022). Based on the literature review of the material properties, the mechanical properties

of 3D-printed concrete (3DPC) are not adequately represented by those obtained from mould-cast specimens. Therefore, this chapter focuses exclusively on determining compressive strength and modulus of elasticity using cubes and prisms saw-cut from the printed walls, and comparing the initial axial stiffness values obtained from 3DPC cylindrical shells.

The saw-cut cube specimens were checked for any imperfections on the loading surfaces and ground by hand with a hand grinder to the best of the operator's ability. Two foil strain gauges (25 mm) were attached to opposite sides of the cylinders to measure strain; because the 25 mm strain gauges do not have wires soldered, the foil strain gauge was first attached to the specimen using quick-set cyanoacrylate adhesive. Later, wires were soldered to the strain gauges, and then the connecting wires were soldered to the wires attached to the strain gauges. This process must be done carefully, as soldering the wires to the foil strain gauges can cause the strain gauge to melt. Figure 3.2 shows how to attach the foil strain gauge and connect the wires.



(a) (b) (c)

Figure 3.2: (a) Strain gauge shall be attached in the required position using the adhesive, (b) conducting wires shall be soldered to the conducting pins on the strain gauge, and (c) the connecting wires are soldered to the wire attached to the conducting pin

Trial specimens with dimensions similar to those of the cubes were tested at different displacement-controlled loading rates, and an optimal displacement rate of 0.12 mm/min was selected for subsequent tests, providing a reasonable loading rate for data acquisition. The loading procedure consisted of two loading-unloading cycles up to 12 kN (45% of the peak load obtained in the compression test on the cubes), followed by loading to failure. Because of the irregular vertical profile, each cube specimen was imprinted on paper and then traced to scale in AutoCAD to obtain the necessary dimensions.

To calculate stress, three dimensions were used: the minimum width (xmin), the maximum width (x_{max}), and the mean width (x_{mean}). The mean width of the specimen was calculated using Equation (3.1):

$$x_{\text{mean}} = \frac{\text{Area}}{\text{Height of the specimen}} \tag{3.1}$$

The areas of the section, A_{min}, A_{max}, and A_{mean}, perpendicular to the direction of loading, were calculated in three ways using x_{min}, x_{max}, and x_{mean}, respectively. The stress (σ) was calculated using Equation (3.2);

$$\sigma = \frac{\text{Applied load}}{\text{Corresponding area of the section}} \tag{3.2}$$

Three specimens were instrumented with foil strain gauges, and the average strain-gauge readings were used in the MoE calculations. Chord modulus of elasticity is then calculated using Equation (3.3), provided in ASTM C469 (American Society for Testing and Materials, 2022).

$$E_c = \frac{S_2 - S_1}{\varepsilon_2 - 0.00005} \tag{3.3}$$

Where:

E_c = chord modulus of elasticity (MPa),

S_2 = stress corresponding to 40% of the ultimate compressive strength,

S_1 = stress corresponding to a longitudinal strain of 0.000050,

ε_2 = longitudinal strain at S_2.

3.2.4 Uniaxial Compression Test – Cylindrical Shells

The top surface of the printed layers features a corrugated pattern to optimise interlayer adhesion during printing. To ensure uniform load distribution, a 5– 10 mm layer of hydrostone was applied to the top surface and cured for 24 hours before testing. The stress-strain response of the hydrostone is provided in Appendix C. Trial specimens with similar dimensions were used to determine a suitable displacement-control loading rate, and a displacement rate of 0.5 mm/min was selected for the cylindrical shell tests. A preload of 5 kN was initially applied to all specimens to accommodate seating effects during the pre-test. To measure the axial shortening of the elements, two spring-loaded linear potentiometers, manufactured by Penny and Giles with a stroke length of 50 mm, were attached to the loading plate connected to the actuator and rested on the supporting beam at the bottom, as shown in Figure 3.3. The potentiometers and actuator were connected to a data acquisition system (DAQ) for seamless data acquisition and analysis.

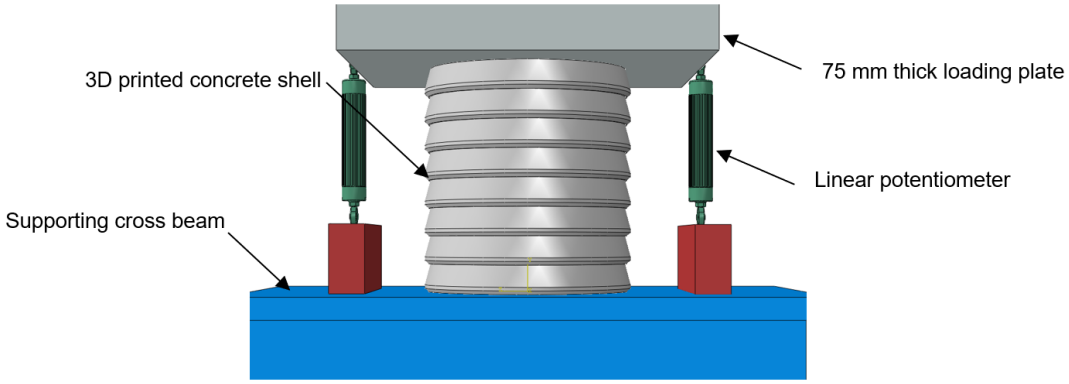


Figure 3.3: Compression loading setup of the printed concrete shells

To determine the most suitable specimen for estimating the elastic modulus of the 3DPC, the elas-

tic axial stiffness of the shell elements was calculated from the load-displacement response using Equation (3.4), and the axial stiffness estimates from both the cubes and prisms were obtained using Equation (3.5).

$$k_{\text{axial,exp}} = \text{slope of the tangent} \tag{3.4}$$

$$k_{\text{axial,theor}} = \frac{E_c A}{L} \tag{3.5}$$

Where,

E_c = Modulus of elasticity of concrete (MPa)

A = Area of the cross-section (mm^2)

L = Length of the specimen (mm)

3.3 Experimental Results

3.4 Compressive Strength Test Results

The cast cylinders yielded an average 28-day compressive strength of 42.8 MPa with a standard deviation of 4.61 MPa. The elastic modulus, evaluated using cylinders at 28 days per ASTM C469, was 21.3 GPa. The failure mode of the cast cylinders follows the ASTM type 2 failure, where a part of the cone is formed on one end of the cylinder while vertical cracks are developed on the other end (American Society for Testing and Materials, 2024). This behaviour indicates that the specimens failed under compression load. The failure patterns of the tested cylinders are provided in Figure 3.4.

The saw-cut cubes and prisms were tested 219 days after printing, along with two sets of 3 cylinders each, which were cast from the concrete mixture used during the day of printing and infilling of



(a) (b) (c)

Figure 3.4: Failure pattern of the cylinders tested under compression loading, which falls under category 2 as per ASTM standards

the columns. The compressive strength results of the tests conducted on saw-cut specimens are provided in Table 3.2. The recorded failure patterns of all cubes tested in the direction perpendicular to the interlayer planes are shown in Figure 3.5. Most cubes failed by crack propagation along a near-vertical direction near the specimen's irregular edges, followed by concrete crushing. This behaviour supports the conclusion that the irregular concrete edges inherent in 3DPC structures do not contribute to load resistance. Some failures were also caused by multiple vertical splitting cracks, which can be categorised as columnar failure.

The average stress–strain responses of the saw-cut cube specimens and the cylinders cast using the concrete mixtures from the 3DPC and infilling concrete are presented in Figure 3.6. Based on these responses, a second-order polynomial curve was fitted, and the corresponding average stress as a function of strain relationships were developed for each concrete mixture. The relationships for the cylinders cast from the 3DPC and infill concrete mixtures are provided in Equations (3.6) and (3.7), respectively, while that for the saw-cut cube specimens is provided in Equation (3.8).

Table 3.2: Compression strength test results summary

Specimen Type	Number of specimens	Direction of loading	Compressive Strength (MPa)[a]		Coefficient of Variation (%)
			Mean	SD	
50 mm cubes	25	to interlayer	44.69	6.67	15
50 mm cubes	8	to interlayer	44.13	6.61	15
Prisms	3	to interlayer	35.22	6.80	19

[a] Compressive strength was calculated using the minimum cross-sectional area perpendicular to the loading direction.



Figure 3.5: 50 mm cube specimens tested in the direction perpendicular to the interlayer plane

$$\sigma_{pc,cylinder} = -7766636.7\varepsilon^2 + 43091.5\varepsilon \tag{3.6}$$

$$\sigma_{inf,cylinder} = -7575125.3\varepsilon^2 + 42838.9\varepsilon \tag{3.7}$$

$$\sigma_{cube} = -3785755.3\varepsilon^2 + 25178.1\varepsilon \tag{3.8}$$

Where,

$\sigma_{pc,cylinder}$ is the stress in the cylinder from the printed concrete mixture (MPa),

$\sigma_{inf,cylinder}$ is the stress in the cylinder from the infill concrete mixture (MPa),

σ_{cube} is the stress in the saw-cut cube specimens (MPa),

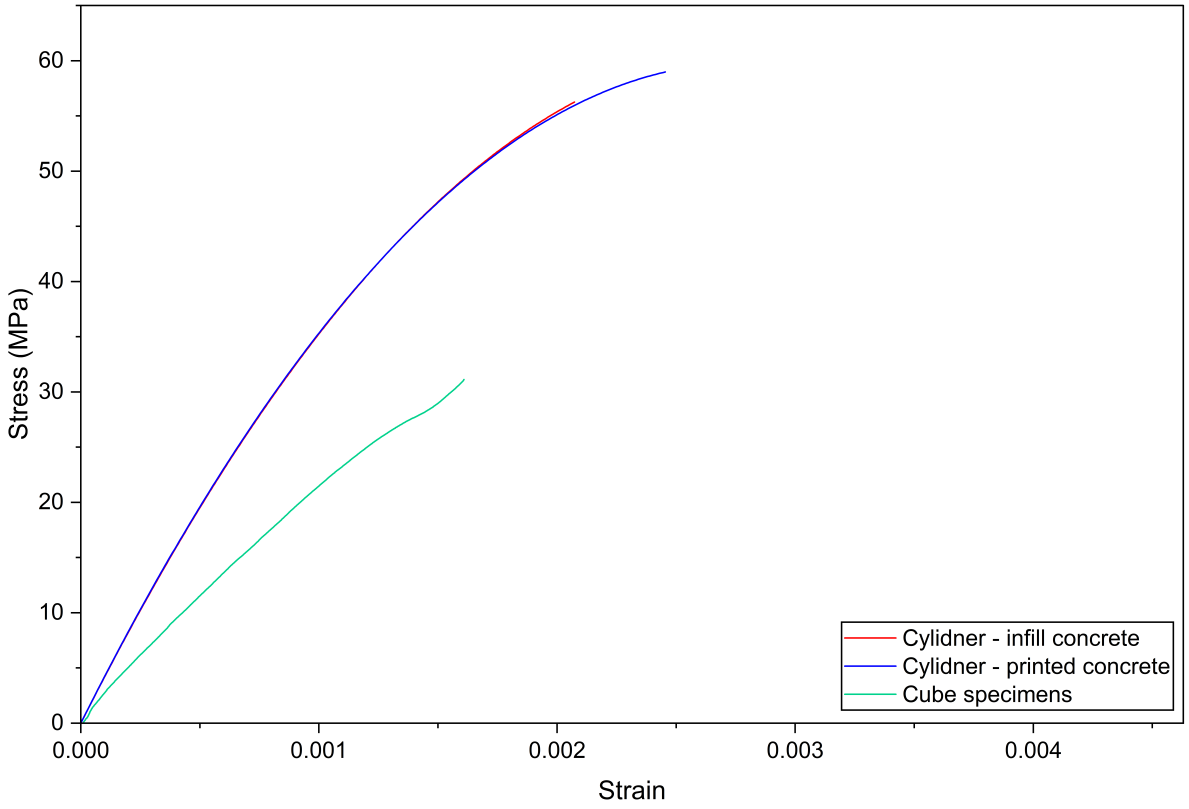


Figure 3.6: Stress-strain response of the saw-cut cubes and the cast cylinders from the 3DPC and infill concrete mixture

3.5 Modulus of Elasticity

The MoE was calculated based on Equation (**??**) for both the 50 mm cube specimens and the prism specimens. The prisms had the same base dimensions as the cubes but a height of 100 mm perpendicular to the interlayer plane. This allowed the elastic response to be evaluated for specimens with different heights while maintaining the same cross-sectional dimensions. For the stress calculations, the minimum cross-sectional area of each specimen was adopted to account for variations in the printed geometry and cross-section. The resulting MoE values and other relevant test results are summarised in Table 3.3. The mean MoE values obtained from the cube and prism specimens were 22.6 GPa and 23.4 GPa, respectively, indicating a similar average stiffness for the

two specimen geometries

Table 3.3: Modulus of elasticity results

Specimen ID	Cube (50 mm)	Prisms (50 mm x 50 mm x 100 mm)
1	21.4	28.5
2	34.9	11.7
3	11.6	29.9
Mean	22.6	23.4
SD	6.8	10.1

* The stress used in the modulus of elasticity calculation was determined based on the minimum cross-sectional area perpendicular to the loading direction.

3.6 Compression test results of cylindrical shells

Figure ref fig: deformationcurveshells presents the load–displacement curves obtained from the uniaxial compression tests. Displacements were measured independently on the right and left sides of each specimen using potentiometers to ensure uniform loading. The average of these two measurements was subsequently used to represent the overall axial displacement response of the specimen.

The measured peak loads for the three specimens were 480 kN, 515 kN, and 395 kN, resulting in an average peak load of 463 kN. The coefficient of variation (CoV) was 13.3%, indicating moderate variation in peak load capacity among the specimens. Although the first two specimens exhibited relatively similar peak loads, the third specimen reached a noticeably lower capacity, contributing to the observed variation. This difference may be associated with variations in the specimen geometry or local imperfections introduced during the printing.

All the concrete shells exhibited initial vertical cracks that formed at the bottom and propagated upwards. The failure near peak loads initiated at the intralayer joints formed during printing, and the concrete split along cracks that propagated through these joints. No concrete crushing was

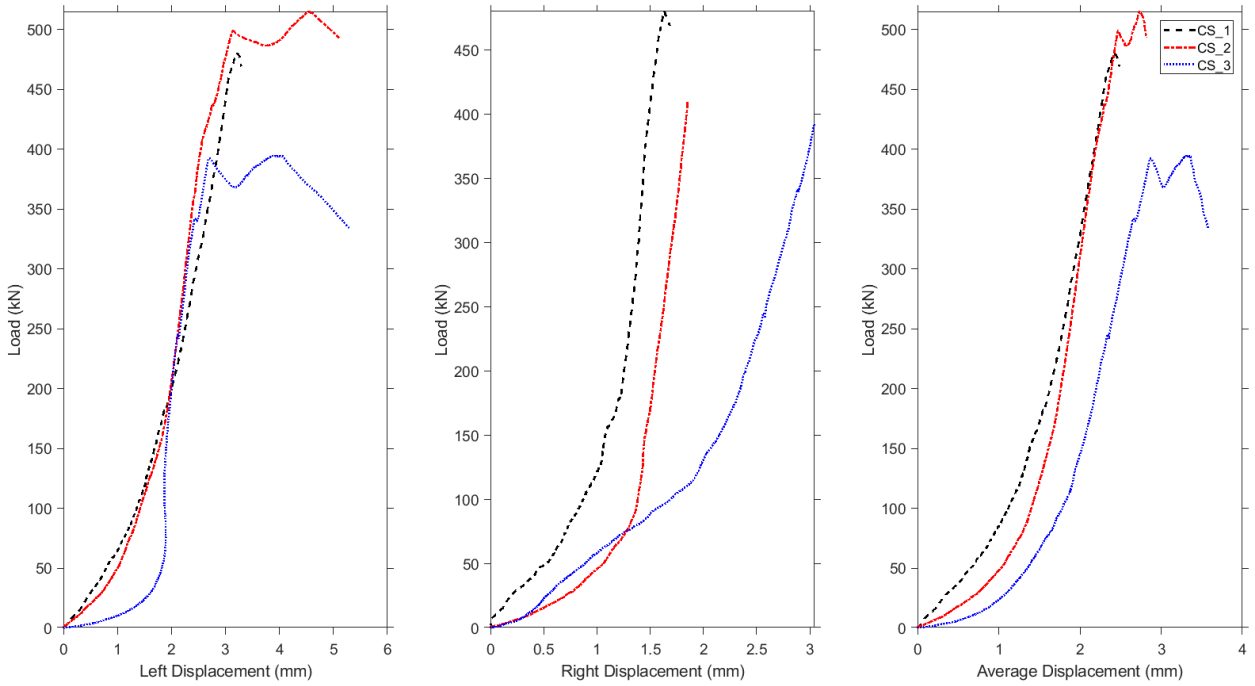
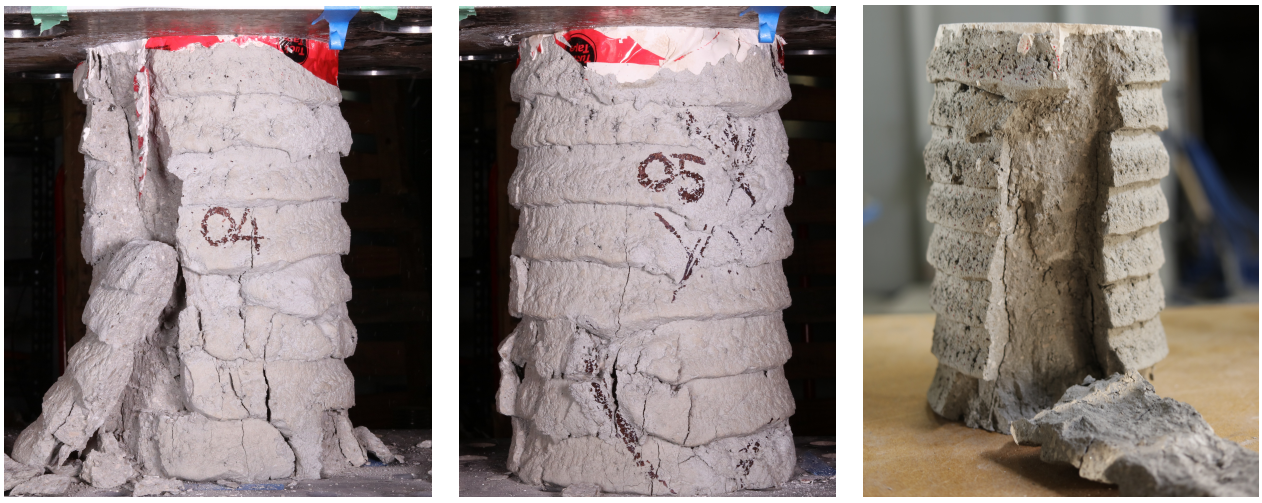


Figure 3.7: Load-displacement response using the left, right, and average displacements.

observed in any of the specimens. However, the failure pattern of all the shells could be categorised as concrete spalling due to splitting vertical cracks. The failure patterns of all specimens are shown in Figure 3.8.



(a) (b) (c)

Figure 3.8: Failure pattern of the concrete shells under axial compression.

3.7 Experimental Analysis

3.7.1 Compressive Stress Results

The compressive stress was calculated using three different cross-sectional areas. The summary statistics for the three methods of defining stresses are given in Table 3.4. Based on these values, it was decided to use the stress values obtained considering the minimum cross-sectional area.

Table 3.4: Summary statistics of compressive stress

Stress (MPa)	Mean	SD	CoV (%)
Using the minimum area	44.69	6.67	14.92
Using the mean area	37.78	6.51	17.23
Using the maximum area	35.83	7.09	19.79

3.7.2 Statistical Analysis of Compressive Strength Results of Cubes

To evaluate whether the 3DPC exhibits anisotropic behaviour as reported in previous studies, the compressive strength measured in directions perpendicular and parallel to the interlayer plane was statistically compared. The normality of the data set was initially assessed using the Shapiro-Wilk test. The p-values of the data sets were 0.83 ($\rho > 0.05$) and 0.87 ($\rho > 0.05$) in the direction perpendicular and parallel to the plane of the interlayer. This concluded that neither dataset significantly deviated from normality. An F-test was conducted to verify that the variances were equal between the two data sets. The F-statistic was 1.016, indicating no significant difference in variance between the data sets at the 95% confidence level. Therefore, a two-sample t-test assuming equal variances was conducted, yielding a p-value of 0.838.

3.7.3 Axial Stiffness – Experimental and Theoretical Estimate

The axial stiffness of the 3DPC shell specimens was evaluated using two approaches. In the first approach, axial stiffness was determined directly from the load–displacement response obtained during the uniaxial compression tests, as calculated using Equation (3.4) and reported in Table

3.5. In the second approach, axial stiffness was calculated using Equation (3.5), based on the MoE values measured from the cube and prism specimens.

The estimate of the axial stiffness obtained using Equation 5, based on the elastic modulus of the 50 mm cubes (MoE - mean: 22.6 GPa, SD: 6.8 MPa), is 656 kN/mm, and from the prisms (MoE - mean: 23.4 GPa, SD: 10.1 GPa) is 680 kN/mm.

Table 3.5: Axial stiffness determined from the load-displacement response

Specimen ID	**Axial Stiffness (kN/mm)**
CS_1	400.7
CS_2	425.1
CS_3	311.2
Mean	379.0
SD	59.9

3.8 Discussion

3.8.1 Variability in compressive strength

This chapter experimentally investigated only specimens saw-cut from a full-scale 3DPC wall element, treating them as representative of the material's intrinsic behaviour. Compressive strength tests on cubes loaded perpendicular and parallel to the interlayer plane, and on prisms loaded perpendicular to the interlayer plane, yielded CoV values of 15%, 15%, and 19%, respectively, as summarised in Table 3.4. These levels of variability fall within the range of CoV values (4%–24%) reported in the literature for similar 3DPC tests (Bos et al., 2016). The consistent failure pattern observed in all cube specimens further supports this assessment, indicating uniform global behaviour despite local variations in strength.

3.8.2 Anisotropy and loading direction in cubes

A two-sample t-test was conducted on the compressive strength results of cubes obtained from the perpendicular and parallel directions to determine the anisotropic nature of the 3PDC. The t-test yielded a p-value of 0.838 (> 0.05), indicating no statistically significant difference between the two datasets at the 95% confidence level. This indicates that the 3DPC showed no significant dependence on the loading directions tested in this chapter.

3.8.3 Behavior of prisms and cubes

Prisms exhibited, on average, a 21% lower compressive strength than cubes cut from the same wall and tested in the same loading orientation. The observed combination of crushing and tensile cracking, together with the slender geometry, suggests that bending and potential buckling reduced the prisms' measured strength at peak load.

MoE was estimated only in the direction perpendicular to the interlayer plane, using both cube and prism specimens. The MoE obtained using the cube and the prism were 22.6 GPa and 23.4 GPa, respectively. With only a 3% difference in the MoE estimated from both specimens, it is recommended that both specimens provide reasonable estimates of the elastic values.

3.8.4 Axial stiffness of 3DPC shells

The axial stiffness of the concrete shells was calculated using two different approaches. First approach: using the load-deformation response under axial compression. The load-deformation response recorded on the left and right sides of the specimen exhibited eccentric behaviour, despite careful alignment along the actuator's line of action and the application of hydrostone to level the top surface, ensuring uniform load distribution. The resulting axial stiffness, calculated from the load-average deformation response as per Equation (3.4), was 379 kN/mm.

The second approach idealised the 3DPC shell as having a uniform cross-section along its height and used Equation (3.5), with the MoE derived from the cube and prism specimens, to estimate

the axial stiffness. The shell height in this model was taken as the average of four measured points, while the cross-sectional dimensions were taken as the average of the top and bottom measurements taken at three points. Using this approach, the estimated axial stiffness based on the cube MoE (656 kN/mm) and prism MoE (680 kN/mm) was an overestimate by 73% and 79%, respectively.

3.9 Conclusion

This chapter presented the experimental results (compressive strength and MoE) of 3DPC specimens saw-cut from a full-scale wall fabricated with a commercial-scale printer. The major findings are summarised as follows:

- The compressive strength measured from the cubes and prisms had coefficients of variation of 15% and 19%, respectively, which are comparable to values reported in the literature, and all samples exhibited consistent failure modes. This indicates that the scatter in the measured properties is attributable to material behaviour rather than experimental inconsistencies.

- The two-sample t-test conducted on the compressive strength results of the cubes tested in directions perpendicular and parallel to the interlayer plane yielded no statistically significant variation at a 95% confidence level. Therefore, the uniaxial compressive behaviour was independent of the loading orientation; hence, the material exhibits isotropic compressive behaviour within the investigated range.

- The compressive strength of the prisms was 21% lower than that of the cubes tested in the same loading orientation. However, the MoE determined from both specimens was nearly identical, differing by only 3%. This suggests that the reduced prism strength likely resulted from premature buckling failure rather than a fundamental difference in material strength.

- The tested specimens showed higher standard deviation than conventional cast control specimens for both compressive strength and the MoE test. Nonetheless, the consistent, repeatable failure patterns indicate that this variability is likely attributable to the intrinsic behaviour of

3DPC rather than to deficiencies in the testing procedure.

- The axial stiffness of the 3DPC shell element calculated using the modulus of elasticity obtained from the cubes and prisms overestimated the actual stiffness by 73% and 79%, respectively.

Chapter 4 Axial Testing of Reinforced 3DPC Columns

This chapter details the experimental program, instrumentation, and test setup employed for the uniaxial compression testing of reinforced 3DPC columns. The study included both large-scale square and small-scale circular column specimens. Given the testing facilities' maximum capacity, the square columns were tested to a maximum load of 1000 kN (i.e., not to failure). The small-scale circular columns were tested to failure. The chapter also presents the experimental findings, including load-carrying capacity, axial compression response, cracking behaviour, and failure mechanisms. Comparisons are made with conventionally cast-in-place reinforced concrete columns, which were constructed and tested as control specimens to establish baseline structural performance and facilitate the evaluation of 3DPC specimens.

4.1 3D-Printed Reinforced Concrete Column Design

4.1.1 Square Reinforced 3DPC Columns

Large-scale 3D-printed reinforced concrete columns with a square cross-section measuring 350 mm x 350 mm and 1040 mm in height were fabricated for this study. The outer geometry (veneer) was initially printed using the 3DPC concrete mixture before the longitudinal reinforcing bars and transverse ties were inserted; the interior hollow space was then infilled (i.e., cast) with the same concrete mixture used in the outer veneer. This study proposed and tested two 3DPC column cross-section designs. The designs were chosen to maximise the amount of 3DPC versus infilled concrete. The first specimen type has 47% of the 3DPC volume and is referred to as the 47PC layout, which involves printing the external veneer, inserting the reinforcing bar cage, and then infilling with concrete. This column layout has been investigated in numerous studies. The second specimen type proposed in this study is optimised to incorporate more 3DPC, thereby improving the printing process and reducing manual labour in column fabrication. The optimised layout has 60% 3DPC in volume and is referred to as 60PC, improving printing by modifying the printed

section area. The section geometry and elevation details of all the columns studied in this research are shown in Figure 4.1, along with the attached DFOS to the reinforcing bar and ties. In addition to the reinforced 3DPC column, Cast Control Column (CCC) specimens were cast with the exact overall section dimensions and geometry to establish baseline structural performance parameters and to validate the fibre model extensively used in this study.

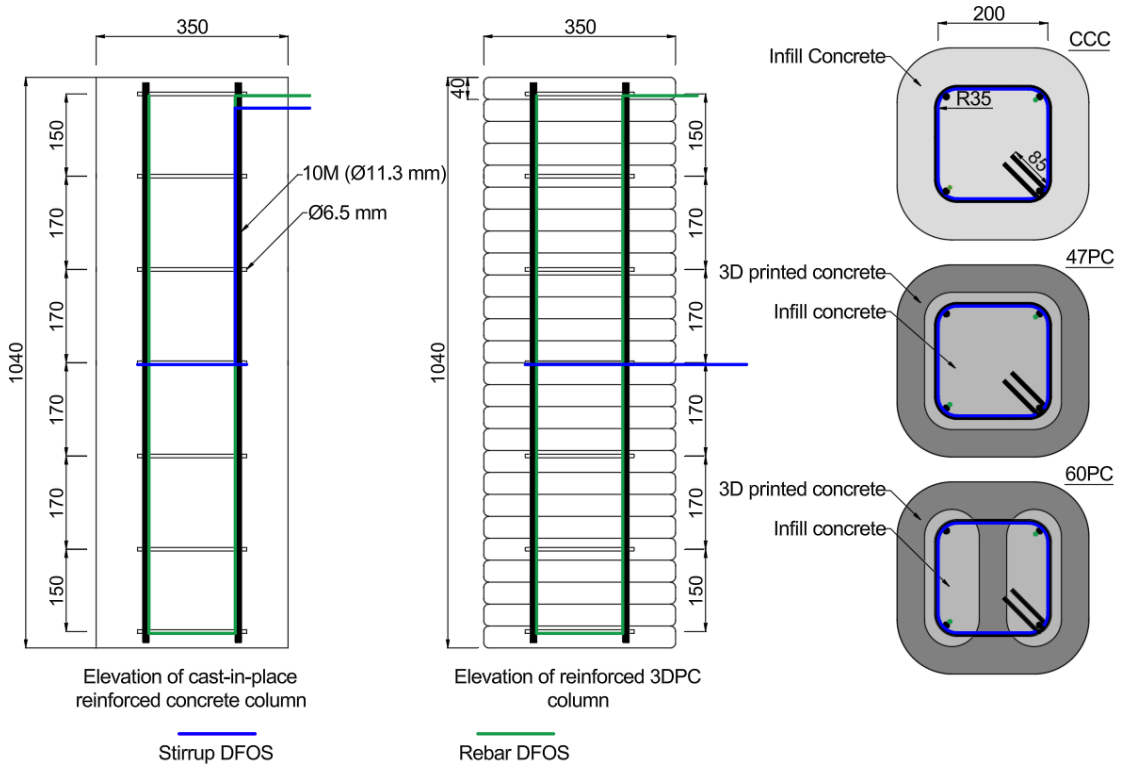
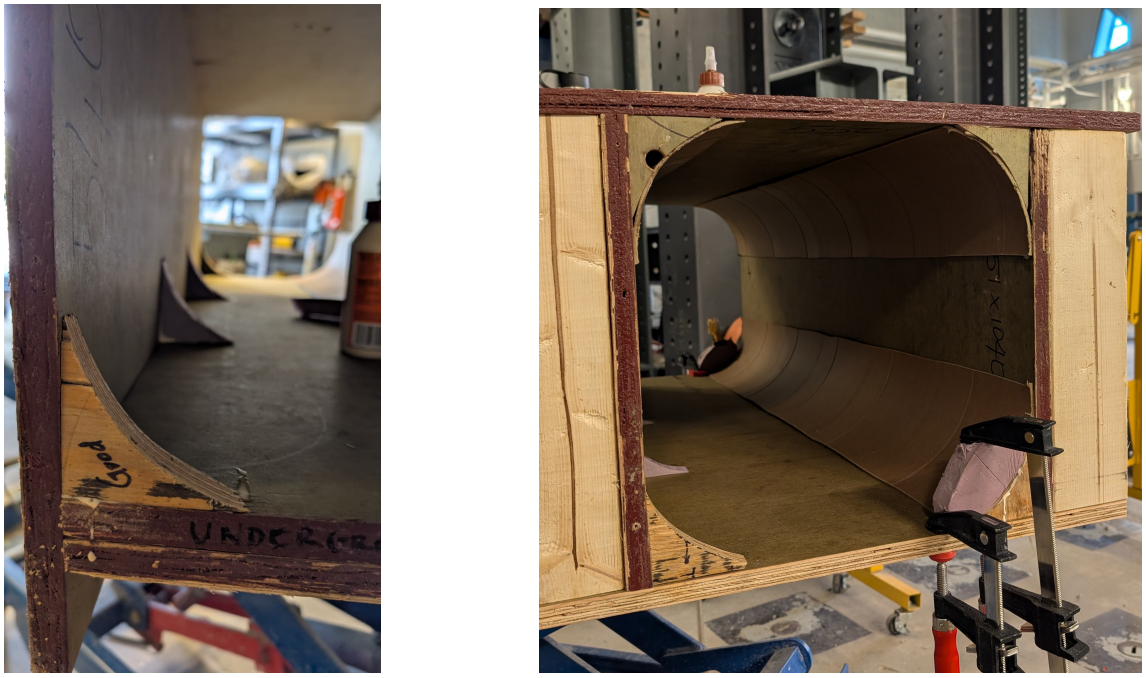


Figure 4.1: Elevation and cross-sections of all the reinforced concrete columns and the DFOS routing path

The vertical (longitudinal) reinforcement consisted of four 10 M deformed steel reinforcing bars, while 6.5-mm-diameter smooth bars were used as transverse ties. The minimum tie spacing was calculated in accordance with CSA A23.3-24 to prevent buckling-induced premature failure during the experiment. The required maximum tie spacing per the standards was 170 mm; therefore, ties were provided at 170 mm spacing. Two additional ties were provided at the top and bottom to prevent bending of the reinforcement near the loading and base plates, spaced 150 mm apart. Detailed design calculations for the large-scale columns are provided in the Appendix A.

The cast concrete columns (i.e., control specimens) used to establish baseline performance were

prepared with a cross-section identical to that of the 3dPC columns. However, due to the natural curvature at the edges for the 3DPC columns, the formwork for the cast columns needed to be fabricated with the exact fillet dimensions. As the first step, a square cross-section formwork measuring 350 mm was made using form boards. To achieve the required fillet radius at the corners, 4-inch ($\sim$100 mm) diameter Sonotubes of cardboard were cut into four equal vertical segments. To support the Sonotubes along the vertical length and to prevent buckling due to hydrostatic pressure from the concrete, corner pieces cut to form a fillet were placed at equal distances at all corners. The cut Sonotube segments were then glued to these pieces and allowed to set for 3 days. The formwork for the large-scale cast/control columns is shown in Figure 4.2. All formwork for the cast-in-place columns was placed side by side and attached to each other so they provided lateral support in one direction. To prevent breakage or buckling of the sides, additional supports were provided by 2" x 4" lumber, and the fully assembled formwork with the cast-in-place concrete is shown in Figure 4.3.



(a) (b)

Figure 4.2: (a) Corner pieces attached along the vertical height of the formwork to support the sonotube from buckling and (b) the attached sonotubes to form the fillet corners of the cast concrete columns



(a) (b)

Figure 4.3: The fully assembled formworks for the cast-in-place concrete with the additional supports in the lateral direction

4.1.2 Circular Reinforced 3DPC Columns

One constraint of the COBOD BOD2 commercial-grade printer used in this study is its minimum turning radius of 50 mm. Meanwhile, the compression testing machine used for circular column testing has a maximum horizontal and vertical clearance of 300 mm. Based on these constraints, the columns' overall dimensions were determined. The smallest plan dimension for the circular column, under the minimum-radius constraint, was 250 mm, determined by the minimum radius and the testing machine's horizontal clearance. The detailing of the reinforced concrete column was performed in accordance with CSA A23.3-24 (Canadian Standards Association, 2024), and the cross-section is shown in Figure 4.4. Detailed design calculations for the small-scale columns are provided in Appendix B.

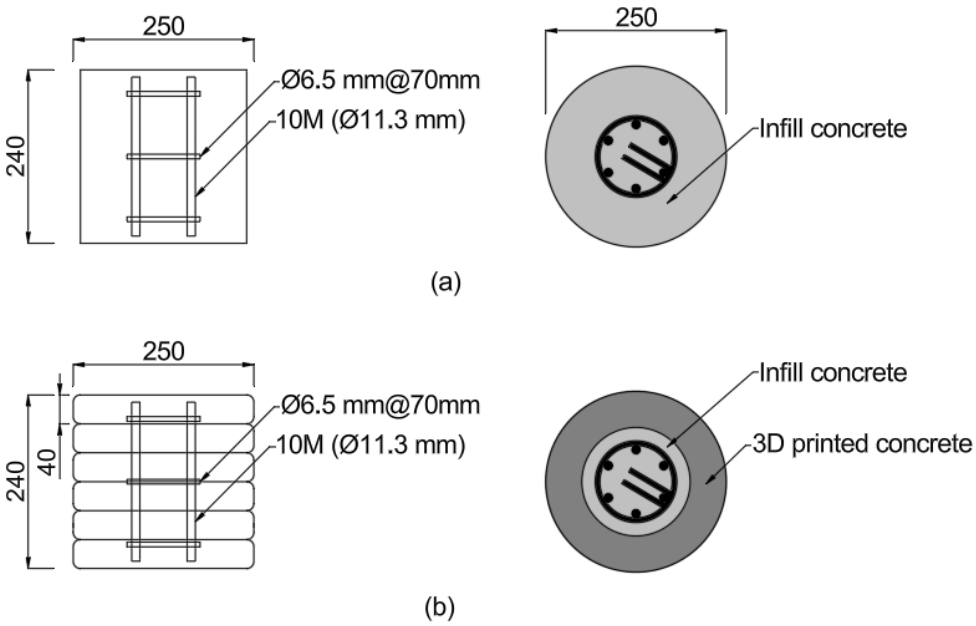


Figure 4.4: (a) Elevation and cross section of cast-in-place circular column and (b) Elevation and cross section of reinforced 3DPC column

The reinforcement cages for the cast specimens and the 3DPC columns were fabricated in the lab, using 10M ribbed reinforcing bars as the vertical reinforcement and 6.5 mm smooth bars as the transverse ties. The ties were made with closed loops at 135° hooks. The tie spacing was computed in accordance with CSA A23.3-24 (Canadian Standards Association, 2024) to provide sufficient confinement against buckling of the vertical bars. A small alignment jig was fabricated to ensure that all reinforcing bars for the circular columns were equally spaced and held vertically, as shown in Figure 4.5. Circular ties were then positioned at the required spacing, tied, and epoxied to hold them in place.

4.2 Specimen Fabrication and Printing Parameters

All 3DPC specimens were fabricated using a commercial gantry-type 3D concrete printer, the BOD-2, manufactured by COBOD International. This printer was designed for large-scale additive manufacturing in the construction industry and allows precise movement in all three directions. The print path was obtained by slicing the 3D model of the proposed columns. The 47PC columns were printed so that the starting point of each layer was not aligned with a vertical line but ran-



(a) (b)

Figure 4.5: (a) Alignment jig fabricated to hold the reinforcing bars in exact positions for the small reinforcing bar cage and (b) completed circular reinforcing bar cage for the circular columns

domised to prevent localised failure at the joint. The 3D printer nozzle was designed to imprint a zigzag pattern on the deposited layer to improve interlayer adhesion. The print parameters, such as print speed and layer-to-layer interval, were adjusted based on experience with the same printer to achieve optimal output.

The layer height was 40 mm, and the layer width was 50 mm. Consistent printing was achieved by introducing a stiffening agent at the printer nozzle, thereby increasing the stiffness of the cementitious mixture just before deposition. Shear vane and slump tests were conducted prior to pumping, and the results ranged from 10 to 12 kPa and 75 mm to 130 mm, respectively. In addition, to prevent layer collapse, the print speed was adjusted so that consecutive layers were printed in 7 seconds, providing sufficient time for early-age strength development to support the weight of successive layers.

The concrete mixture design used in this study is a proprietary mixture developed by the industry partner, Aretek (formerly Printerra Inc.). All 3DPC specimens were printed at the Climate-Data-

Driven Design (CD3) Facility for Built Infrastructure at York University's Keele Campus. The printer was housed in a fully enclosed (non-temperature-controlled) tent with the concrete mixer and pump stored outdoors. The 3DPC specimens were printed directly on a flat concrete surface covered with plastic sheeting to prevent them from bonding to the floor. The 3DPC specimens and companion cylinders, cubes, and prism specimens were covered with a tarp to prevent moisture loss and allowed to cure for 48 hours before infilling. After the concrete infill was poured, the specimens were covered again with plastic sheeting and allowed to cure for an additional 48 hours. The facility where the specimens were printed, along with the plastic wrap, was placed on the floor to prevent the concrete from sticking to it, and the printed specimens are shown in Figure 4.6.



(a) (b)

Figure 4.6: (a) The facility where the specimens were ready to be printed with the plastic wrap on the floor and (b) the printed specimens

The 47PC columns used in this research study allow the post-installation of a reinforcing cage into the printed permanent formwork. This approach was also used to incorporate the reinforcing cage into the small-scale circular columns. However, the geometry proposed for the 60PC columns in

this study will not allow a traditional reinforcing bar cage to be inserted from the top. Therefore, the ties were placed at the required spacing as the column was being printed. Figure 4.7 shows the fabrication sequence, which is a similar process adapted from Chen et al. (2023).



(a) (b) (c) (d)

Figure 4.7: Process of fabricating the optimised reinforced 3DPC columns: (a) the first layer is printed, (b) ties are placed on the first layer, (c) layers are continuously printed while the ties are placed at the required spacing, and (d) the final 3DPC columns

4.3 Instrumentation and Test setup

4.3.1 Large-Scale Square Columns

To measure strain in the reinforcing bars, two of the four vertical reinforcing bars (in opposite corners) in all specimens were instrumented with DFOS to obtain distributed strain measurements along their full length. In addition, the mid-height ties of the column were instrumented with DFOS to better understand their role in providing confinement. The accuracy of DFOS measurements depends on strain transfer from the material substrate to the optical fibre core. To ensure sufficient strain transfer, two-part high-strength epoxy resin was used. To attach the DFOS cables to the substrate, two parts of epoxy Gorilla Epoxy were used with a setting time of 5 minutes. The reinforcing bars were cleaned with sandpaper to remove loose rust and dust for proper adhesion, and the DFOS cables were laid in the required locations and secured with zip ties. Epoxy resin

was then applied to the bars, and the DFOS was adjusted to the correct position. The epoxy was allowed to cure for at least 24 hours. The DFOS cables were routed to the top, with both the dead end and the end to be spliced passed through protective tubing to prevent DFOS breakage during column casting. The attached DFOS cables, along with the fully prepared reinforcing bar cage and the final infilled 3DPC columns with protective sleeves for the DFOS cables to exit, are shown in Figure 4.8. Strain measurements were taken at a spatial resolution of 2.6 mm and an acquisition rate of 1.04Hz. The routing of the DFOS cables to obtain the strain levels is shown in Figure 4.1.



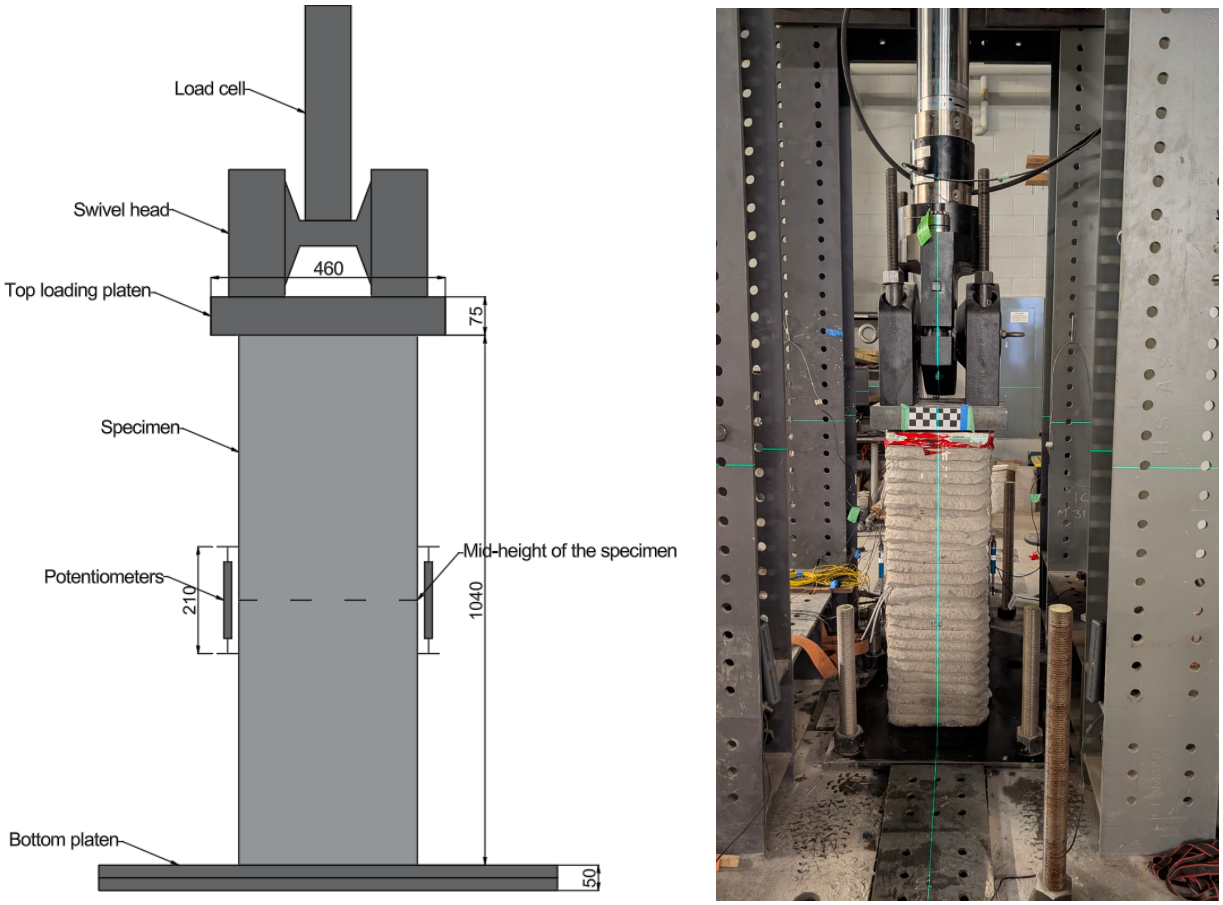
(a) (b) (c)

Figure 4.8: (a) Epoxied DFOS cable to the vertical reinforcing bar, (b) Completed reinforcing bar cage for the square columns, and (c) the final infilled 3DPC columns with the protective sleeves for the DFOS to exit the columns

To measure concrete surface strain, three spring-loaded linear potentiometers (Penny and Giles, stroke length 100 mm) were used to measure the relative displacement between two points on the left and right sides of the columns, with a gauge length of 210 mm. The potentiometer attached to the back side of the columns had a stroke length of 150 mm and was used to measure relative displacements between two points with a gauge length of 300 mm. The potentiometers were placed at mid-height on the columns and centred on the sides.

To obtain a flat loading surface and ensure uniform stress distribution during axial loading, hydrostone gypsum cement was applied to the surface to a thickness of 5-10 mm. To keep the hydrostone from spilling over the column, duct tape was used to build up to the required height and prevent spillage. The gypsum cement was allowed to cure for 24 hours before loading to ensure adequate strength development.

The axial compression tests on the reinforced concrete columns were conducted using a servo-hydraulic actuator system operating under closed-loop displacement control. This research study used a DuraGlide 201.70 Hydraulic Actuator with a capacity of 1500 kN. The test setup, along with attached potentiometers at the sides of gauge length 210 mm, is provided in Figure 4.9a, and the actual test setup is shown in Figure 4.9b.



(a) (b)

Figure 4.9: (a) Schematic of the test setup for the large column specimens (the potentiometer attached to the back is not shown in the schematic) and (b) the actual test setup

The loading rate for the specimens was established through a trial-and-error approach to ensure sufficient data acquisition while maintaining the requirements of quasistatic loading. The applied loading rate was controlled by the actuator head displacement rate; however, the actual loading rate experienced by the columns differed due to the interaction between the applied load and the response of the 4-post loading frame. A displacement rate of 0.3 mm/min was ultimately selected for all large-scale column tests. However, directly replicating this loading rate in similar experimental setups may not yield identical results due to variations in testing configurations, system stiffness, and load transfer mechanisms.

The potentiometers and the actuator were all connected to a single data acquisition unit. To ensure that the load applied was concentric to the centroidal vertical axis of the column, a laser level was used to align the column to the shaft of the actuator as best as possible by placing the laser facing the front face of the column, then to the side of the column, and finally again on the front face of the column. In addition, images of the front sides of the columns were captured using a Canon EOS 5DS R at 8688 x 4888 pixels and 0.1 Hz for use in Digital Image Correlation (DIC).

4.3.2 Small scale circular columns

Two linear Novotechnik TR-0025 potentiometers with a 25 mm working range and an accuracy of ± 0.05 mm were attached at mid-height, with a gauge length of 80 mm, to measure the axial shortening. An LVDT was also attached to the bottom moving plate to measure the overall axial shortening of the column. In addition to all the physical measuring devices, DIC was implemented. The test setup for the small column is shown in Figure 4.10 along with the attached potentiometer on the specimen as well as the one attached to the bottom platen.

The test was conducted using the Controls 50-A52Z00 universal compression testing frame with 3000 kN capacity and a 4-welded column frame for high stiffness. The machine is equipped with a swivel head at the top to ensure concentric load application on the specimen. Meanwhile, top and bottom loading platens with thicknesses of 35 mm and 50 mm were used to increase stiffness and



(a) (b)

Figure 4.10: (a) Potentiometer attached to the circular column (b) the compression test setup with all the physical measuring devices

prevent bending of the loading platens during the tests. The schematic of the test setup is given in Figure 4.11. To determine the optimum loading rate for data collection and satisfy the requirement of a quasistatic loading scenario, the CCC_{03} column was tested multiple times with different loading rates before it failed. As a result of multiple loading cycles, the stiffness degraded during testing; therefore, it was excluded from any analysis.

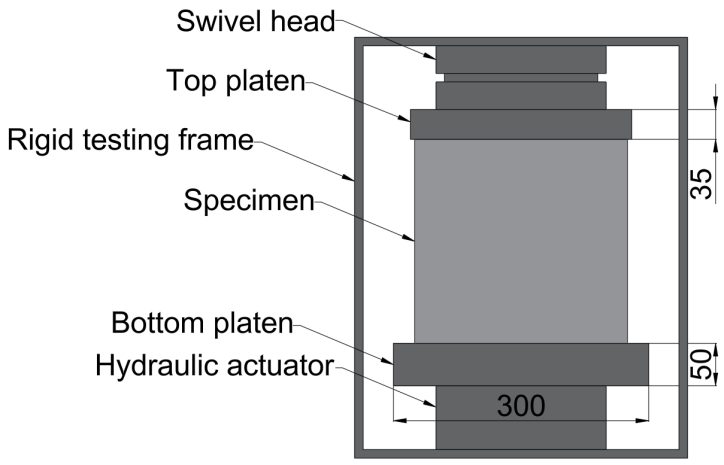


Figure 4.11: The schematic of the CONTROLS A52Z00 compression testing machine

4.4 Experimental results and discussion

4.4.1 Axial load response of small-scale circular columns

The axial shortening of the circular columns was measured using two approaches: potentiometers and a custom-scripted, computer-vision-based Virtual Potentiometer (VP) for the 3DPC columns.

For the cast columns, potentiometers were only attached directly to the specimen at mid-height; however, their readings began to deviate significantly shortly after the tests were initiated, in a similar manner to the observations reported by Bates and Aslani (2025), even though no visible cracking or local damage was observed near the attachment points or elsewhere on the column at the time of deviation. This indicated that the attached potentiometers were not reliably capturing the full displacement response up to the point of failure. The captured potentiometer readings along with the axial load resistance plots of the cast-in-place columns and 3DPC are provided in Appendix G. Consequently, for subsequent tests on 3D-printed circular columns, an additional potentiometer was mounted on the loading plate to record the overall axial displacement. The plate-mounted potentiometer readings were then verified against VP-based displacement tracking, yielding good agreement. The difference between the VP and potentiometer readings as a percentage of the potentiometer readings is shown in Figure 4.12.

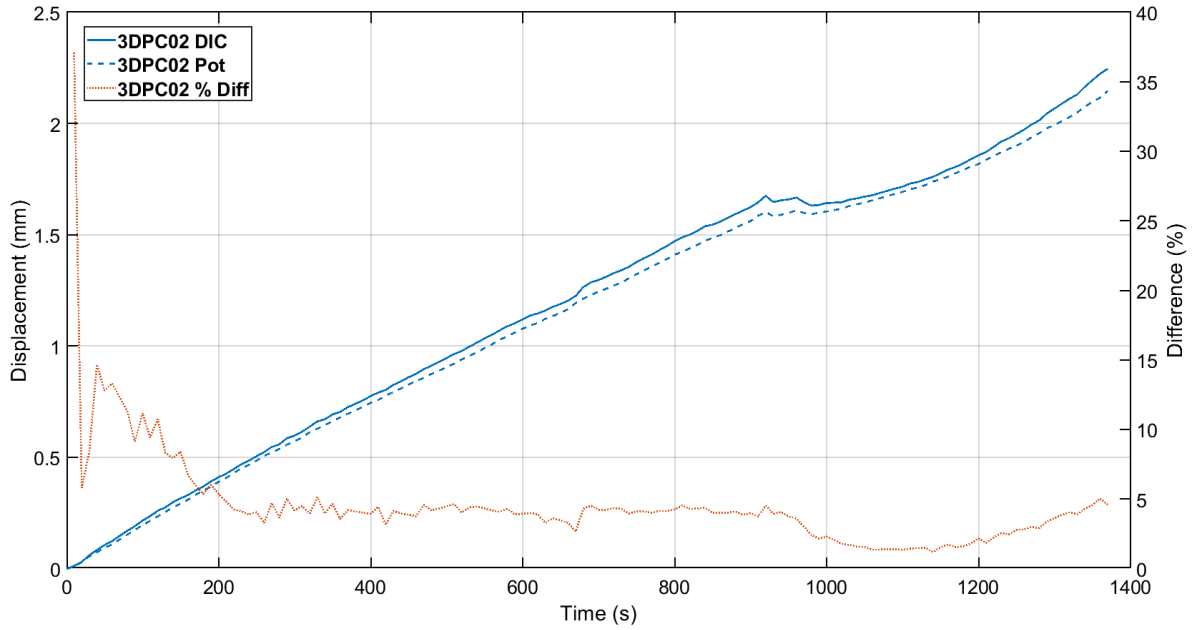


Figure 4.12: Potentiometer measurement vs virtual potentiometer measurement and the percentage difference of VP measurement to potentiometer readings

Given that the overall error at large displacements has converged to acceptable levels, the deformations were measured as an overall shortening of the columns using the VP for the cast-in-place

columns, and the response is shown in Figure 4.13. The 3DPC columns failed at an average load of 1727 kN, which is 4.5% lower than the cast-in-place columns, which failed at an average load of 1808 kN. In addition, the cast-in-place columns failed suddenly after reaching peak axial load-carrying capacity, while the 3DPC columns failed gradually, suggesting greater ductility.

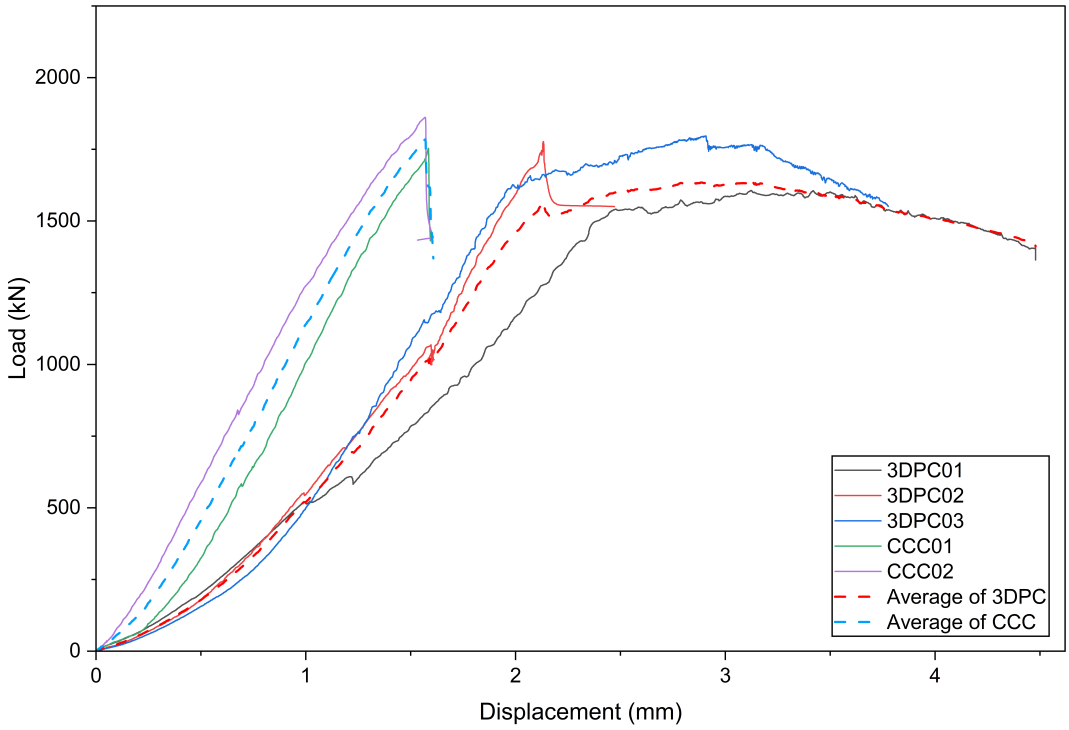


Figure 4.13: Axial load vs overall shortening measured using the VP for both circular and 3DPC columns

In addition to the peak load comparison, initial stiffnesses of the cast-in-place and 3DPC columns were compared. However, since the axial load response is measured against the displacement of the loading plate (as in Figure 4.13), which captures the inherent behaviour of the hydrostone, the stiffness of the linear region past the concave-up response was considered for the axial stiffness calculations. The secant stiffness determined using this approach and the average stiffness values are given in Table 4.1. The 3DPC columns have 34.6% lower mean axial stiffness than their cast-in-place counterparts. This reduction in stiffness could be attributed to the lower stiffness of the printed material resulting from the layer-by-layer deposition process and the associated porosity introduced during printing. Consequently, for similar applied load, the 3DPC columns exhibit greater

axial deformation than the cast-in-place specimens, reflecting their lower resistance to elastic compression.

Table 4.1: Initial stiffness of the small-scale circular columns

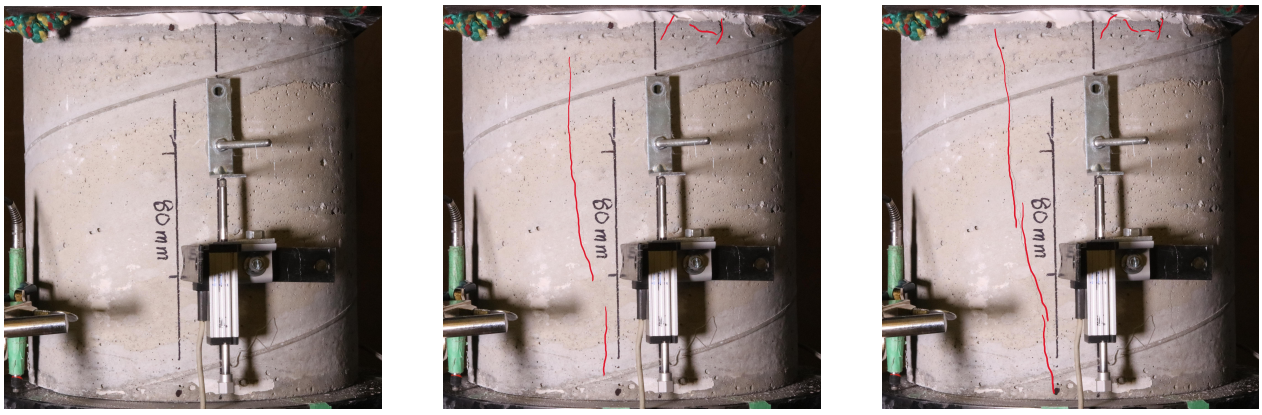
Specimen	Initial stiffness (kN/mm)	Mean stiffness (kN/mm)
CCC_{01}	1366.95	1431.77
CCC_{02}	1496.59	
$3DPC_{01}$	955.28	935.87
$3DPC_{02}$	1092.8	
$3DPC_{03}$	759.53	

CCC_{03} specimen was tested multiple times and therefore was excluded from determining the stiffness

4.4.2 Failure mechanism of circular columns

The failure mechanisms of the circular columns were monitored throughout the tests and subsequently verified using front-view images. The cast columns initially exhibited vertical cracking at the mid-height of the column, although the load at which the first visible crack appeared varied between specimens. CCC_{01} developed its first crack at approximately 600 kN, whereas CCC_{02} remained uncracked (no visible cracks) until approximately 1300 kN. Multiple vertical cracks started to open on different sides of the columns as the load increased, and the cracks propagated vertically as the load increased. CCC_{01} failed shortly after crack propagation at a load of 1786 kN, while CCC_{02} developed additional cracks near the bottom and subsequently at the top of the column. These cracks widened significantly at approximately 1560 kN, leading to failure at around 1700 kN. The overall failure of the columns could be described as a sudden drop in load resistance soon after reaching the peak load. The development of cracks on the CCC_{01} column is shown in Figure 4.14.

In contrast, the 3DPC circular columns exhibited a distinctly different failure pattern. Initial cracking occurred primarily along the bottom printed layer, where multiple cracks developed and the pieces of cracked concrete began to spall off at loads between 580 and 600 kN. As the load in-

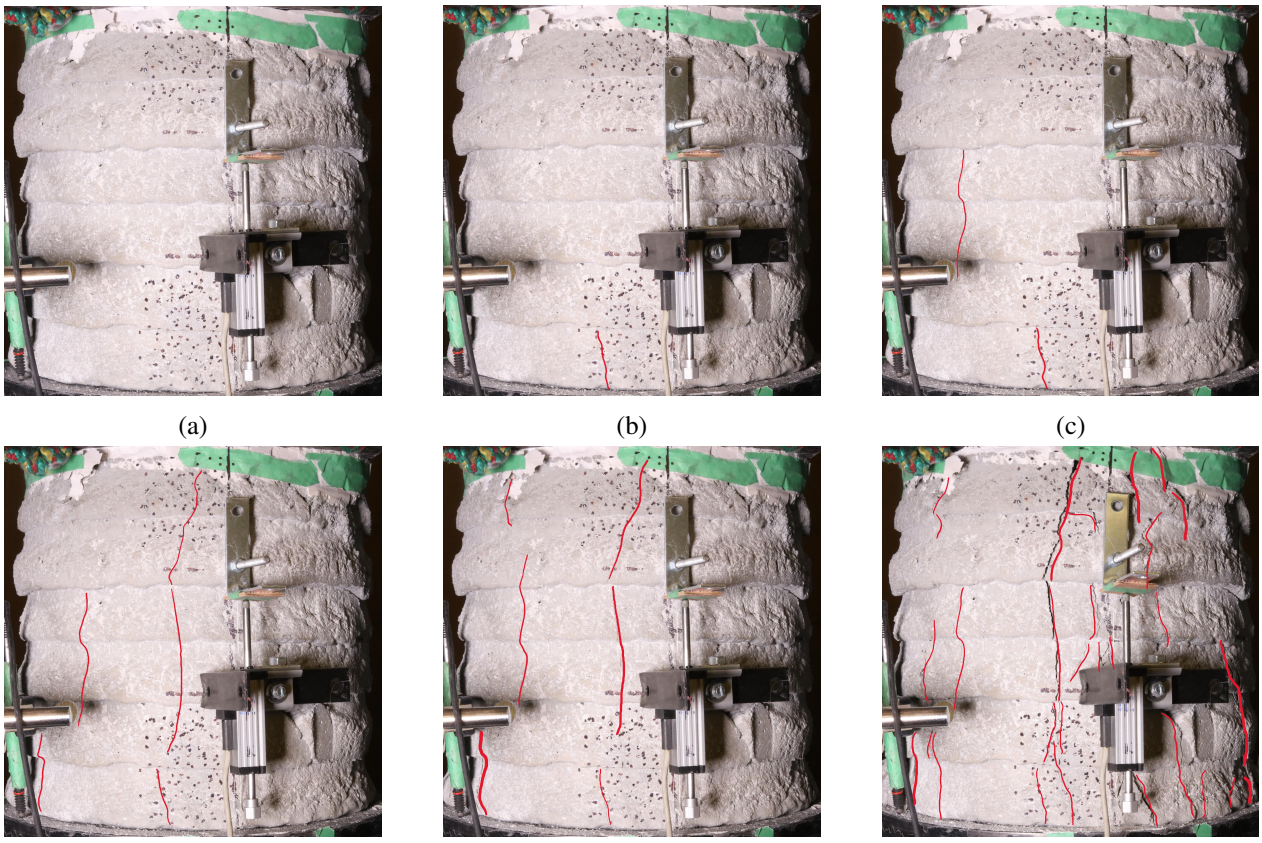


(a) (b) (c)

Figure 4.14: Failure mechanism and crack propagation in cast circular columns under uniaxial compression loading

creased, additional cracks formed predominantly near the lower layers, accompanied by noticeable lateral expansion of the bottom layer at approximately 640 kN. This observation could result from insufficient transverse reinforcement to prevent lateral deformation near the top and bottom surfaces. Further cracking was observed near the top of the column, while progressive spalling of concrete occurred in the lower layers due to continued lateral expansion, particularly at loads around 1400 kN. At approximately 1540 kN, a significant increase in cracking was observed near the base, and cracks began to develop at the mid-height of the column on different sides of the column. By 1560 kN, the concrete at the top of the column also began to spall. This may be because there are no reinforcing bars in the top 20 mm of the space, and the concrete may be crushing due to a lack of lateral confinement. Subsequently, the columns ultimately failed after sustaining the peak load for a longer duration than the cast circular columns, indicating a more progressive failure process. This response is similar to that observed in a study of reinforced concrete columns fabricated using 3DPC as a permanent formwork by Bates and Aslani (2025). The crack formation and propagation in the 3DPC columns are shown in Figure 4.15. Meanwhile, Figures 4.16 and 4.17 show the post-failure states of the cast-in-place and 3DPC columns, respectively.

All the small-scale circular columns were designed and detailed in accordance with CSA A23.3, with axial load resistance of $P_{ro} = 2569$ kN and $P_{rmax} = 2055$ kN (the calculation sheet is attached



(a) (b) (c)

(d) (e) (f)

Figure 4.15: Failure mechanism and crack propagation in circular columns with 3DPC as permanent formwork



(a) (b) (c)

Figure 4.16: Post-failure state of the cast-in-place columns (a) CCC_1, (b) CCC_2, and (c) CCC_3

in Appendix B). However, during testing, the cast columns failed at an average load of 1808 kN, and the 3D-3DPC columns at 1727 kN, which are 88% and 84%, respectively, of the predicted



(a) (b) (c)

Figure 4.17: Post-failure state of the 3DPC columns (a) $3DPC_1$, (b) $3DPC_2$, and (c) $3DPC_3$

capacity of the small-scale circular cast columns as per CSA A23.3. One printed and one cast column were dissected to examine the core, inspect the reinforcing bars for buckling, and ensure that the placement of the reinforcing cage and the ties was as expected. During the inspection of these columns, no buckling of the reinforcing bars was observed in either the cast-in-place or 3DPC columns, and the reinforcing cage was positioned as planned. The images of the dissected columns are provided in Figure 4.18.

4.4.3 Axial load response of large-scale square columns

The axial displacement was captured using three potentiometers attached to the faces: the left and right potentiometers have a gauge length of 210 mm, while the potentiometer attached to the back face of the columns has a gauge length of 300 mm. Therefore, the back potentiometer was converted to the corresponding strain and the displacement for a gauge length of 210 mm was used to calculate the average displacement of the columns. The average load-displacement responses for the CCC, 47PC, and 60PC columns are shown in Figure 4.19. The CCC3 and 60PC3 columns were tested multiple times, and only the results of the final test run were collected (as shown in the figure).



(a) (b)

Figure 4.18: Images of the columns that were cut open to inspect any causes for reduced axial load capacity of the small-scale circular columns

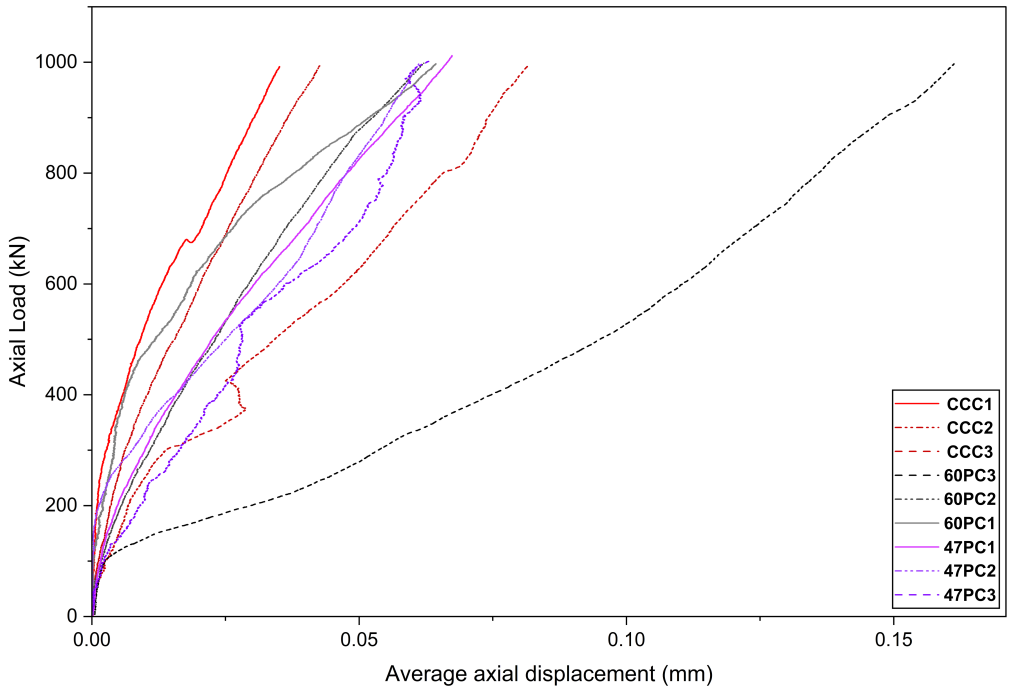


Figure 4.19: Axial load - average displacement response of CCC, 47PC, and 60PC columns

Visual inspection during testing showed no visible cracks in any column after loading up to 1000 kN. The axial stiffness of reinforced concrete columns is an important parameter that can affect

a structure's deformation response at service load levels. It represents the resistance of a column to axial shortening prior to the onset of significant cracking, crushing, or other nonlinear material behaviour. A higher initial axial stiffness results in smaller axial deformations under a given load, which can influence load distribution among structural members, overall structural stability, and serviceability performance. In multi-storey buildings, column axial stiffness affects vertical shortening, differential settlement between structural elements, and the interaction between columns, walls, and floor systems. Due to actuator capacity limitations, the columns could only be tested to a maximum load of 1000 kN. Therefore, the initial stiffness is taken as the secant stiffness of the load-deformation response of 3DPC columns and is compared with that of cast-in-place columns. The calculated secant stiffness values are provided in Table 4.2. The CCC columns were found to have the highest axial stiffness of 29829 kN/mm, while the 47PC columns provided an axial stiffness of 15655 kN/mm (48% lower compared to cast columns) and the 60PC columns exhibited an average axial stiffness of 16596 kN/mm (45% lower compared to cast columns). The reduced stiffness values were as expected, since the modulus of elasticity of the 3DPC is lower than that of CCC columns, and reducing the volume percentage of cast-in-place concrete reduces the contribution from a stiffer material, resulting in reduced overall column stiffness.

Table 4.2: Initial stiffness of the square columns was determined using the load-deformation response

Specimen Type	**Secant Stiffness (kN/mm)**		
	Specimen 1	**Specimen 2**	**Specimen 3**
CCC	30611	29047	13960*
Mean		29829	
47PC	15025	16188	15753
Mean		15655	
60PC	16902	16289	7264*
Mean		16289	

* Specimens were tested more than once and were not considered during the calculation of the mean stiffness

4.4.4 Strain distribution along the ties

The DFOS was epoxied to the tie at mid-height of each column, enabling measurement of the strain distribution along the tie over its full bonded length. However, for visualisation, only a bonded length of 100 mm was used on all four sides. Since both the DFOS measurements and actuator load data shared the same time domain, the strain for each load step was obtained via interpolation. Strain values at five distinct load levels, 20%, 40%, 60%, 80%, and 100% of the peak load, were then extracted, and the strain over the 100 mm was plotted, and the average strain ($\mu m/m$) over this length was marked in the produced plots. All the plots that were produced in this section are drawn to scale.

The strain distributions measured on the ties of the CCC columns are shown in Figures 4.20 and 4.21. In general, the strain remained relatively uniform along the bonded length on each side. However, slight differences in average strain between the four sides were observed, indicating that one side of the ties experienced slightly more strain than the other sides. This variation is likely attributable to minor accidental eccentricities in loading introduced during testing, which caused different degrees of concrete dilation.

Similar observations were made with the strain distribution obtained for the ties from the printed column with 47% 3DPC (Figure 4.22 and Figure 4.23) and for the ties from the printed column with 60% 3DPC, shown in Figure 4.24. The tie strain distribution for one of the optimised columns was unavailable for analysis, and the strain distributions for columns tested more than once were excluded from the analysis.

At 100% of the applied load, the cast concrete columns experienced a maximum average strain of 76.5 microstrain and a minimum of 67 microstrain, while the printed column, 47%PC, experienced a maximum strain of 89 microstrain and a minimum of 85 microstrain. This indicates that the volumetric expansion in the 3DPC columns is higher than in the cast columns, which correlates with the reduced stiffness and higher strain observed in the longitudinal reinforcing bars in the

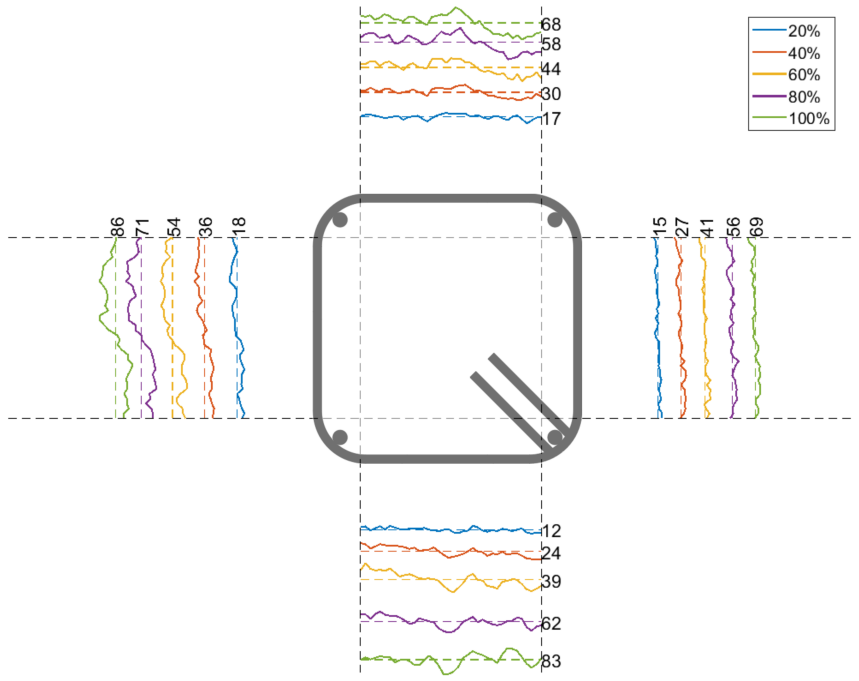


Figure 4.20: Strain distribution around the tie placed at the mid height of column CCC_1 and the average strain values over the bonded length at each loading step

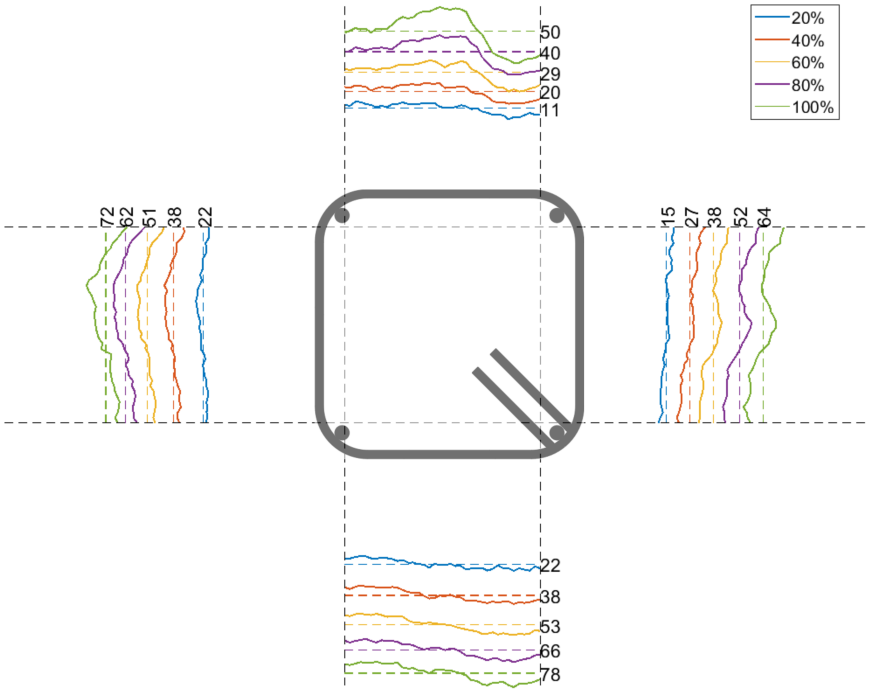


Figure 4.21: Strain distribution around the tie placed at the mid height of column CCC_2 and the average strain values over the bonded length at each loading step

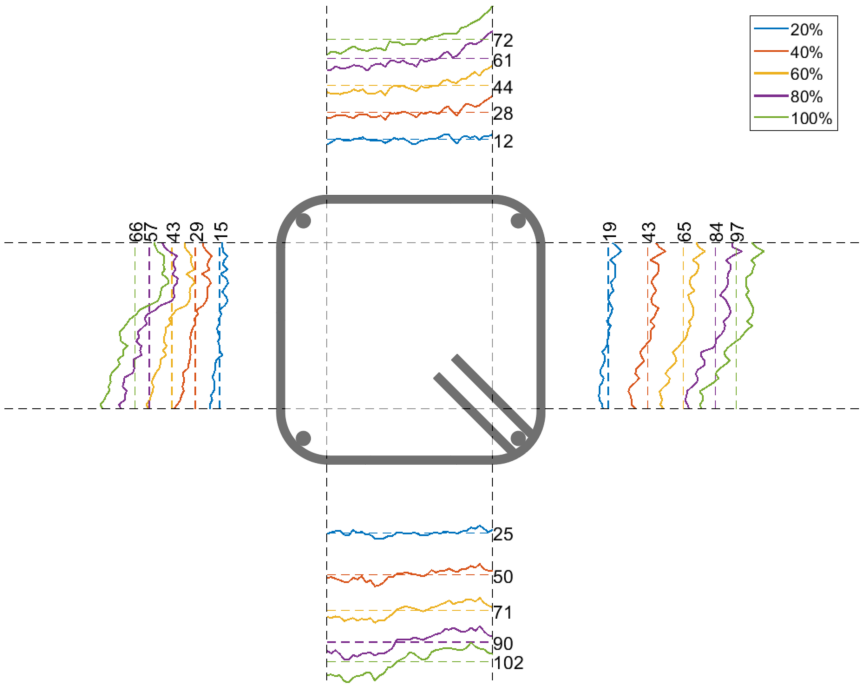


Figure 4.22: Strain distribution around the tie placed at the mid height of 3DPC column 47PC_1 and the average strain values over the bonded length at each loading step

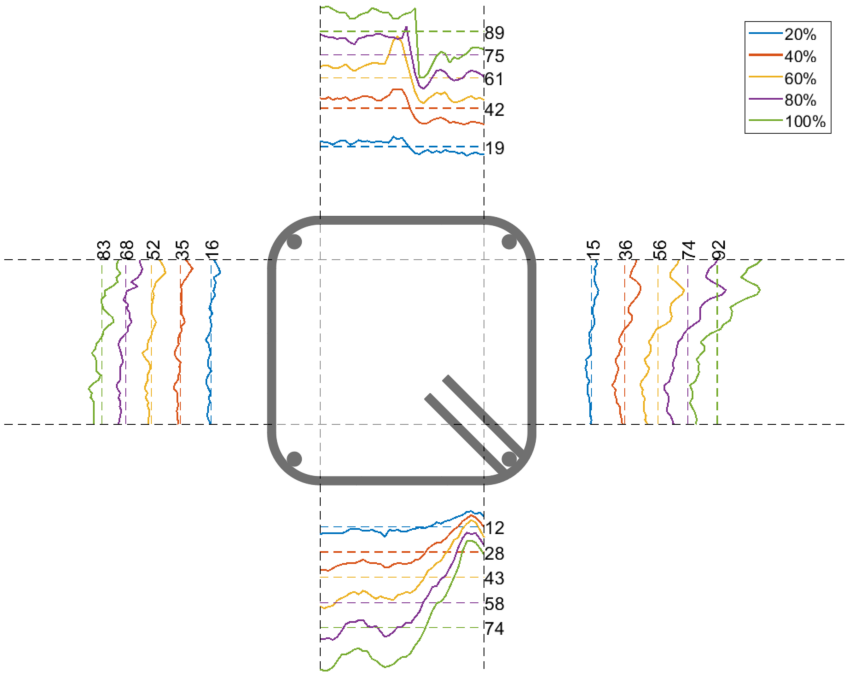


Figure 4.23: Strain distribution around the tie placed at the mid height of 3DPC column 47PC_2 and the average strain values over the bonded length at each loading step

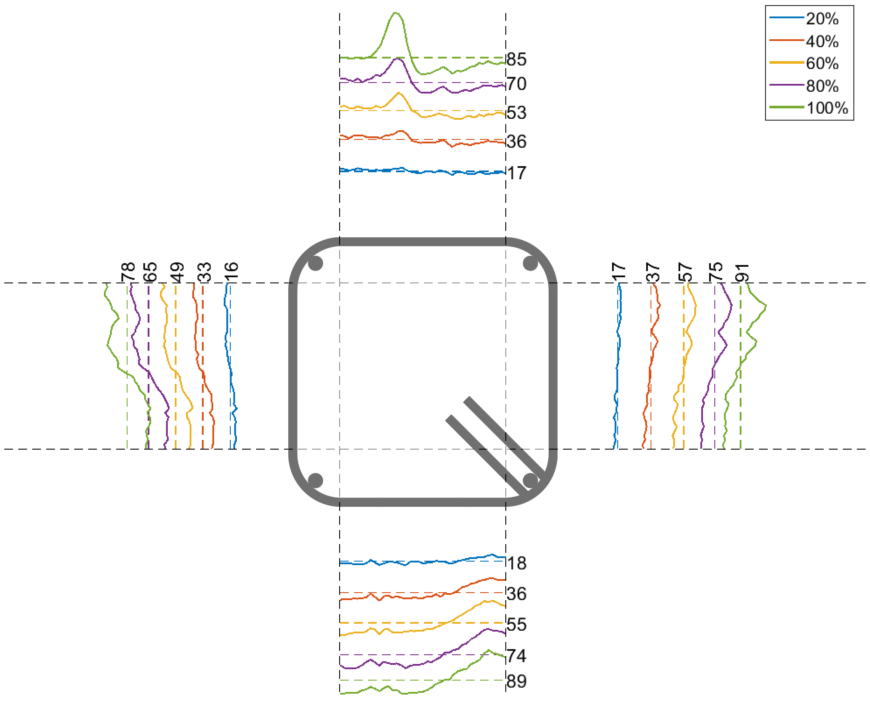


Figure 4.24: Strain distribution around the tie placed at the mid height of the 3DPC column $60PC_2$ and the average strain values over the bonded length at each loading step

3DPC. These increased strains could result in increased vertical crack formations, which may lead to column failure. Meanwhile, the printed column, 60%PC, experienced an average strain of 86 microstrain.

4.4.5 Strain distribution along the vertical reinforcing bars

To capture the strain distribution along the vertical reinforcing bars in the reinforced concrete columns, DFOS cables were mounted along the reinforcing bars as described in section 4.1. Some data from these DFOS cables were unavailable for analysis due to cable damage during printing and subsequent transportation, a downside of using DFOS cables for strain data acquisition.

Overall, the strain distribution along the reinforcing bars was similar in shape from top to bottom of the bonded length across all the test specimens regardless of the type of specimen. Higher strain levels were observed near the top and bottom ends of the reinforcing bars compared with the mid-height region. This is likely attributable to direct interaction between the reinforcing bars and

the loading plates, where contact forces may have induced localised stress concentrations at the specimen ends, causing peaks in the strain measured by the DFOS. In contrast, the strain measured at mid-height of the reinforcing bars is considered more representative of the strain transferred from the surrounding concrete, as it is less influenced by end effects. This supports the decision to attach the surface-mounted potentiometers near mid-height of the specimen to measure strain in the concrete. Only two diagonal bars were instrumented in this testing due to the capacity limitations of the maximum number of DFOS that could be connected to the data acquisition system.

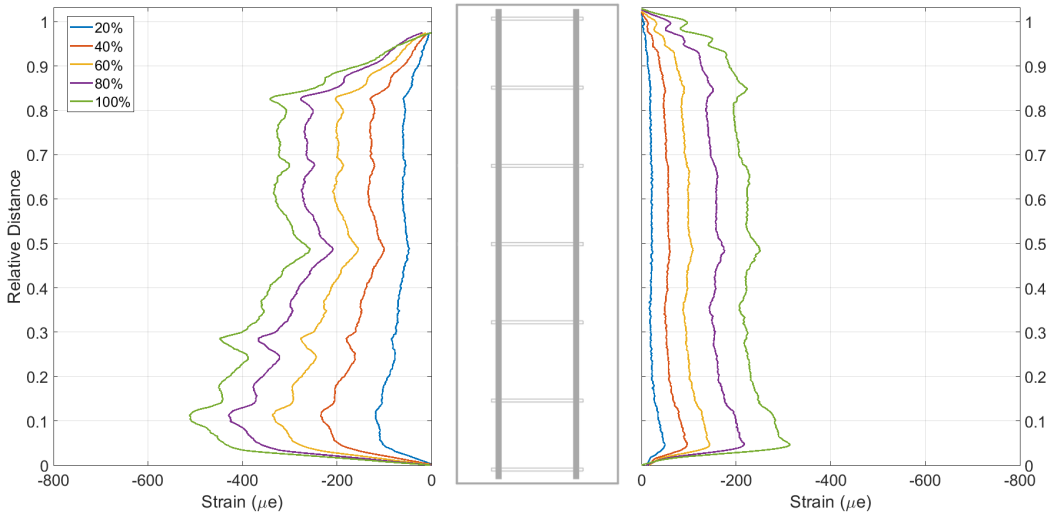


Figure 4.25: Strain distribution along the two diagonal vertical reinforcing bars in Cast Concrete Column (CCC_1)

It could be noted that the strains observed within the mid-height of the columns are within a range of 200 microstrain to 350 microstrain for CCC columns (as shown in Figure 4.25), whereas the strains observed for 47PC columns are within a range of 350 microstrain to 500 microstrain (as shown in Figures 4.26 and 4.27)and for the 60PC columns, the strain is within the range of 400 microstrain to 450 microstrain (as shown in Figure 4.28). This increase in strain in the reinforcing bars, compared to the cast concrete columns, is consistent with the previously observed trend in displacements measured from the attached potentiometers, further supporting that the readings from the surface-mounted potentiometers accurately captured the columns' behaviour.

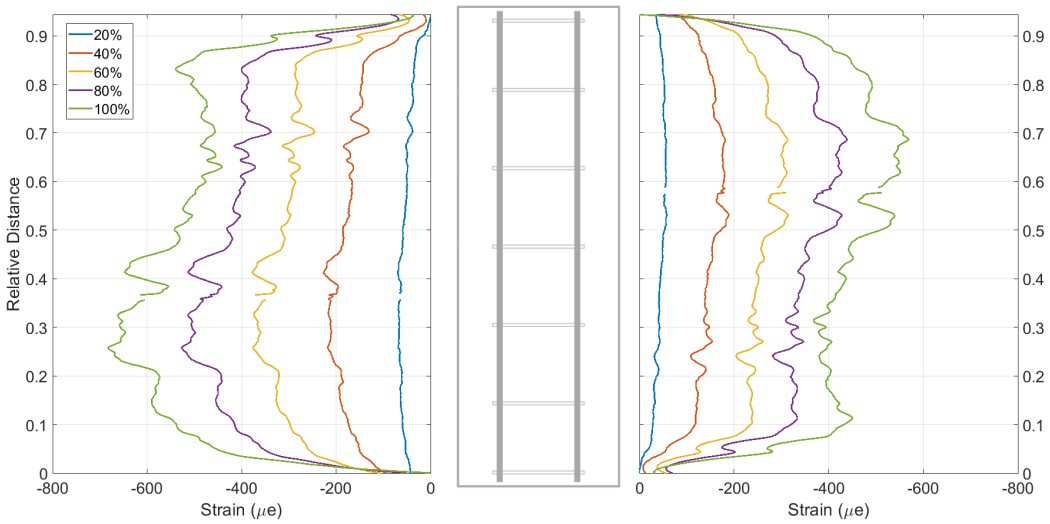


Figure 4.26: Strain distribution along the two diagonal vertical reinforcing bars in 47PC_1

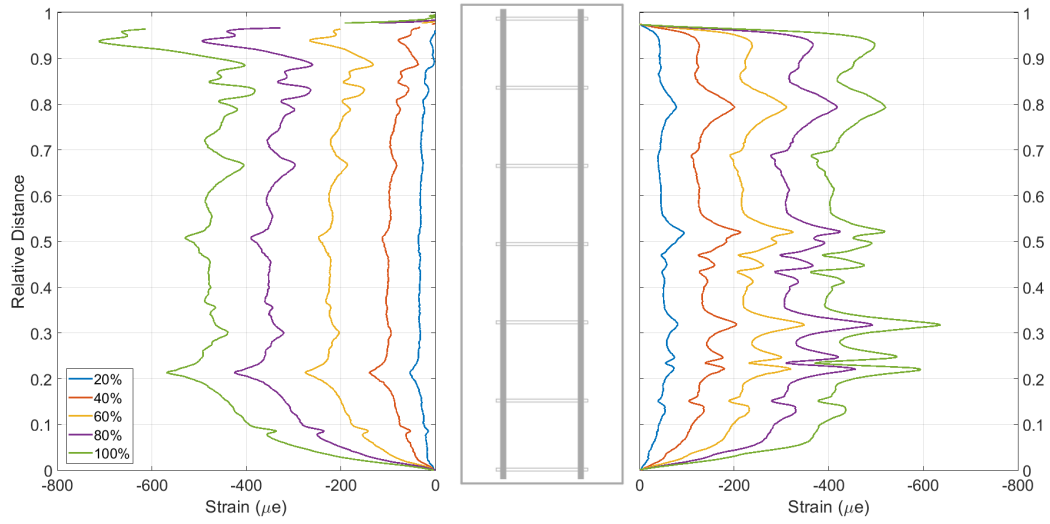


Figure 4.27: Strain distribution along the two diagonal vertical reinforcing bars in 47PC_2

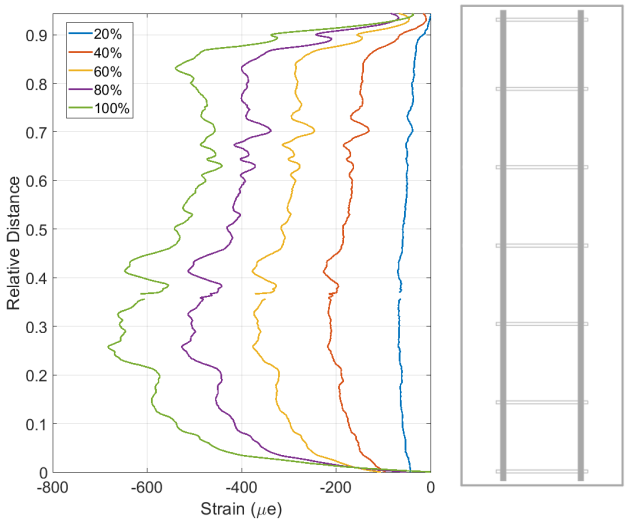


Figure 4.28: Strain distribution along the vertical reinforcing bar of $60PC_2$

4.5 Summary and conclusions

This chapter presented the experimental results obtained for the reinforced concrete, both square and circular, columns that were proposed in this research study to understand the behaviour of the columns under uniaxial compression loading and also to understand the load sharing between different materials in the 3DPC columns, which are the infill concrete, 3DPC, and reinforcing steel bars.

Given the capacity restraints of the hydraulic testing system, the large-scale square columns were tested up to a maximum load of 1000 kN. The small-scale circular columns were tested until failure. Similar cast-in-place columns with comparable reinforcement ratios and geometry were fabricated to establish baseline parameters. Further, an optimised geometry was proposed for the square column (60PC), increasing the amount of 3DPC by 13% compared to the 47PC columns, thereby increasing print efficiency and reducing construction time.

Upon comparing the failure mechanism of the small-scale circular columns, the cast and 3DPC columns exhibited distinctly different failure mechanisms. The cast columns primarily developed vertical cracks near the middle that propagated as load increased, resulting in a relatively sudden

loss of load-carrying capacity upon failure. In contrast, the 3DPC columns exhibited a more distributed cracking pattern near the bottom, characterised by the formation and progressive widening of multiple cracks, particularly along the printed layers. Rather than experiencing an abrupt drop in load capacity, the 3DPC columns sustained the applied load longer after extensive crack development before eventual failure. This behaviour suggests a more gradual failure process in the 3DPC columns, indicating post-peak load resistance compared to the cast columns. This behaviour was also observed in a similar study by Bates and Aslani (2025), where 3DPC columns exhibited a more gradual post-peak response than cast-in-place columns. In a compression loading experiment conducted on similar reinforced composite specimens made using printed permanent formwork infilled with conventional concrete by Zhu et al. (2021), 3DPC columns exhibited higher load-carrying capacity than the counter cast-in-place companion columns, which was associated with the additional confinement provided by the printed layer to the core. Given this observation and the understanding that passive confinement enhances ductility, the confinement mechanism contributed to the specimen's improved deformation capacity.

The readings from the potentiometers attached to the surfaces of the circular columns deviated, producing unreliable data regardless of column type at lower load levels. Therefore, the subsequent analysis used overall column shortening measured by bottom-plate displacement. However, due to the presence of the Hydrostone, the columns exhibited concave-upward load-deformation behaviour, which was more pronounced in the 3DPC column than in the cast concrete column (as shown in Figure 4.13). Given the available knowledge of the behaviour, it was treated as behaviour induced by the Hydrostone rather than by the 3DPC columns.

The axial load capacity of the cast-in-place columns from the experiment was 88% of the predicted axial resistance of a circular column as per CSA A23.3, which is 2055 kN, while the 3DPC columns exhibited an axial load resistance of 1727 kN, which is 4.5% lower than the experimental capacity of the cast-in-place counterpart and 84% of the capacity prediction based on CSA A23.3.

In contrast, the square columns tested to a maximum load of 1000 kN showed no visible cracks dur-

ing the experiment. Since the columns were not tested beyond the stage of yielding of the reinforcing steel, the initial axial stiffness, which influences the amount of axial shortening under service loading, was determined by calculating the secant stiffness obtained from the load-deformation response. The axial deformation was calculated as the mean of the potentiometer readings from the three potentiometers attached to the column surface. The stiffness of 47PC is 48% lower, and that of 60PC is 45% lower, compared to the stiffness of CCC columns.

Chapter 5 Fibre Section Analysis

This chapter describes the methodology used to analyse the experimental data collected from the large-scale square columns. To compare the 3DPC columns with the cast-in-place columns, a modified fibre section analysis was proposed, using experimentally measured potentiometer displacements as input to determine the strain field across the cross section. This analysis method not only quantifies any accidental eccentricity introduced into the column during testing, but also eliminates deviations in axial load resistance resulting from moments induced by the accidental eccentricity. Initially, the cast-in-place columns were used to determine the fit of the constitutive models used for the infilled concrete and vertical reinforcing bars. Later, three different stress-strain responses obtained from different specimens were used as three alternative constitutive models for the 3DPC material, and a best-fit material model was chosen using this modified fibre section analysis. This model was also used to determine the axial load contribution by the corresponding constituent materials of the columns, which is one of the main objectives of this research study. Using the verified material constitutive models, fibre section analysis under pure compression was used to estimate the ultimate capacity of the large-scale columns, which were then compared to the prediction based on CSA A23.3 (Canadian Standards Association, 2024).

5.1 Methodology

Fibre section modelling is a widely used analytical approach for reinforced concrete for simulating the non-linear behaviour of cross-sections of elements such as beams and columns. In this research study, the analysis was conducted by dividing the section into individual "fibres" belonging to different materials, such as 3DPC, infill concrete, and reinforcing steel, used in the fabrication of the reinforced concrete columns. The strain compatibility condition was assumed, along with the assumption that plane sections remain plane during loading. In contrast to the traditional fibre section analysis, where forces and moments are calculated at incremental displacements (or strain values), a modified fibre section analysis was developed in which the experimental displacement

was used to determine the strain field at mid-height of the column. This modified fibre section analysis method was used to eliminate errors arising from accidental eccentric moments during testing. The stresses were then determined using the corresponding non-linear constitutive models obtained from material testing, and the axial force contributions of the individual materials were integrated over the entire section to evaluate the accidental eccentric moments. This modified approach not only improves understanding of the load contribution of the materials, but also enables the generation of the structural behaviour of similar columns.

The detailed process for the fibre section analysis is given below, and a flow chart of all key processes and inputs is shown in Figure 5.1. The MATLAB scripts for the modified fibre section analysis of all the columns are provided in Appendices D, E, and F.

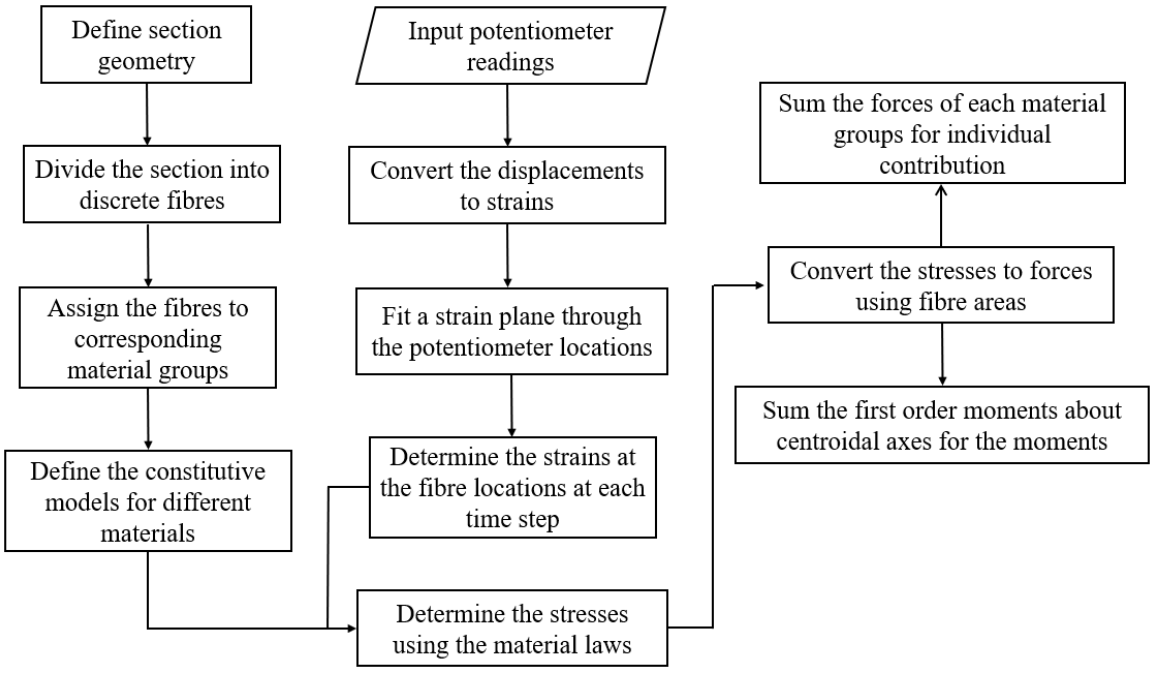


Figure 5.1: Flowchart for the modified fibre section analysis

5.2 Material Constitutive Models

The infill concrete constitutive material models used in the fibre section analysis in this research study were obtained from uniaxial compression tests conducted on cast cylinders in accordance

with ASTM C39/39M. To capture the material behaviour of 3DPC, this research study evaluated three approaches, listed below.

- The first approach measured the stress-strain behaviour of cubes extracted from 3DPC wall specimens when tested in the orientation perpendicular to the interlayer plane, as described in Chapter 3.
- The second approach used the uniaxial stress-strain response of cast cylinders tested in accordance with ASTM C39/39M (i.e., assuming a response similar to that of cast samples).
- The third approach used the load-deformation response of 3DPC cylindrical shell specimens tested in this study (details are in Chapter 3).

The deformation response of the cylindrical shells was measured as overall shortening rather than between two specified points on the specimen, including the Hydrostone applied on top of the cylindrical shell specimens to level the surface for uniform load transfer. As a result, the load–deformation response exhibited an initial nonlinear toe region, attributed to seating effects associated with local accommodation of the hydrostone layer and the establishment of full contact between the specimen and the loading platens. Because the measured displacement included deformation due to the hydrostone caps, the initial portion of the response was not considered representative of the specimen's intrinsic deformation behaviour. To account for this effect, a tangent line was fitted to the approximated linear portion of the load–deformation curve and extrapolated to intersect the x-axis. The intersection point was adopted as the corrected origin. Subsequent fibre section analyses were performed using the corrected load–deformation response. This procedure is depicted in Figure 5.2.

Following the origin correction for the load-deformation responses of the three cylindrical shell specimens, the force was converted to stress by dividing the applied load by the average cross-sectional area measured at multiple locations. The strain was obtained by dividing the change in length by the specimen's overall height. Average stress at each strain level was calculated to obtain

the average stress-strain response of the cylindrical shell specimen, which was then used as input to the material constitutive model for the fibre section analysis.

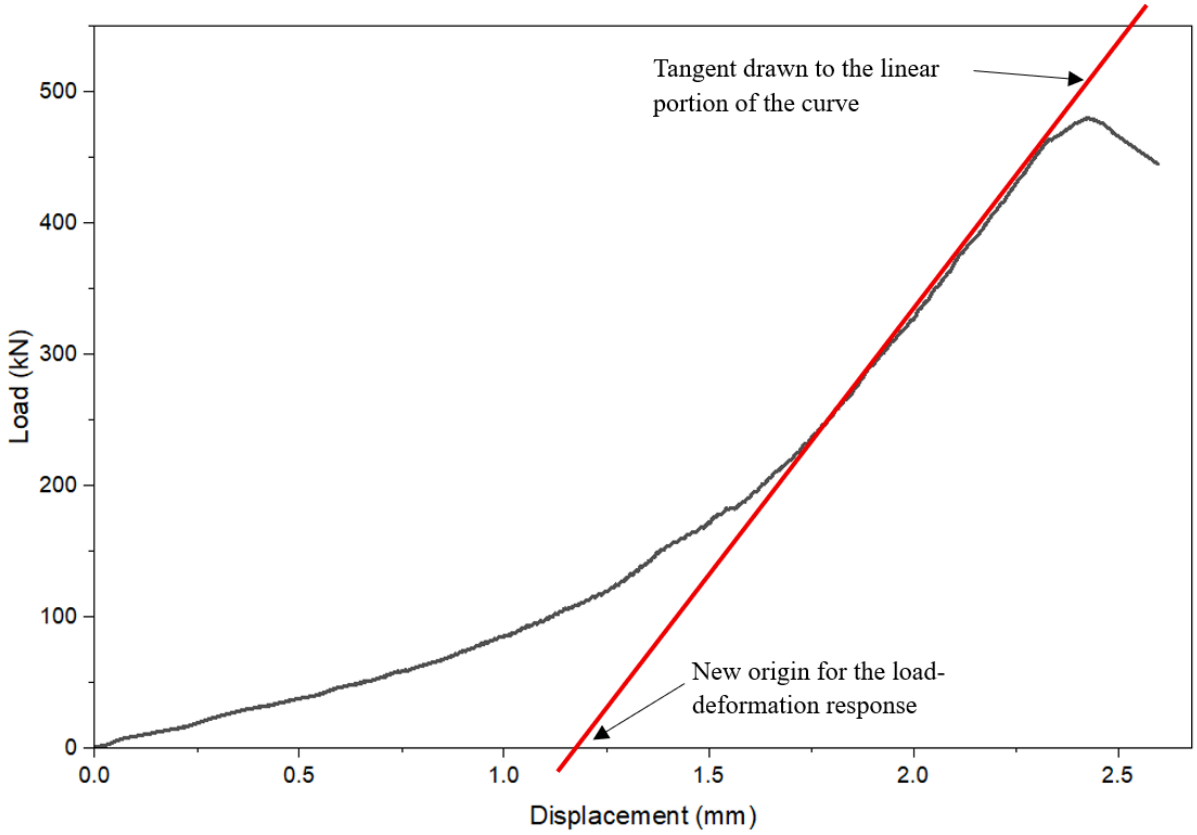


Figure 5.2: Schematic of the correction and new origin definition for the average load-deformation response of 3DPC cylindrical shells using the tangent drawn to the loading part of the

The mechanical properties of the corresponding models used for both 3DPC and infilled concrete are given in Table 5.1. Except for the cylindrical shells, the mechanical properties of the rest of the specimens were determined using ASTM C39/39M (American Society for Testing and Materials, 2024).

Table 5.1: Mechanical properties of specimens used to determine the constitutive model

Material	**Specimen Type**	$f_{c,mean}$	ε_0
Infill concrete (inf)	Cast cylinders	58.66	0.002441
Printed concrete (pc) - approach 1	Cubes	31.14	0.001609
Printed concrete (pc) - approach 2	Cast cylinders	56.25	0.002073
Printed concrete (pc) - approach 3	Cylindrical shells	28.57	0.004492

In the subsequent analysis, tensile stresses are not considered, as the entire section is under compression, and circumferential strains are also not considered. The concrete constitutive models obtained from Approach 1 (cubes), Approach 2 (cast cylinders), and Approach 3 (cylindrical shells) are given in Figure 5.3.

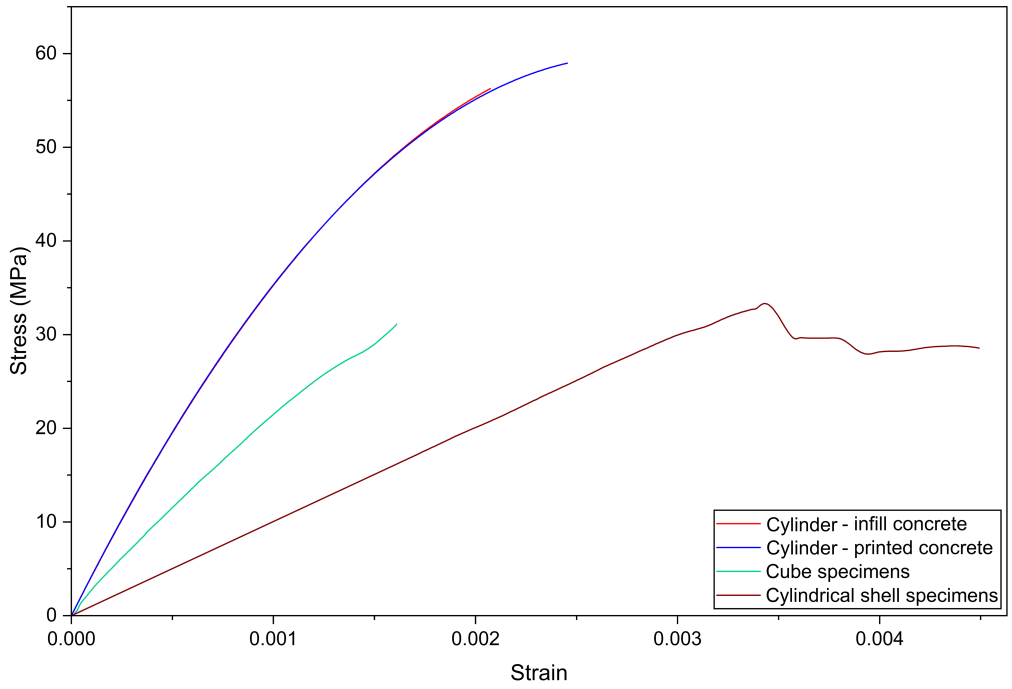


Figure 5.3: Stress-strain response of concrete obtained using shell, cube, and cylinder specimens for both infill and printed concrete

5.2.1 Discretization of cross-section and fibre sectional analysis

The column cross-sections were generated using a custom MATLAB script. The geometry of each specimen, including the outer profile, 3DPC permanent formwork, infill concrete, and the locations of reinforcing steel, was defined directly in the code using hard-coded geometric parameters derived from the experimental specimen dimensions. Regions corresponding to infill concrete, printed concrete, and steel reinforcing bars were assigned groups. The area occupied by steel reinforcing bars was excluded from the concrete region to avoid double-counting of forces. The section was discretised into 10-mm-square elements. A mesh convergence analysis was conducted to obtain

the optimum mesh size that yields the best results. Convergence cannot occur with any mesh size above 350 mm, as the maximum cross-section dimension is 350 mm, while the mesh size must be smaller than 50 mm since the printed layer width is 50 mm. Therefore, only the mesh sizes below 50 mm were checked. Based on the analysis, a 10 mm mesh size yielded reasonable estimates with minimal computational effort and time. The results of the mesh convergence analysis are given in Figure 5.4. The meshed regions of the three sections are shown in Figure 5.5.

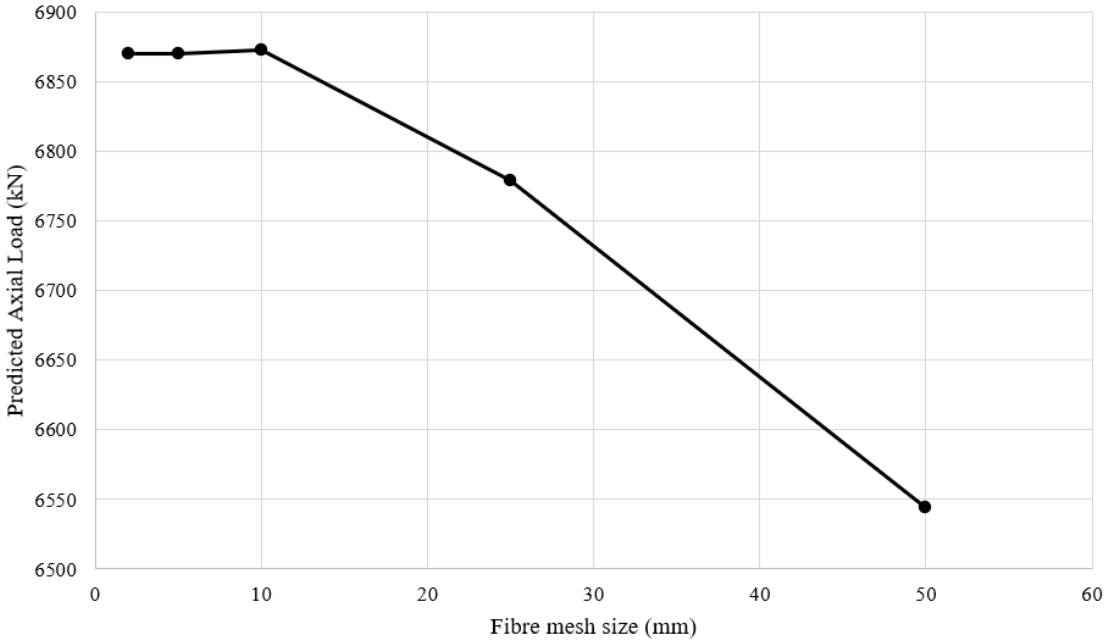
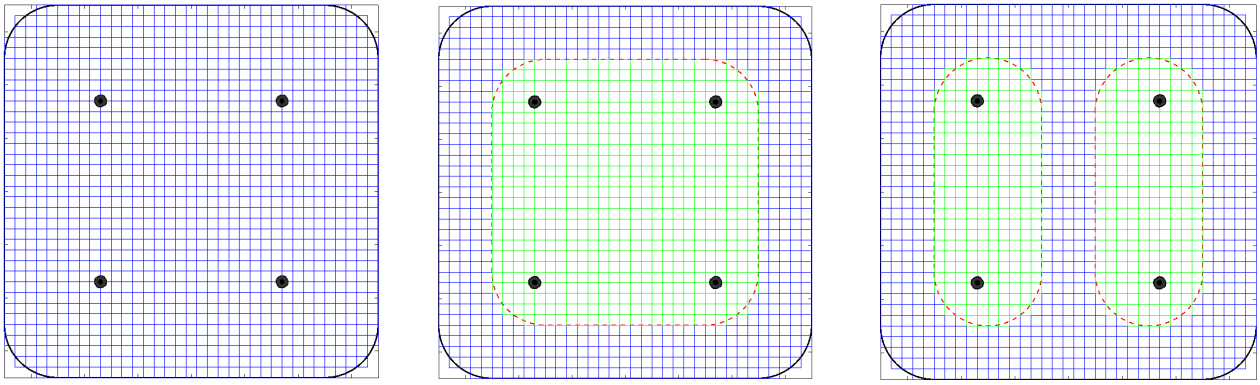


Figure 5.4: Meshconvergence analysis conducted for the fibre section model used in this study



(a) (b) (c)

Figure 5.5: The discretised fibre elements of each cast control specimen, standard permanent formwork concrete column, and optimised permanent formwork concrete column

The three potentiometers attached to the three faces of the columns measured surface strain by

dividing the displacements by the initial gauge lengths. The strain values were then used to fit a plane through the points where the potentiometer readings were taken by solving the following equation, Equation (5.1), for κ_x, κ_y, and ε_0. The locations of the potentiometer and a sample of the fitted plane are shown in Figure 5.6a and Figure 5.6b, respectively.

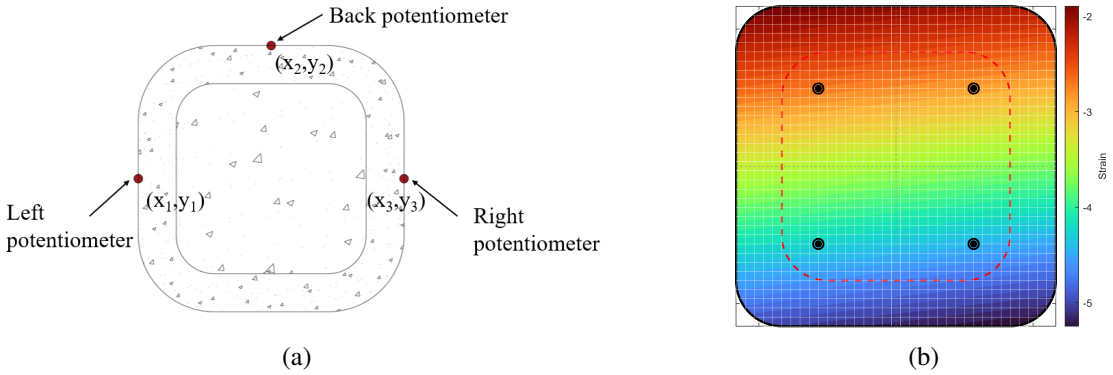
$$\begin{bmatrix} 1 & x_1 & y_1 \\ 1 & x_2 & y_2 \\ 1 & x_3 & y_3 \end{bmatrix} \begin{bmatrix} \varepsilon_0 \\ \kappa_x \\ \kappa_y \end{bmatrix} = \begin{bmatrix} \varepsilon_1 \\ \varepsilon_2 \\ \varepsilon_3 \end{bmatrix} \tag{5.1}$$

Where:

ε_i = axial strain at reference point; $i \in [1,3]$

κ_x, κ_y = coefficients for the plane equation

x_i, y_i = coordinates of the position of the potentiometers; $i \in [1,3]$



(a) (b)

Figure 5.6: (a) the location of the potentiometers and the measured displacements and (b) a sample of the fitted strain plane through the strain values obtained from those potentiometers

The coordinates of the mesh centres (x_i, y_i) were used to interpolate the strain values (ε_i) at those centres using the plane fitted through the displacements measured on the three faces of the columns. The stresses (σ_i) were computed using the corresponding material constitutive models. For the concrete materials, the constitutive relationships were represented by quadratic functions fitted to the average experimental compression stress–strain curves (described as in section 3.4), while the

reinforcing steel was modelled using an elastic-perfectly plastic relationship calibrated from the tensile test results. The stresses were then converted to the force contribution from each element i using Equations (5.2) and (5.3) for both 3DPC and infill concrete, respectively, and the force contributed by the steel was estimated using Equation (5.4).

$$\sigma_{pc} = -7766636.7\varepsilon_{i,pc}^2 + 43091.5\varepsilon_{i,pc} \tag{5.2}$$

$$\sigma_{inf} = -7575125.3\varepsilon_{i,inf}^2 + 42838.9\varepsilon_{i,inf} \tag{5.3}$$

$$\sigma_s = \begin{cases} E_s\varepsilon_i & \varepsilon_i \leq \varepsilon_y, \\ f_y & \varepsilon_i > \varepsilon_y, \end{cases} \tag{5.4}$$

$$\varepsilon_y = \frac{f_y}{E_s} \tag{5.5}$$

Where,

σ_{pc} is the stress in the printed concrete (MPa),

σ_{inf} is the stress in the infill concrete (MPa),

σ_s is the stress in the reinforcing steel (MPa),

E_s is the modulus of elasticity of steel (GPa),

ε_i is the strain in the ith fibre (mm/mm),

$\varepsilon_{i,pc}$ is the strain in the ith fibre of printed concrete (mm/mm),

$\varepsilon_{i,inf}$ is the strain in the ith fibre of infill concrete (mm/mm),

ε_y is the yield strain of steel (mm/mm),

f_y is the yield strength of the reinforcing steel (MPa).

The total force contribution (N) at each time step in the time history was calculated as the sum of

the contributions from 3DPC, infill concrete, and steel, as given in Equation (5.6).

$$N = \sum \sigma_{pc} A_{pc} + \sum \sigma_{inf} A_{inf} + \sum \sigma_s A_s \tag{5.6}$$

One challenge encountered during testing was aligning the columns with the actuator's vertical shaft. Laser levels were used to align the columns; however, due to the vertical profile and geometry of the fabricated columns (particularly the 3DPC columns), the degree of eccentric loading was mitigated as much as possible. However, during testing, the potentiometer readings differed slightly; therefore, the moments induced by the accidental eccentricity needed to be determined. The accidental moments of the x- and y-axes, M_x and M_y, are calculated using Equations (5.7) through (5.10).

$$M_x = \sum F_i y_i \tag{5.7}$$

$$M_x = \sum \sigma_{pc} A_{pc} y + \sum \sigma_{inf} A_{inf} y + \sum \sigma_s A_s y_s \tag{5.8}$$

$$M_y = \sum F_i x_i \tag{5.9}$$

$$M_y = \sum \sigma_{pc} A_{pc} x + \sum \sigma_{inf} A_{inf} x + \sum \sigma_s A_s x_s \tag{5.10}$$

5.3 Modelling Results and Discussion

5.3.1 Estimation of accidental eccentric moments

To quantify the effect of accidental eccentricity on moments, a modified fibre section analysis, as explained above, was conducted. The moments derived from the displacements and loads, as per Equations (5.8) and (5.10), for all columns tested in this study are shown in Figure 5.7. Even with careful alignment of the columns with the actuator shaft's vertical axis, some accidental eccentric moments were created. Comparing the accidental moments, it is evident that all columns expe-

rienced similar axial behaviour regardless of whether they were cast-in-place or 3DPC. Although the moments increased with the applied load, no clear difference was observed between the printed and cast-in-place columns in terms of the potential for accidental moments under uniaxial compression. Meanwhile, the calculated cracking moment (M_{cr}) for CCC was 27 kN-m. Therefore, it was concluded that none of the columns experienced concrete cracking due to bending during the experiment. This induced accidental eccentric moments in the column supports, supporting the use of the proposed modified fibre section analysis, which will eliminate deviations in the results caused by these moments.

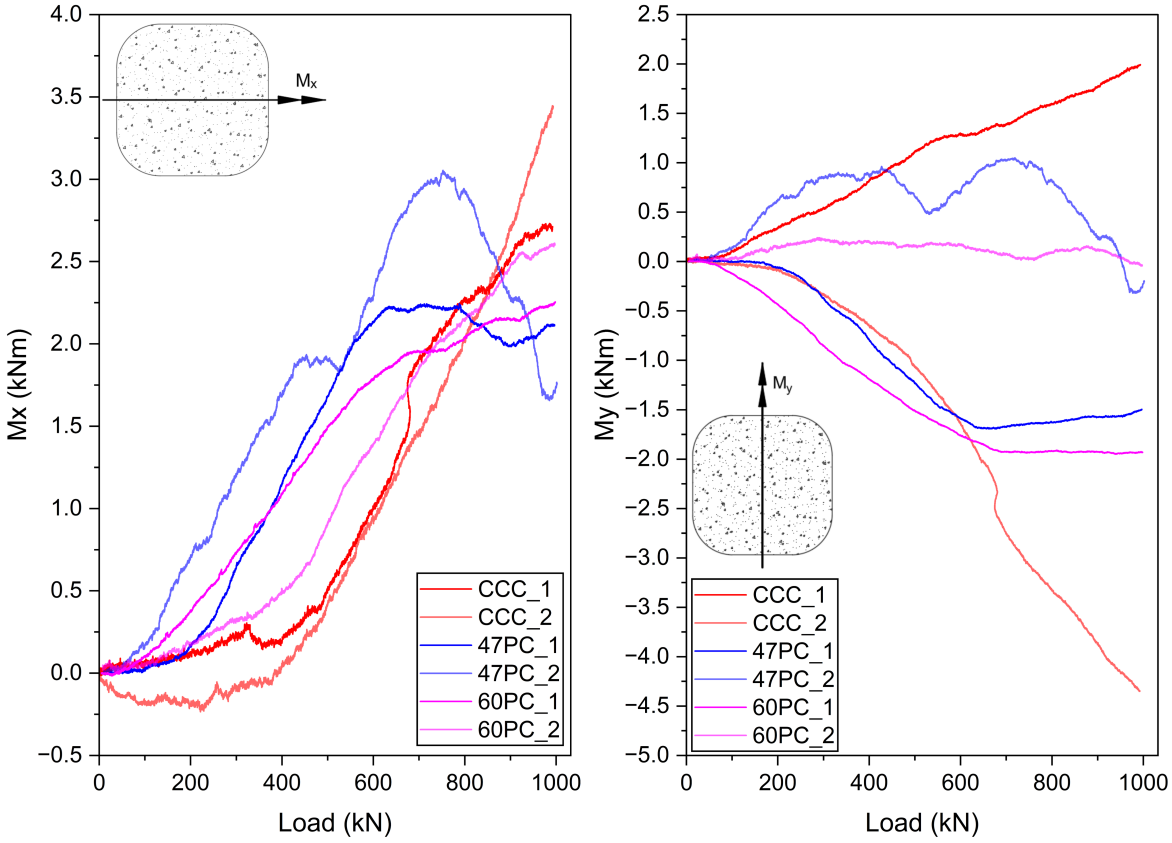


Figure 5.7: Accidental eccentric moments in the x and y directions

5.3.2 Comparison of experimental and predicted axial loads

Three specimens of each type of column, CCC, 47PC, and 60PC, were tested. However, one of each column type was tested multiple times because the initial test results were incomplete due to

improper initial alignment. This would have caused closure of microcracks and changes in the pore structure from the uniaxial compression stress-strain response of cylinders (refer to section 3.4), and Table 5.2 gives the predicted load contribution and the percentage error from the fresh specimens, which were tested only once. Meanwhile, the modified fibre section analysis was used in the subsequent analyses to eliminate possible prediction deviations that could stem from accidental eccentric moments.

The results for the cast concrete column were first used to determine the accuracy of the fibre section analysis. The concrete constitutive model was obtained from the uniaxial compression stress-strain response of cylinders (refer to section 3.4), and Table 5.2 gives the predicted load contribution and the percentage error.

Table 5.2: Predicted and experimental loads with the percentage error for the square cast concrete columns (CCC)

Specimen	**Experimental Load (kN)**	**Predicted Load (kN)**	**Error (%)**
CCC_1	992.10	970.30	-2.1%
CCC_2	993.40	1003.53	1.0%

CCC_3 specimen was tested multiple times, and as a result it was excluded from this analysis

Upon obtaining satisfactory results using the fibre section analysis with a maximum deviation of 2.1% from the experimental values, it was concluded that the material constitutive models chosen for the infilled columns and vertical reinforcing bars provide satisfactory results in comparison to the experimental results. Therefore, subsequent analyses were conducted using these constitutive models for the infilled concrete and reinforcing steel.

As described earlier, the axial force contribution from the printed concrete at each loading step was calculated using three constitutive models derived from uniaxial compression testing of cubes (approach 1), cast cylinders (approach 2), and shell specimens (approach 3). The predicted and experimental loads, along with the error percentages, for the printed columns using the cube stress-strain response as the constitutive model (approach 1) are given in Table 5.3. An error percentage

ranging from 12.6% to 20.3% in the predicted load resistance of the 3DPC columns, compared with the experimental values, suggests that this constitutive model may not provide the most suitable fit for the 3DPC material.

Table 5.3: Predicted and experimental loads with the percentage error of the square columns using the cube stress-strain response (approach 1) as the printed concrete constitutive model

Specimen	**Experimental Load (kN)**	**Predicted Load (kN)**	**Error (%)**
$47PC_1$	996.65	1133.57	13.7%
$47PC_2$	1001.92	1130.24	12.8%
$60PC_1$	998.28	1124.16	12.6%
$60PC_2$	997.34	1199.61	20.3%

$47PC_3$ and $60PC_3$ specimens were tested multiple times, and as a result, they were excluded from this analysis

A similar fibre section analysis was conducted using the stress-strain response obtained from the cylinder specimens (approach 2) to represent the printed concrete. The predicted and experimental loads, along with the percentage error, for the 3DPC columns are given in Table 5.4. The observed error percentages are greater than those observed when cube stress-strain response was used as the constitutive material behaviour for the printed concrete. This observation is supported by reported observations in the literature that mechanical properties obtained from mould-cast specimens often overestimate the actual properties of the printed specimen. Therefore, using the stress-strain response of the mould-cast cylindrical specimens shall be prohibited for the prediction of 3DPC material response.

The same analysis was conducted using the stress-strain behaviour of the cylindrical shell specimens (approach 3) obtained from uniaxial compression loading of the 3DPC shells as the constitutive model for the printed concrete, and the predicted load contribution, along with the experimental values and the error percentage, is given in Table 5.5.

The predicted load contributions from the fibre section analysis, obtained using the shell specimen response as the constitutive model for the printed concrete, yielded the lowest error percentages

Table 5.4: Predicted and experimental loads with the percentage error of the square columns using the cylinder stress-strain response (approach 2) as the printed concrete constitutive model

Specimen	Experimental Load (kN)	Predicted Load (kN)	Error (%)
$47PC_1$	996.65	1538.41	54.3%
$47PC_2$	1001.92	1640.85	63.8%
$60PC_1$	998.28	1625.40	62.8%
$60PC_2$	997.34	1627.90	63.2%

$47PC_3$ and $60PC_3$ specimens were tested multiple times, and as a result, they were excluded from this analysis

Table 5.5: Predicted and experimental loads with the percentage error of the square columns using the shell stress-strain response (approach 3) as the printed concrete constitutive model

Specimen	Experimental Load (kN)	Predicted Load (kN)	Error (%)
$47PC_1$	996.65	1077.73	8.1%
$47PC_2$	1001.92	1075.14	7.3%
$60PC_1$	998.28	985.23	1.3%
$60PC_2$	997.34	1051.34	5.4%

$47PC_3$ and $60PC_3$ specimens were tested multiple times, and as a result, they were excluded from this analysis

relative to the experimental values, ranging from 1.3% to 8.3%. The error in the predicted load contribution for large-scale testing is within the acceptable tolerance for experimental studies of this magnitude (Nguyen-Van et al., 2026). Therefore, the predicted load-deformation behaviours of the columns using the shell constitutive model, along with the experimental load-deformation behaviour for CCC, 47PC and 60PC columns, are given in Figure 5.8, Figure 5.9 and Figure 5.10.

Although the predicted results were within acceptable error limits (10% based on values reported in the literature), with deviations of less than 10% from the experimental values, the error magnitude was not consistent across all specimens. This variation is likely attributable to uncertainties in measuring the locations of the attached potentiometers. Because of the irregular surface texture and curved corners of the printed specimens, accurately determining the potentiometers' coordinates in the horizontal plane was challenging, potentially introducing inaccuracies in strain measurements

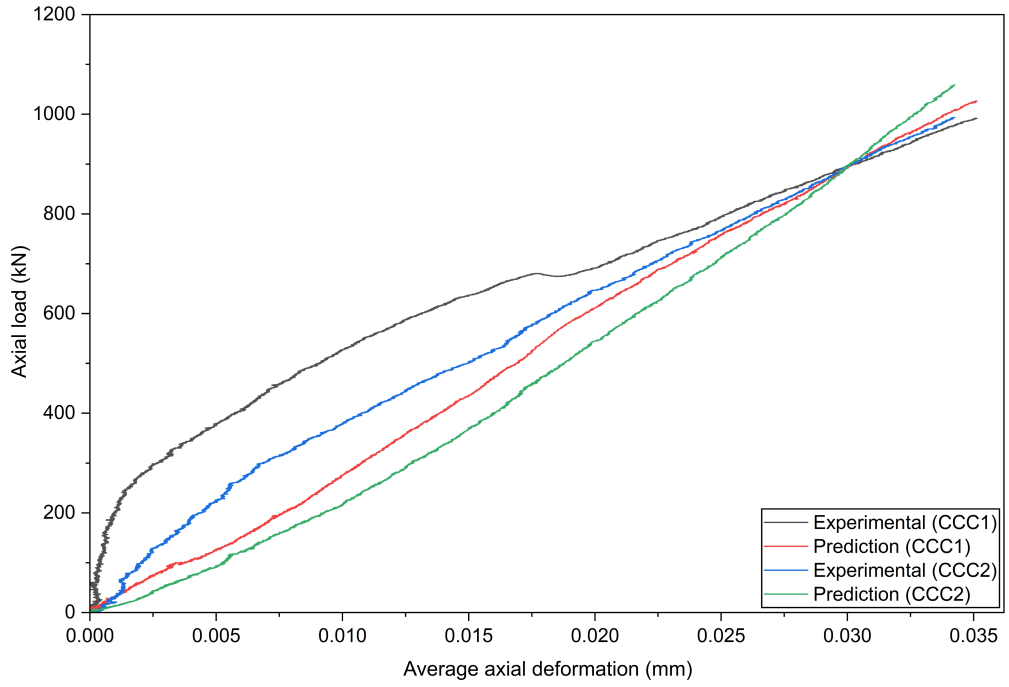


Figure 5.8: Predicted and experimental load-deformation response of cast concrete columns (CCC)

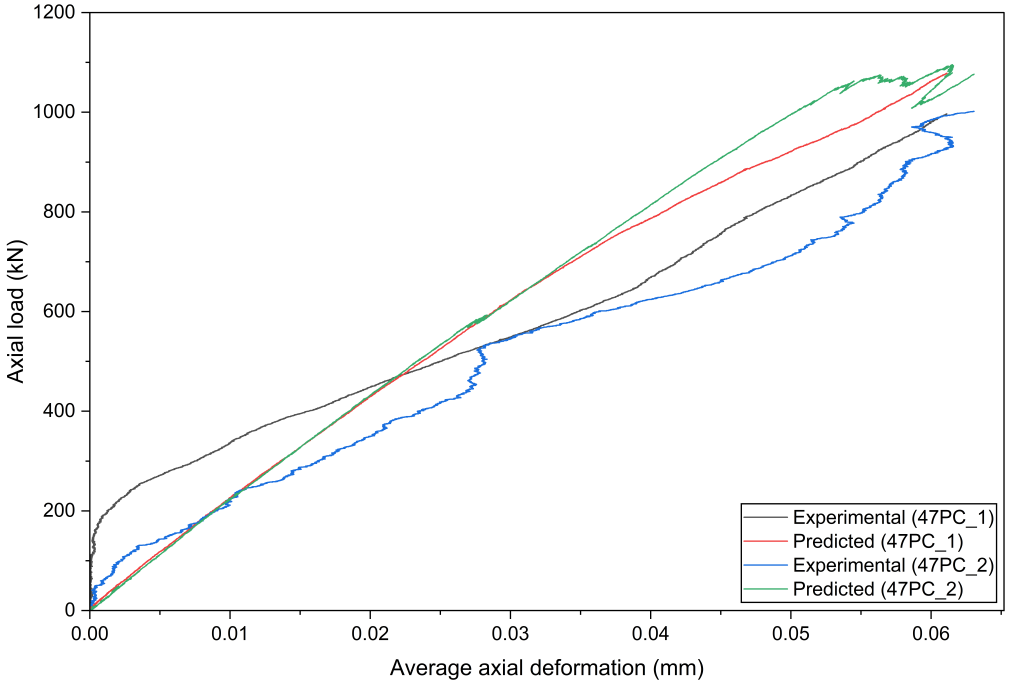


Figure 5.9: Predicted and experimental load-deformation response of standard printed columns (SPC)

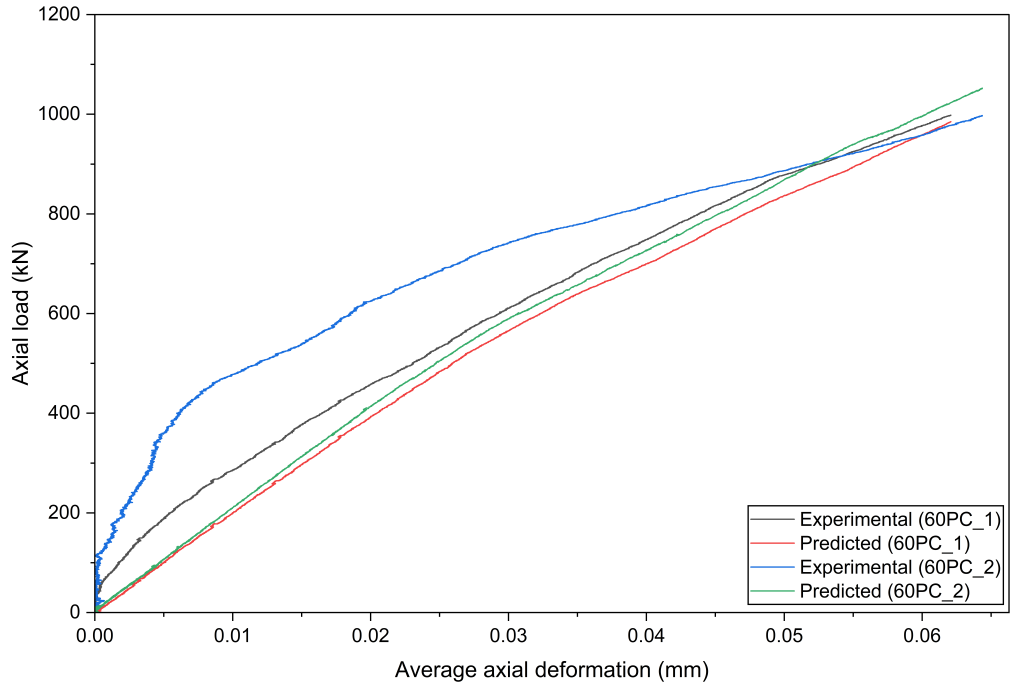


Figure 5.10: Predicted and experimental load-deformation response of optimised printed columns (OPC)

and subsequent predictions. However, for designing columns to resist loads, these models could be used without requiring these considerations.

5.3.3 Estimation of load sharing

The individual contributions of 3DPC, infill concrete, and reinforcement bars were extracted from the fibre section analysis, and the summary results, expressed as percentages of the total at the peak load, are given in Table 5.6. Even though $47PC_3$ and $60PC_3$ were tested multiple times and exhibited greater deformation than the fresh specimens, the percentage load contribution of each material is consistent with that of the untested specimens.

These results are consistent with the hypothesis that load sharing is proportional to the product of the modulus of elasticity (E) and the section area (A) of a material for cast-in-place control specimens, and for the printed concrete columns it is still valid, but the modulus of elasticity corresponding to that of the shell specimens shall be used.

Table 5.6: Percentage load contribution from infill concrete, 3DPC, and reinforcing bars towards the axial contribution obtained from fibre section model

Specimen	3DPC	Infill	Reinforcing Steel
$47PC_1$	17.7%	79.6%	2.7%
$47PC_2$	17.7%	79.6%	2.7%
$47PC_3$*	18.0%	79.2%	2.8%
$60PC_1$	24.5%	72.6%	2.9%
$60PC_2$	24.5%	72.5%	3.0%
$60PC_3$*	27.7%	69.2%	3.0%

* Specimens were tested more than once

5.4 Prediction of the ultimate axial capacity of the columns

Upon verification of the model accuracy using the constitutive models presented in Section 5.3.2, the pure fibre section model (i.e. concentrically loaded fibre section analysis) was used to further extrapolate the ultimate axial capacity of the cast and 3DPC columns based on the following assumptions :

- The plane cross-sections remain plane and no warping of the cross-section at any given point in time;
- The strain at a cross-section is uniform and transferred without any slip between the longitudinal reinforcing bars;
- The 3DPC permanent formwork (veneer) does not delaminate at any load level and contributes towards the axial load carrying capacity of the column; and
- Material constitutive laws are independent of any external or internal forces

The predicted load-deformation response under pure (i.e., concentric) axial deformation of the cast-in-place concrete columns, using the material properties reported in the study, is shown in Figure 5.11, along with the maximum capacity predicted per CSA A23.3-24. The ultimate axial capacity

predicted by the fibre section model was very similar to the CSA prediction (0.34% higher). This difference is due to the square meshes used in a column with curved corners.

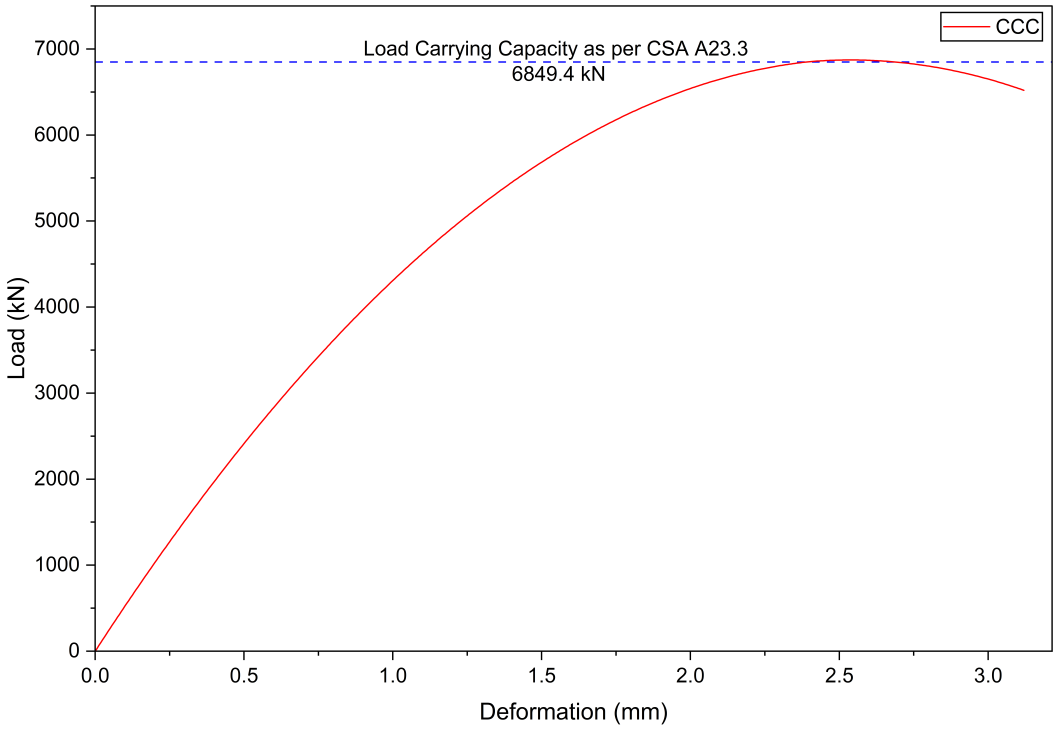


Figure 5.11: Uniaxial compression load-deformation response of cast-in-place (control) column obtained from the fibre section model

The model was further extended to estimate the axial load-carrying capacity of the cast-in-place column, and this estimate was verified against the CSA A23.3-24 provisions without accounting for the 0.85 reduction factor used to relate the cylinder compressive strength to column compressive strength. Upon verifying that the prediction is consistent with the code-based prediction, the model was used to estimate the load-carrying capacity of the printed columns, assuming no delamination of the printed concrete permanent formwork at higher loads and that the printed layer's contribution follows the material constitutive law. This assumption is supported by experimental tests conducted on circular columns up to failure, in which delamination of the printed layer from the infill concrete was not observed. Based on these assumptions, the estimated pure axial load-carrying capacity, without any reduction factors, for 47PC columns is 17.8% less than that of similar cast-

in-place concrete, while the 60PC columns are 22.1% less than the cast-in-place concrete capacity. The predicted axial load-carrying capacities of the cast-in-place and printed columns are shown in Figure 5.12 along with the experimental test results up to 1000 kN. The axial capacities and the reduction in capacity are given in Table 5.7.

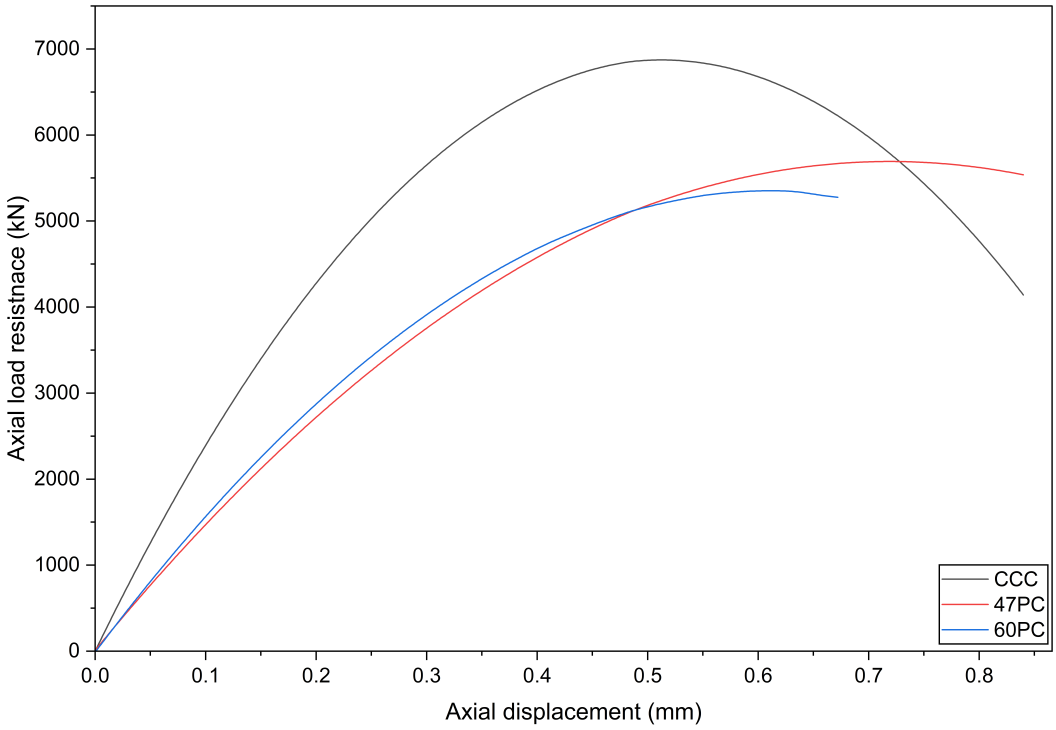


Figure 5.12: Predicted axial load vs displacement of the reinforced concrete columns using the fibre section model for concentric loading case

Table 5.7: Estimated axial load-carrying capacity using the fibre section model

Column Type	**Predicted Axial Resistance**	**Predicted reduction in capacity**
CCC	6873 kN	NIL
47PC	5651 kN	17.8%
60PC	5353 kN	22.1%

The predicted axial load capacities of the 47PC and 60PC columns were 82% and 78% of the predicted axial load capacity of the cast-in-place columns, respectively. These predictions, however,

did not account for accidental eccentricity as the displacements were concentric to the centroidal axis.

5.5 Summary and conclusion

This chapter described the methodology adopted to formulate the modified fibre section analyses used to predict the axial load resistance of the columns tested in this study. The modified fibre section analysis used experimentally measured displacements, which were converted to strain to obtain the strain field across the section and interpolate stresses and forces. This approach eliminates any deviations in the prediction that might arise from accidental eccentricity imparted during testing.

The predicted load resistance of the cast-in-place columns was used to verify the material constitutive models used for the infill concrete and reinforcing steel in the analyses. Three material constitutive models that were obtained from testing of cube samples saw-cut from the printed wall, cylinders moulded using the same concrete mixture proportions, and printed cylindrical shells were used to verify the best-fit constitutive model for the printed concrete permanent formwork. Upon verifying the model results against the experimental results, the constitutive model derived from the cylindrical shell specimens demonstrated the best-fit approximation of the load resistance of the columns, with maximum errors of 8.1% and 5.4% for 47PC and 60PC columns, respectively.

Given the good agreement with the material models used to represent the corresponding constituent materials of the columns, the fibre model was used to extrapolate the axial load-carrying capacity by applying a monotonically increasing concentric displacement along the centroid. The axial load-carrying capacity of the cast-in-place column was compared to the CSA A23.3-24 equation without any reduction factors, producing only 0.34% overestimation of the code equation, which arises from the use of square meshes in the section. The same approach was carried out for the printed columns for the layouts 47PC and 60PC, resulting in $\sim$ 18% and $\sim$ 22% reduction in theoretical axial load-carrying capacity, respectively.

Chapter 6 Conclusions and Future Work

Additive concrete construction, or 3DPC, has become a widely studied research topic in recent years due to rapid technological development and studies supporting the development of a feasible concrete mixture with adequate green properties to support its own weight and improve print quality. Despite numerous studies in this domain, few have explored the potential of 3DPC as a viable solution for fabricating structural elements such as columns, walls, and beams. To the best of the author's knowledge, only a few studies have focused on understanding the structural behaviour of reinforced 3DPC columns. While these studies focused on niche topics such as cyclic behaviour, the incorporation of coarse aggregates, and innovative square precast stirrups for reinforcement cages, one challenge remains unaddressed: establishing guidelines for member sizing to resist axial loads. Therefore, this research aims to provide additional experimental data to address this gap by exploring the uniaxial compression response of reinforced 3DPC columns at service load levels (i.e., up to 17% of nominal axial resistance P_{ro}). In addition, an optimised section geometry for the 3DPC column is proposed that reduces the amount of infill concrete required and increases the amount of printed concrete, thereby saving construction time and allowing alternative concrete mixtures, such as low-carbon concrete, to be used in smaller quantities as infill material.

6.1 3DPC Material Behaviour

To understand the composite behaviour of the 3DPC columns, material properties such as compressive strength and elastic modulus were determined. The literature indicates that using cast concrete specimens often overestimates the mechanical properties of 3DPC, and little research has reported measuring the elastic modulus. Therefore, a separate study was conducted to propose two specimen geometries (cubes and prisms) for determining the elastic modulus of 3DPC. The modulus of elasticity results obtained from these two different specimens were then compared with the derived axial stiffness measured by testing 3DPC hollow cylindrical shell specimens. It was found that the axial stiffness derived from the moduli of elasticity of the cubes and prisms did not

provide comparable axial stiffness estimates of the concrete shells. This is attributed to differences in the combined behaviour of the interlayering in the 3DPC and the bulk material, and also to variations in the overall response as the number of interfaces captured in the tested structure varies. However, the proposed specimens provided consistent results over the tested specimens in the two directions evaluated, perpendicular and parallel to the interlayer of the printed layers, implying that these specimens could be used to determine the elastic modulus for the purposes of material characterisation. The compressive strength of the prism specimens was 21% lower than that of the cube specimens, while the modulus of elasticity varies by only 3%. This indicated that the prisms failed under buckling at higher loads while exhibiting similar behaviour to cubes at lower load levels. Therefore, using cubes as representative specimens for mechanical characterisation is recommended rather than prisms. However, when using small specimens such as cubes or prisms to approximate the mechanical properties of 3DPC structures, appropriate modification factors should be considered.

One commonly reported behaviour of 3DPC material is the anisotropy arising from interactions between printed layers. This study sought to verify this phenomenon by testing the cubes in different directions under compression loading. Since the cubes were already sawcut and the layer width is 50 mm, the imperfections on the printed layer surface were not removed. As a result, only two sides were tested to prevent any further disturbance to the samples. The compressive strength results for the two tested directions were statistically verified for normality at the 95% confidence level. A two-sample t-test with equal variances was conducted to test whether the sample means differ significantly. At the 95% confidence level, the results indicate that the two samples did not differ, suggesting isotropic behaviour in the two tested directions. This conclusion is supported by recent studies on the isotropic behaviour of 3DPC materials printed using the 1K and 2K systems, as well as studies of pore structures and mechanical testing, which show that the 2K system often exhibits isotropic behaviour. The printer used in this research study is a 2K COBOD BOD2 system; therefore, this observation is consistent with other studies that used a similar printer.

6.2 Behaviour of 3D printed concrete cylindrical shell

Phase 2 of this research study compared the axial stiffness of 3D-printed hollow cylindrical shells with the axial stiffness determined using the modulus of elasticity obtained from the cube and prism specimens proposed in Phase 1 as representative samples for determining the mechanical properties of 3DPC. The axial stiffness of the hollow 3DPC circular cylindrical shells was found to be nearly 80% lower than the modulus of elasticity measured using cubes or prism specimens. Part of this error could be due to geometric simplifications in printing the cylindrical shells to form a uniform shell with average geometric dimensions throughout the height and across the cross section.

The load-deformation behaviour recorded for the uniaxial compression test of the hollow cylindrical shells was measured as the total shortening of the specimens. This included an ascending region in the response plot, which contradicts typical descending or stiffness-degradation models for similar structures. Therefore, a correction was applied to obtain the probable load-deformation behaviour of the 3D-printed cylindrical shells, which was later used to derive constitutive relationships for 3DPC for use in fibre section analysis.

6.3 Reinforced 3D printed concrete columns

Nine square reinforced concrete columns (350 mm x 350 mm x 1200 mm)and nine (9) circular (250 mm diameter x 340 mm) reinforced concrete columns were tested in axial compression. The purpose of this part of the research was to quantify differences in the axial response of 3DPC columns and similar cast-in-place columns fabricated using the same concrete mixture. Due to test setup limitations and 3D printer constraints, the large-scale square columns were tested only to 1000 kN, while the circular columns were tested to failure.

The square columns were instrumented with DFOS to measure strain along the length of two vertical reinforcing bars and the stirrup at mid-height; in addition, the 3DPC columns also contained DFOS between printed layers at mid-height of the column. To quantify the accidental eccentric-

ity introduced during experimental testing and the load contribution from different materials (i.e., 3DPC, infill, and reinforcing steel), a fibre section analysis was selected as the main analysis tool. The geometry was discretised into 10 mm square elements and assigned material properties depending on their location within the cross-section (i.e., 3DPC, infill concrete, or reinforcing steel). To establish constitutive relationships, a tension test was conducted on reinforcing bars from the same batch used to fabricate the columns, and a compression test capturing the full stress-strain response was performed on three different specimen types. Three material constitutive models were therefore obtained based on compression testing of cylinders, saw-cut cubes (50 mm), and 3DPC hollow cylindrical shells. The fibre section analysis of the cast control columns was used to verify the accuracy of the method and the material constitutive models for the infill concrete and vertical reinforcing bars.

The comparison between the experimental and predicted axial load contributions yielded a maximum error of 2.1%. Therefore, the fibre section analysis was deemed sufficiently accurate for predicting the load contributions from the infill concrete and reinforcing bars. Following this analysis, three different fibre section analysis models for the 3DPC columns were analysed (i.e., using the three constitutive models). Using cast cylinder stress-strain behaviour as the infill concrete material constitutive model resulted in the largest error, overpredicting the load contribution by 63.8%, whereas using cube stress-strain behaviour as the constitutive model overpredicted the load contribution by 24.6%. These results are consistent with the literature findings that the mechanical properties obtained from cylinders often overestimate actual values because cylinders fail to capture the effects of interlayer presence and are compacted during casting, whereas 3D-printed concrete has no physical compaction. Therefore, this research compared a third constitutive-model approach that uses the stress-strain behaviour of 3DPC cylindrical shells under uniaxial loading. This approach yielded a maximum error of 8.1% for 47PC columns and 5.4% for 60PC columns, which was by far the best approximation of the predicted load resistance compared to the experimental results.

On the other hand, even though the cast specimens were saw-cut from a printed structure, they captured only one interlayer surface across the specimen's full height. Studies on the pore structure of printed structures have found that the pore density at the interface differs from that in the bulk material. Therefore, using cube specimens as representative samples for large, printed structures may not yield accurate predictions. Therefore, this research compared a third constitutive-model approach that uses the stress-strain behaviour of 3DPC cylindrical shells under uniaxial loading. This approach yielded a maximum error of 8.1%, the best approximation of the load contribution of the 3DPC columns. Further prediction of the load contribution of the optimised column proposed in this study confirms the model's accuracy.

The fibre section analysis, verified by experimental results, could be used for parametric studies by varying the percentage of vertical reinforcement in the section and for alternative section geometries. However, this fibre section analysis did not account for the effect of concrete confinement due to lateral reinforcement, as the literature indicates that the confinement effect is pronounced at failure, increases ductility, and is minimal in the early stages of loading. The applied load is 1000 kN and is within 17% of the columns' nominal axial resistance, P_{ro}, as per CSA A23.3-24, assuming pure concentric loading, without any material safety factors, and neglecting the effects of confinement.

Using the proposed fibre section model, the load sharing between the constituent materials of the printed columns was determined. For 47PC columns, the 3DPC was estimated to share 17.7% of the axial load, while the infill concrete and the remaining 2.7% were shared by the vertical reinforcing bars, which shared 79.6%. For 60PC columns, 24.5% of the axial load is resisted by the 3DPC, while 72.5% is resisted by the infilled concrete and the remaining 3% by the vertical reinforcing bars. This finding suggests that reinforced infilled columns with 3DPC permanent formwork should be designed to account for the load resistance provided by the 3DPC permanent formwork.

6.4 Future Directions

Studies should focus on understanding the overall behaviour of printed concrete by examining the bulk material and the interface region separately. Further, studies should examine whether the behaviour of printed structures correlates with the number of layers included. If a correlation is present, studies should focus on relationships to predict behaviour using the proposed specimens that capture the intrinsic properties of 3DPC. Moreover, the high standard deviation and coefficient of variation observed across the tests conducted to determine the mechanical properties underscore the uncertainty prevailing around the determination of the mechanical properties of 3DPC. Therefore, it is recommended to test more than three samples to obtain the mechanical properties.

Given the results of the fibre section analysis produced using the cube stress-strain behaviour as the constitutive model for the printed column, which provided a maximum deviation of 20.3% from the experimentally measured axial load resistance and the predictions provided by the printed cylindrical shells, which had a maximum deviation of 8.1%. These results support the use of a 3DPC cylindrical shell stress-strain model as a material constitutive model for 3DPC instead of sawcut specimens. However, if a correlation exists between the number of printed layers and the mechanical properties derived from a sawcut cube, as presented in this study, the constitutive model obtained using sawcut cubes could represent 3DPC in similar analyses with corresponding adjustment factors.

This research proposed a fibre section model to predict the axial load resistance of the printed columns, with the corresponding constitutive models providing sufficient accuracy relative to the experimentally measured load resistance. However, due to the limitations of the hydraulic actuator setup, the columns could be tested up to 1000 kN, while the constraints of the printing system restrict any columns from being made smaller than those used in this study, using the optimised 60PC layout. However, smaller-dimension columns could be made using the 47PC layout. The model is verified up to 1000 kN, and the author recommends conducting experimental studies

using similar layouts and testing to failure to validate the fibre section model. Upon verification, the model shall be used at its full capacity to determine the nominal axial load resistance of the columns and to develop moment interaction diagrams, which can later be used in structural design applications using 3DPC as permanent formwork for reinforced concrete columns.

References

Abdullah, Leung, A. Y., and Chan, T. M. (2025). Characterisation of strain distribution in concrete-filled steel tubular columns via distributed fibre optic sensing technology. *Structures*, 81.

Ahmed, G. H. (2023). A review of "3d concrete printing": Materials and process characterization, economic considerations and environmental sustainability. *Journal of Building Engineering*, 66:105863.

Akomah, B. B., Ahinaquah, L. K., and Mustapha, Z. (2020). Skilled labour shortage in the building construction industry within the central region. *Baltic journal of real estate economics and construction management*, 8:83–92.

Alsharef, A., Ovid, A., Uddin, S. M. J., and Albert, A. (2024). Biggest challenges facing the construction industry. In *Construction Research Congress 2024*, pages 652–660.

American Society for Testing and Materials (2022). Astm c469/c469m-22: Standard test method for static modulus of elasticity and poisson's ratio of concrete in compression. Standard Test Method ASTM C469/C469M-22, ASTM International.

American Society for Testing and Materials (2024). Astm c39/c39m-24: Standard test method for compressive strength of cylindrical concrete specimens. Standard Test Method ASTM C39/C39M-24, ASTM International.

Bai, H., Guo, D., Wang, W., Tan, X., Yan, M., Chen, G., and Bao, Y. (2022). Experimental investigation on flexural behavior of steel-concrete composite floor slabs with distributed fiber optic sensors. *Journal of Building Engineering*, 54.

Bates, R. and Aslani, F. (2025). Performance of 3d-printed concrete columns with gfrp rebars under axial compression. *Scientific Reports*, 15(1):39419.

Baz, B., Aouad, G., Khalil, N., and Remond, S. (2021). Inter-layer reinforcement of 3d printed concrete elements. *Asian Journal of Civil Engineering*, 22:341–349.

Baz, B., Aouad, G., and Remond, S. (2020). Effect of the printing method and mortar's workability on pull-out strength of 3d printed elements. *Construction and Building Materials*, 230.

Bolomope, M. T., Nwadike, A. N., and Aigwi, I. E. (2025). Managing supply chain disruptions in the construction industry: an institutional approach. *Journal of Financial Management of Property and Construction*, 30:212–231.

Bos, F., Wolfs, R., Ahmed, Z., and Salet, T. (2016). Additive manufacturing of concrete in construction: potentials and challenges of 3d concrete printing. *Virtual and physical prototyping*, 11:209–225.

Bos, F. P., Ahmed, Z. Y., Jutinov, E. R., and Salet, T. A. M. (2017). Experimental exploration of metal cable as reinforcement in 3d printed concrete. *Materials*, 10.

Braga, F., Gigliotti, R., and Laterza, M. (2006). Analytical stress–strain relationship for concrete confined by steel stirrups and/or frp jackets. *Journal of Structural Engineering*, 132(9):1402–1416.

Canadian Standards Association (2024). *CSA A23.3-24: Design of Concrete Structures*. Canadian Standards Association, Mississauga, ON, Canada.

Chen, Y., Zhang, W., Zhang, Y., Zhang, Y., Liu, C., Wang, D., Liu, Z., Liu, G., Pang, B., and Yang, L. (2023). 3d printed concrete with coarse aggregates: Built–in–stirrup permanent concrete formwork for reinforced columns. *Journal of Building Engineering*, 70:106362.

Colyn, M., Van Zijl, G., and Babafemi, A. J. (2024). Fresh and strength properties of 3d printable concrete mixtures utilising a high volume of sustainable alternative binders. *Construction and Building Materials*, 419:135474.

Cooperman, A. and Martinez, M. (2015). Load monitoring for active control of wind turbines. *Renewable and Sustainable Energy Reviews*, 41:189–201.

Dahlenburg, M., Hechtl, C. M., Matthäus, C., and Fottner, J. (2022). 3d-concrete printing–graded concrete extrusion. In *2022 3rd International Conference on Computation, Automation and Knowledge Management (ICCAKM)*, pages 1–5. IEEE.

Delavar, M. A., Chen, H., and Sideris, P. (2024). Analysis and design of 3d printed reinforced concrete walls under in-plane quasi-static loading. *Engineering Structures*, 303:117535.

Deloitte (2025). Deloitte's global powers of construction report finds that the rebounding construction industry expects significant growth through 2030. `https://www.deloitte.com/global/en/about/press-room/deloitte-global-powers-of-construction-report.html`. Accessed: 2026-04-30.

Du, L., Zhou, J., Lai, J., Wu, K., Yin, X., and He, Y. (2023). Effect of pore structure on durability and mechanical performance of 3d printed concrete. *Construction and Building Materials*, 400.

Farra, R., Mazanec, O., Ducoulombier, N., and Mallet, A. (2024). Toward the optimal use of local cementitious materials through novel admixture technology and a dedicated 2k printing system. *Digital Concrete*.

Floris, I., Adam, J. M., Calderón, P. A., and Sales, S. (2021). Fiber optic shape sensors: A comprehensive review. *Optics and Lasers in Engineering*, 139:106508.

Gu, Y.-c. and Khayat, K. H. (2024). Extrudability window and offline test methods to predict buildability of 3d printing concrete. *Cement and Concrete Research*, 182:107552.

Hager, I., Golonka, A., and Putanowicz, R. (2016). 3d printing of buildings and building components as the future of sustainable construction? In *Procedia Engineering*, volume 151, pages 292–299. Elsevier Ltd.

Hao, X. (2020). *Mechanical simulation of the passive confinement of reinforced concrete for design*. PhD thesis, School of Architecture and Civil Engineering, Univ. of Adelaide.

Hassan, G. M. (2021). Deformation measurement in the presence of discontinuities with digital image correlation: A review. *Optics and Lasers in Engineering*, 137:106394.

Hognestad, E. (1951). Study of combined bending and axial load in reinforced concrete members. *University of Illinois. Engineering Experiment Station. Bulletin; no. 399*.

Huang, Y., Xu, M., Cui, Z., and Zhao, H. (2026). Experimental study on mechanical properties and anisotropic degradation mechanism of 3dpc after exposure to high temperature. *Construction and Building Materials*, 527.

Hwang, D. and Khoshnevis, B. (2005). An innovative construction process-contour crafting (cc). In *Proceedings of the 22nd International Symposium on Automation and Robotics in Construction*.

International Code Council (2025). Icc 1150: Standard for 3d automated construction technology for 3d concrete walls. Draft Standard ICC 1150, International Code Council.

International Organization for Standardization and ASTM International (2023). Additive manufacturing for construction — Qualification principles — Structural and infrastructure elements.

Ji, G., Ding, T., Xiao, J., Du, S., Li, J., and Duan, Z. (2019). A 3d printed ready-mixed concrete power distribution substation: Materials and construction technology. *Materials*, 12:1540.

Khoshnevis, B. (2004). Automated construction by contour crafting - related robotics and information technologies. In *Automation in Construction*, volume 13, pages 5–19.

Lee, H., Kim, J.-H. J., Moon, J.-H., Kim, W.-W., and Seo, E.-A. (2019). Evaluation of the mechanical properties of a 3d-printed mortar. *Materials*, 12:4104.

Li, Z., Wang, L., Ma, G., Sanjayan, J., and Feng, D. (2020). Strength and ductility enhancement of 3d printing structure reinforced by embedding continuous micro-cables. *Construction and Building Materials*, 264:120196.

Lin, H.-J. and Liao, C.-I. (2004). Compressive strength of reinforced concrete column confined by composite material. *Composite Structures*, 65(2):239–250.

Liu, J. et al. (2025). Comprehensive review of 3d printed concrete, life cycle assessment, ai and ml models: Materials, engineered properties and techniques for additive manufacturing. *Construction and Building Materials*, 415:134234.

Liu, J., Kanwal, H., Tang, C., and Hao, W. (2022). Study on flexural properties of 3d printed lattice-reinforced concrete structures using acoustic emission and digital image correlation. *Construction and Building Materials*, 333.

Ma, G., Li, Z., Wang, L., and Bai, G. (2019). Micro-cable reinforced geopolymer composite for extrusion-based 3d printing. *Materials Letters*, 235:144–147.

Mander, J. B., Priestley, M. J. N., and Park, R. (1988). Theoretical stress-strain model for confined concrete. Technical report.

Marchment, T. and Sanjayan, J. (2019). Mechanical anisotropy of 3d printed fibre reinforced concrete. *Materials and Design*, 181:108088.

Marchment, T. and Sanjayan, J. (2020). Bond properties of reinforcing bar penetrations in 3d concrete printing. *Automation in Construction*, 120.

Marini, A., Spacone, E., et al. (2006). Analysis of reinforced concrete elements including shear effects. *ACI Structural Journal*, 103:645–655.

Menon, M. A. and Varghese, S. (2018). Labour productivity measurement method using 3d bim of a commercial project. *Labour*, 5.

Mim, N. J., Shaikh, F. U. A., and Sarker, P. K. (2025). Sustainable 3d printed concrete incorporating alternative fine aggregates: A review. *Case Studies in Construction Materials*, page e04570.

Natanzi, A. S. and McNally, C. (2023). Experimental investigation of low carbon 3d printed concrete. *Transportation Research Procedia*, 72:3696–3702.

Nguyen-Van, V., Jie, C. C., Zhang, Y. X., and Wong, H. S. (2026). Effect of infill architecture on structural performance and sustainability of 3d-printed reinforced concrete columns. *Engineering Structures*, 351:122057.

Nodehi, M., Aguayo, F., Nodehi, S. E., Gholampour, A., Ozbakkaloglu, T., and Gencel, O. (2022). Durability properties of 3d printed concrete (3dpc). *Automation in Construction*, 142:104479.

Odoko, A., Ealefoh, D., Haruna, S., and Okechukwu, O. (2018). The role the construction industry plays in economic growth. *Journal of Environmental Science and Resources Management*, 10(2):92–98.

Palmieri, L., Schenato, L., Santagiustina, M., and Galtarossa, A. (2022). Rayleigh-based distributed optical fiber sensing. *Sensors*, 22(18):6811.

Pan, Z., Si, D., Tao, J., and Xiao, J. (2023). Compressive behavior of 3d printed concrete with different printing paths and concrete ages. *Case Studies in Construction Materials*, 18.

Panda, B., Mohamed, N. A. N., Paul, S. C., Singh, G. V. P. B., Tan, M. J., and vSavija, B. (2019). The effect of material fresh properties and process parameters on buildability and interlayer adhesion of 3d printed concrete. *Materials*, 12:2149.

Panda, B., Paul, S. C., Mohamed, N. A. N., Tay, Y. W. D., and Tan, M. J. (2018). Measurement of tensile bond strength of 3d printed geopolymer mortar. *Measurement*, 113:108–116.

Panda, B., Paul, S. C., and Tan, M. J. (2017). Anisotropic mechanical performance of 3d printed fiber reinforced sustainable construction material. *Materials Letters*, 209:146–149.

Pegna, J. (1997). Exploratory investigation of solid freeform construction. *Automation in Construction*, 5:427–437.

Perkins, I. and Skitmore, M. (2023). Digital fabrication with concrete: A state-of-the-art review. *Automation in Construction*, 147:104717.

Perng, Y.-H., Chen, S.-J., and Lu, H.-J. (2005). Potential benefits for collaborating formwork subcontractors based on co-operative game theory. *Building and Environment*, 40:239–244.

Phadnis, K. P., Shariff, M. N., and Menon, D. (2020). Optimal rate of printing of 3d printed concrete columns and walls to avoid buckling. In *IOP Conference Series: Materials Science and Engineering*, volume 936. IOP Publishing Ltd.

Pham, L., Tran, P., and Sanjayan, J. (2020). Steel fibres reinforced 3d printed concrete: Influence of fibre sizes on mechanical performance. *Construction and Building Materials*, 250:118785.

Quah, T. K. N., Tay, Y. W. D., Lim, J. H., Tan, M. J., Wong, T. N., and Li, K. H. H. (2023). Concrete 3d printing: Process parameters for process control, monitoring and diagnosis in automation and construction. *Mathematics*, 11:1499.

Raza, S., Triantafyllidis, Z., Anton, A., Dillenburger, B., and Shahverdi, M. (2024). Seismic performance of fe-sma prestressed segmental bridge columns with 3d printed permanent concrete formwork. *Engineering Structures*, 302:117423.

Saelens, L., Wan-Wendner, R., Caspeele, R., and Tittelboom, K. V. (2026). Anisotropy of 3d printed concrete strength and elasticity for a well-developed one-component and two-component concrete mixture. *Cement and Concrete Composites*, 170:106544.

Sahin, H. G. and Mardani, A. (2023). Mechanical properties, durability performance and interlayer adhesion of 3dpc mixtures: a state-of-the-art review. *Structural concrete*, 24:5481–5505.

Shanmugam, N. E. and Lakshmi, B. (2001). State of the art report on steel–concrete composite columns. *Journal of constructional steel research*, 57(10):1041–1080.

Silfwerbrand, J. (2024a). Composite concrete columns of 3dp concrete and self-compacting concrete subjected to normal force. *Proceedings, Digital Concrete*, pages 4–6.

Silfwerbrand, J. (2024b). Form pressure in composite columns of 3dpc and scc. *Nordic Concrete Research*, 71:137–151.

Silveira, M. V. G., Wagner, J. S., Khanverdi, M., and Das, S. (2024). Structural performance of large-scale 3d-printed walls subjected to axial compression load. *Canadian Journal of Civil Engineering*, 51:919–933.

Singh, A., Wang, Y., Zhou, Y., Sun, J., Xu, X., Li, Y., Liu, Z., Chen, J., and Wang, X. (2023). Utilization of antimony tailings in fiber-reinforced 3d printed concrete: A sustainable approach for construction materials. *Construction and Building Materials*, 408.

Sousa Jr, J. B. M. and Muniz, C. F. (2007). Analytical integration of cross section properties for numerical analysis of reinforced concrete, steel and composite frames. *Engineering Structures*, 29(4):618–625.

Subakaran, R. and Butler, J. L. (2026). Experimental characterization of the modulus of elasticity of 3d-printed concrete utilizing full-scale printing parameters. In *Proceedings of the CSCE Annual Conference*, Quebec, Canada.

Suhr, J. K. (2009). Kanade-lucas-tomasi (klt) feature tracker. *Computer Vision (EEE6503)*, pages 9–18.

Taborda-Llano, I., Hoyos-Montilla, A. A., Asensio, E., Guerrero, A. M., and Tobón, J. I. (2025). Influence of the construction process parameters on the mechanical performance and durability of 3d printed concrete (3dpc): A systematic review. *Journal of Building Engineering*, page 114965.

Tang, F., Zhou, G., Li, H. N., and Verstrynge, E. (2021). A review on fiber optic sensors for rebar corrosion monitoring in rc structures. *Construction and Building Materials*, 313.

Taucer, F., Spacone, E., and Filippou, F. C. (1991). *A fiber beam-column element for seismic response analysis of reinforced concrete structures*, volume 91. Earthquake Engineering Research Center, College of Engineering, University of California.

The MathWorks, Inc. (2024). *MATLAB*. The MathWorks, Inc., Natick, Massachusetts, United States. Version R2024b.

Tomasi, C. and Kanade, T. (1991). Detection and tracking of point. *Int J Comput Vis*, 9(137-154):3.

UL LLC (2022). Ul 3401: Outline of investigation for 3d printed building construction. (UL 3401).

Venkateshwaran, A., Lai, B. L., and Liew, J. Y. (2022). Buckling resistance of steel fibre-reinforced concrete encased steel composite columns. *Journal of Constructional Steel Research*, 190.

Wang, C., Chen, B., Vo, T. L., and Rezania, M. (2023). Mechanical anisotropy, rheology and carbon footprint of 3d printable concrete: A review. *Journal of Building Engineering*, 76:107309.

Wang, H., Shen, J., Sun, X., Dong, W., and Gao, J. (2025). Numerical investigation on shear behaviour of reinforced concrete beam with 3d printed concrete permanent formwork. *Journal of Building Engineering*, 100:111706.

Wang, Q., Yang, W., Wang, L., Zhang, D., Li, Z., and Ma, G. (2024). Flexural performance of the integrated steel truss reinforced 3d printed concrete beams: experimental and numerical analysis. *Journal of Building Engineering*, 97:110794.

Wolfs, R. J. M., Bos, F. P., and Salet, T. A. M. (2018). Structural failure behaviour of 3d printed concrete walls. *Structural and Multidisciplinary Optimization*, 57:1387–1402.

Xie, S., Liu, Y., Ansari, F., and Bao, Y. (2026). Distributed fiber optic sensors for monitoring cracks in civil infrastructure. *Automation in Construction*, 182.

Yerikania, U., Du, H., and Poh, L. H. (2025). A comprehensive experimental investigation of anisotropy behavior on highly carbon-minimized 3d printed concrete (3dpc). *Construction and Building Materials*, 491:142766.

Zhang, D., Ma, G., Guan, J., Wang, L., and Wang, Q. (2023). Cyclic behavior of unbonded post-tensioned precast segmental concrete columns fabricated by 3d printed concrete permanent formwork. *Engineering Structures*, 292.

Zhang, J., Wang, J., Dong, S., Yu, X., and Han, B. (2019). A review of the current progress and application of 3d printed concrete.

Zhang, K., Lin, W., Zhang, Q., Wang, D., and Luo, S. (2024). Evaluation of anisotropy and statistical parameters of compressive strength for 3d printed concrete. *Construction and Building Materials*, 440:137417.

Zhang, S., Liu, H., Coulibaly, A. A. S., and DeJong, M. (2021a). Fiber optic sensing of concrete cracking and rebar deformation using several types of cable. *Structural Control and Health Monitoring*, 28.

Zhang, Y., Zhang, Y., Yang, L., Liu, G., Chen, Y., Yu, S., and Du, H. (2021b). Hardened properties and durability of large-scale 3d printed cement-based materials. *Materials and Structures*, 54(1):45.

Zhou, Y., Althoey, F., Alotaibi, B. S., Gamil, Y., and Iftikhar, B. (2023). An overview of recent advancements in fibre-reinforced 3d printing concrete. *Frontiers in Materials*, 10.

Zhu, B., Nematollahi, B., Pan, J., Zhang, Y., Zhou, Z., and Zhang, Y. (2021). 3d concrete printing of permanent formwork for concrete column construction. *Cement and Concrete Composites*, 121:104039.

Appendix A Design Calculation of Axial Load Resistance of Cast-in-Place Rectangular Column

Assumed Material Properties

The nominal axial load capacity is calculated assuming zero material safety factors. The maximum aggregate size of the concrete mixture used in this study is 5 mm.

Yield strength of reinforcement	$f_y = 475$ MPa
Concrete compressive strength	$f'_c = 60$ MPa
Concrete stress block factor	$\alpha_1 = 0.85 - 0.0015 f'_c$
Gross cross-sectional area	$A_g = 113\,916$ mm^2
Steel reinforcement area	$A_s = 400$ mm^2 (4–10M bars)

Axial Resistance Calculation

Concrete Contribution

$$P_{rc} = \alpha_1 \phi_c f'_c (A_g - A_s) \tag{A.1}$$

$$= 0.76(1.0)(60)(113916 - 400) \times 10^{-3} \tag{A.2}$$

$$= 5176 \text{ kN} \tag{A.3}$$

Steel Contribution

$$P_{rs} = \phi_s f_y A_s \tag{A.4}$$

$$= (1.0)(475)(400) \times 10^{-3} \tag{A.5}$$

$$= 190 \text{ kN} \tag{A.6}$$

Nominal Axial Resistance

$$P_{ro} = P_{rc} + P_{rs} \tag{A.7}$$

$$= 5176 + 190 \tag{A.8}$$

$$= 5366 \text{ kN} \tag{A.9}$$

Maximum Factored Axial Resistance According to CSA A23.3, the maximum usable concentric axial resistance is limited to

$$P_{r,\max} = 0.8 P_{ro} \tag{A.10}$$

$$= 0.8(5366) \tag{A.11}$$

$$= 4292 \text{ kN} \tag{A.12}$$

Summary

Quantity	Value
Concrete contribution, P_{rc}	5789 kN
Steel contribution, P_{rs}	190 kN
Nominal axial resistance, P_{ro}	5979 kN
Maximum axial resistance, $P_{r,\max}$	4783 kN

Appendix B Appendix 2: Design Calculation of Axial Load Resistance of Circular Cast-in-Place Column

The nominal axial load capacity is calculated assuming zero material safety factors. The maximum aggregate size of the concrete mixture used in this study is 5 mm.

Assumed Material Properties

Yield strength of reinforcement	$f_y = 475$ MPa
Concrete compressive strength	$f'_c = 60$ MPa
Concrete stress block factor	$\alpha_1 = 0.85 - 0.0015 f'_c$
Gross cross-sectional area	$A_g = 49\,087$ mm^2
Steel reinforcement area	$A_s = 600$ mm^2 (6–10M bars)

Concrete Contribution

$$P_{rc} = \alpha_1 \phi_c f'_c (A_g - A_s) \tag{B.1}$$

$$= 0.76(1.0)(60)(49087 - 600) \times 10^{-3} \tag{B.2}$$

$$= 2283 \text{ kN} \tag{B.3}$$

Steel Contribution

$$P_{rs} = \phi_s f_y A_s \tag{B.4}$$

$$= (1.0)(475)(600) \times 10^{-3} \tag{B.5}$$

$$= 285 \text{ kN} \tag{B.6}$$

Nominal Axial Resistance

$$P_{ro} = P_{rc} + P_{rs} \tag{B.7}$$

$$= 2283 + 285 \tag{B.8}$$

$$= 2569 \text{ kN} \qquad \text{(CSA A23.3 Cl. 10.10.4)} \tag{B.9}$$

Maximum Axial Resistance

$$P_{r,\max} = 0.8 P_{ro} \tag{B.10}$$

$$= 0.8(2569) \tag{B.11}$$

$$= 2055 \text{ kN} \qquad \text{(CSA A23.3 Cl. 10.10.4)} \tag{B.12}$$

Minimum Longitudinal Reinforcement

$$A_{s,\min} = 0.01 A_g \tag{B.13}$$

$$= 0.01(49087) \tag{B.14}$$

$$= 491 \text{ mm}^2 \qquad \text{(CSA A23.3 Cl. 10.9.1)} \tag{B.15}$$

Maximum Longitudinal Reinforcement

$$A_{s,\max} = 0.08 A_g \tag{B.16}$$

$$= 0.08(49087) \tag{B.17}$$

$$= 3927 \text{ mm}^2 \qquad \text{(CSA A23.3 Cl. 10.9.2)} \tag{B.18}$$

Minimum Number of Longitudinal Bars

$$n_{\min} = 6 \qquad \text{(CSA A23.3 Cl. 10.9.3)} \tag{B.19}$$

Minimum Bar Spacing

$$s = \min\left(1.4d_b,\ 1.4 \times \text{Aggregate Size},\ 30 \text{ mm}\right) \tag{B.20}$$

$$= 30 \text{ mm} \qquad \text{(CSA A23.3 Cl. 6.6.5.2)} \tag{B.21}$$

Maximum Tie (Spiral) Spacing

$$s_{\text{tie}} = \min\left(16D_b,\ 48d_b,\ D,\ 300 \text{ mm}\right) \tag{B.22}$$

$$= 180.8 \text{ mm} \qquad \text{(CSA A23.3 Cl. 7.6.5.2)} \tag{B.23}$$

Summary

Quantity	Value
Concrete contribution, P_{rc}	2283 kN
Steel contribution, P_{rs}	285 kN
Nominal axial resistance, P_{ro}	2569 kN
Maximum axial resistance, $P_{r,\max}$	2055 kN
Minimum reinforcement area	491 mm^2
Maximum reinforcement area	3927 mm^2
Minimum number of bars	6
Minimum bar spacing	30 mm
Maximum tie spacing	180.8 mm

Appendix C Stress – Strain response of Hydro-Stone Gypsum Cement

Three 75 mm diameter cylinders, 150 mm high, were moulded with Hydrostone cement (properly known as USG Hydro-Stone Gypsum Cement). Strain gauges were attached to the opposite sides of the cylinders at the mid-height, and the cylinders were tested under axial compression at a displacement rate of 0.12 mm/min. The resulting average stress-strain response of the hydrostone cement is provided in Figure C.1.

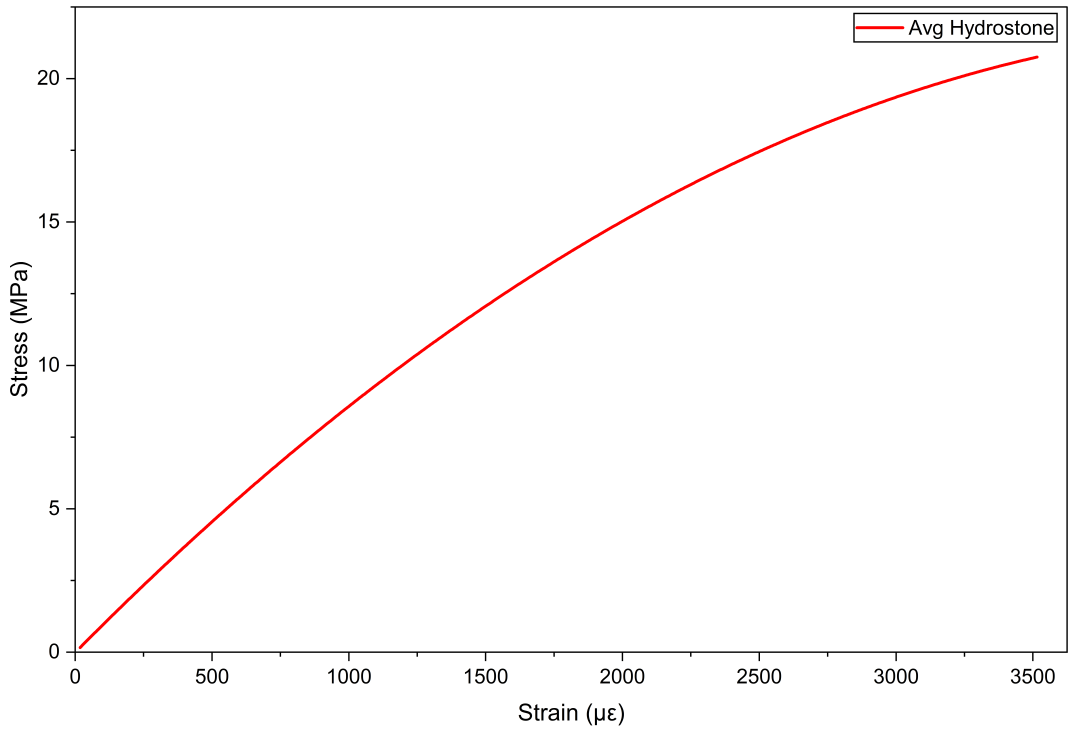


Figure C.1: Average stress - strain response of hydrostone cement cylinders

Appendix D Modified fibre section analysis for cast-in-place columns - MATLAB script

```
clear; clc; close all;
%  INPUT DATA AND DISPLACEMENT-TO-STRAIN TRANSFORMATION

% Experimental data is imported from an Excel file. The recorded
% potentiometer displacements are converted into axial strains
% using the corresponding gauge lengths.

[file, path] = uigetfile('*.xlsx;*.xls','Select Excel File');
fullpath = fullfile(path,file);

data = readtable(fullpath);

time    = data{:,1};
disp1   = data{:,2};
disp2   = data{:,3};
disp3   = data{:,4};
load_kN = data{:,5};

% Gauge locations and lengths
xg = [-175; 175; 0];
yg = [0; 0; 175];
Lg = [210; 210; 300];


%  CROSS-SECTION GEOMETRY DEFINITION

% The cross-section is defined as a square with rounded corners.
% This geometry is later used for fibre selection and visualisation.

B = 350; r = 100;
a = B/2;
c = a - r;

nArc = 60;
xb=[]; yb=[];

xb=[xb c -c]; yb=[yb a a];
```

```
th=linspace(pi/2,pi,nArc);
xb=[xb -c+r*cos(th)];
yb=[yb  c+r*sin(th)];

xb=[xb -a -a]; yb=[yb c -c];

th=linspace(pi,3*pi/2,nArc);
xb=[xb -c+r*cos(th)];
yb=[yb -c+r*sin(th)];

xb=[xb -c c]; yb=[yb -a -a];

th=linspace(3*pi/2,2*pi,nArc);
xb=[xb c+r*cos(th)];
yb=[yb -c+r*sin(th)];

xb=[xb a a]; yb=[yb -c c];

th=linspace(0,pi/2,nArc);
xb=[xb c+r*cos(th)];
yb=[yb c+r*sin(th)];

boundary=[xb(:),yb(:)];


%  FIBRE DISCRETIZATION APPROACH

% The cross-section is discretised into square fibres of uniform
% size. Only fibres located within the section boundary are retained.
% Regions occupied by reinforcing bars are excluded.

cellSize = 10;

xEdges=-a:cellSize:a-cellSize;
yEdges=-a:cellSize:a-cellSize;

[Xc,Yc]=meshgrid(xEdges+cellSize/2,yEdges+cellSize/2);
centers=[Xc(:) Yc(:)];

in=inpolygon(centers(:,1),centers(:,2),boundary(:,1),boundary(:,2));
inside=centers(in,:);

%% Reinforcement layout
barX = [-85 85 -85 85]';
```

```
barY = [ 85 85 -85 -85]';
barA = 100;
nBars = length(barX);
barArea = barA*ones(nBars,1);

% Remove fibres overlapping reinforcement
exclude=false(size(inside,1),1);
for i=1:nBars
    rb=sqrt(barA/pi);
    dx=inside(:,1)-barX(i);
    dy=inside(:,2)-barY(i);
    exclude = exclude | (dx.^2 + dy.^2 <= rb^2);
end

conc = inside(~exclude,:);
meshA = cellSize^2;

%  MATERIAL MODELS

% Concrete: nonlinear compressive model based on experimental fit
% with stress plateau beyond peak strain.
% Steel: elastic{perfectly plastic behaviour.

fc = 58.57;
e0 = 0.00244;

Es = 206000;
fy = 475;
%  PREALLOCATION

n = length(time);

Fc=zeros(n,1);
Fs=zeros(n,1);
Ftot=zeros(n,1);

Mx=zeros(n,1);
My=zeros(n,1);

steelStrain=zeros(n,nBars);
avgDef=zeros(n,1);

A=[ones(size(xg)) xg yg];
maxCoef=[0 0 0];
```

```
%  STRAIN COMPATIBILITY AND SECTION ANALYSIS

% A linear strain field is assumed across the section:
% ε = ε0 + κx·x + κy·y
% The coefficients are obtained from measured strains at gauges.
% Stresses are computed at each fibre and integrated to obtain
% resultant forces and moments.

for i=1:n

    % Convert displacement to strain
    u=[disp1(i);disp2(i);disp3(i)];
    eps=u./Lg;

    % Solve for strain plane
    if rank(A)==3
        coef=A\eps;
    else
        coef=[mean(eps);0;0];
    end

    % Strains
    strainC = coef(1)+coef(2)*conc(:,1)+coef(3)*conc(:,2);
    strainS = coef(1)+coef(2)*barX+coef(3)*barY;

    %% Concrete response
    sigC=zeros(size(strainC));
    comp=strainC<0;
    epsC=-strainC(comp);

    sigC(comp)= -7575125*epsC.^2 -42838*epsC;
    sigC(comp & (-strainC>e0))=-fc;

    %% Steel response
    sigS=Es*strainS;
    sigS=max(min(sigS,fy),-fy);

    %% FORCE AND MOMENT INTEGRATION
    Fc(i)=sum(sigC)*meshA;
    Fs(i)=sum(sigS.*barArea);
    Ftot(i)=Fc(i)+Fs(i);

    Mx(i)=sum(sigC.*meshA.*(conc(:,2)/1e6)) + ...
          sum(sigS.*barArea.*(barY/1e6));
```

```
    My(i)=sum(sigC.*meshA.*(conc(:,1)/1e6)) + ...
          sum(sigS.*barArea.*(barX/1e6));

    avgDef(i)=mean(u);
    steelStrain(i,:)=strainS';

    % Store strain state at peak load
    if load_kN(i)==max(load_kN)
        maxCoef=coef;
    end
end

%  EXTRACTION OF LOADING BRANCH

% Only the monotonic loading portion (up to peak load) is retained.

[~,id]=max(load_kN);
idx=1:id;

time=time(idx);
load_kN=load_kN(idx);

Fc=Fc(idx)/1000;
Fs=Fs(idx)/1000;
Ftot=Ftot(idx)/1000;

Mx=Mx(idx);
My=My(idx);

steelStrain=steelStrain(idx,:);
avgDef=avgDef(idx);

%  STRAIN CONTOUR VISUALIZATION

% The strain field at peak load is reconstructed and plotted
% over the cross-section.

xx=linspace(-a,a,250);
yy=linspace(-a,a,250);
[XX,YY]=meshgrid(xx,yy);

ZZ=maxCoef(1)+maxCoef(2)*XX+maxCoef(3)*YY;

mask=inpolygon(XX,YY,boundary(:,1),boundary(:,2));
ZZ(~mask)=NaN;
```

```
%% GLOBAL RESPONSE PLOTS

figure('Color','w','Position',[100 100 1600 900]);
tiledlayout(2,3,'Padding','compact','TileSpacing','compact');

nexttile;
plot(-avgDef,load_kN); hold on;
plot(-avgDef,-Ftot);
title('Load{Displacement'); grid on;

nexttile;
plot(-avgDef,Mx);
title('Mx'); grid on;

nexttile;
plot(-avgDef,My);
title('My'); grid on;

nexttile;
plot(time,-Fc); hold on;
plot(time,-Fs);
plot(time,-Ftot,'k--');
title('Force Contribution');
legend('Concrete','Steel','Total');
grid on;

nexttile;
for i=1:nBars
    plot(time,steelStrain(:,i)*1e6,'LineWidth',1.2);
    hold on;
end
title('Rebar Strains (με)');
grid on;

%% STRAIN MAP
figure('Color','w','Position',[300 100 900 900]);
contourf(XX,YY,ZZ,40,'LineColor','none');
colormap(turbo);
colorbar;
hold on;

plot(boundary(:,1),boundary(:,2),'k','LineWidth',2);

axis equal;
```

```
title('Strain Map');
grid on;
```

Appendix E Modified fibre section analysis for 47PC printed columns - MATLAB script

```
clear; clc; close all;
% INPUT DATA AND DISPLACEMENT-TO-STRAIN TRANSFORMATION
% Experimental measurements (time, displacements, load) are imported.
% Measured displacements are converted into axial strains using
% known gauge lengths and positions.

[filename, pathname] = uigetfile('*.xlsx;*.xls', ...
    'Select Excel file with time, displacements, load');

fullpath = fullfile(pathname, filename);
fprintf('Loading: %s\n', fullpath);

outputFolder = pathname;
[~, baseName, ~] = fileparts(fullpath);

data = readmatrix(fullpath);

time    = data(:,1);
u_left  = data(:,2);
u_right = data(:,3);
u_back  = data(:,4);
load_exp = data(:,5);

nSteps = length(time);

Lg = [210; 210; 300];
x_gauge = [-175; 175; 0];
y_gauge = [0; 0; 175];


% MATERIAL PROPERTIES AND CONSTITUTIVE MODELS

% Printed concrete: stress{strain response obtained from experimental data.
% Infill concrete: nonlinear compressive model with peak stress plateau.
% Steel: elastic{perfectly plastic behaviour.

fc_3dpc = 36.41;
```

```
e0_3dpc = 0.002156558;

fc_infill = 58.5709;
e0_infill = 0.002441407;

Es = 206000;
fy = 475;

[file_mat, path_mat] = uigetfile('*.xlsx;*.xls', ...
    'Select Printed Concrete Stress-Strain File');

if isequal(file_mat,0)
    error('No material file selected');
end

matData = readmatrix(fullfile(path_mat, file_mat));
strain_mat = matData(:,1);
stress_mat = matData(:,2);


% CROSS-SECTION GEOMETRY DEFINITION

% The section consists of an outer printed shell and an inner infill core,
% defined using an offset geometry.

B = 350;
a = B/2;

r = 100;
c = a - r;

offset = 50;

cellSize = 10;
meshArea = cellSize^2;

barX = [-85; 85; -85; 85];
barY = [-85; -85; 85; 85];
barArea = 100 * ones(size(barX));

nArc = 80;

%% Outer boundary definition
xb_outer = [c, -c, ...
    (-c + r*cos(linspace(pi/2,pi,nArc))), ...
```

```
    -a, -a, ...
    (-c + r*cos(linspace(pi,3*pi/2,nArc))), ...
    -c, c, ...
    (c + r*cos(linspace(3*pi/2,2*pi,nArc))), ...
    a, a, ...
    (c + r*cos(linspace(0,pi/2,nArc)))];

yb_outer = [a, a, ...
    (c + r*sin(linspace(pi/2,pi,nArc))), ...
    c, -c, ...
    (-c + r*sin(linspace(pi,3*pi/2,nArc))), ...
    -a, -a, ...
    (-c + r*sin(linspace(3*pi/2,2*pi,nArc))), ...
    -c, c, ...
    (c + r*sin(linspace(0,pi/2,nArc)))];

boundary_outer = [xb_outer(:), yb_outer(:)];

%% Inner boundary via geometric offset
outerPoly = polyshape(boundary_outer(:,1), boundary_outer(:,2));
innerPoly = polybuffer(outerPoly, -offset);

[xb_inner, yb_inner] = boundary(innerPoly);
boundary_inner = [xb_inner, yb_inner];
boundary_inner = unique(boundary_inner, 'rows', 'stable');

% FIBRE DISCRETIZATION APPROACH
% The cross-section is discretized into square fibres. Fibres are
% classified into printed shell and infill regions. Fibres overlapping
% reinforcement are removed.

xEdges = -a:cellSize:a-cellSize;
yEdges = -a:cellSize:a-cellSize;

[xC, yC] = meshgrid(xEdges + cellSize/2);
centers = [xC(:), yC(:)];

in_outer = inpolygon(centers(:,1),centers(:,2),boundary_outer(:,1),boundary_outer(:,2));
in_inner = inpolygon(centers(:,1),centers(:,2),boundary_inner(:,1),boundary_inner(:,2));

printedCenters = centers(in_outer & ~in_inner,:);
infillCenters  = centers(in_inner,:);

exclude_p = false(size(printedCenters,1),1);
exclude_i = false(size(infillCenters,1),1);
```

```
for i = 1:length(barX)
    rb = sqrt(barArea(i)/pi);

    dp = printedCenters - [barX(i), barY(i)];
    di = infillCenters  - [barX(i), barY(i)];

    exclude_p = exclude_p | (dp(:,1).^2 + dp(:,2).^2 <= rb^2);
    exclude_i = exclude_i | (di(:,1).^2 + di(:,2).^2 <= rb^2);
end

printedCenters = printedCenters(~exclude_p,:);
infillCenters  = infillCenters(~exclude_i,:);

% STRAIN COMPATIBILITY ASSUMPTION
% A linear strain field is assumed across the section:
% ε = ε0 + κx·x + κy·y
% The strain field is determined from measured gauge strains.

fprintf('Running analysis...\n');

resistance_history = zeros(nSteps,1);
disp_avg_history   = zeros(nSteps,1);
Mx_plot = zeros(nSteps,1);
My_plot = zeros(nSteps,1);

for t = 1:nSteps

    u = [u_left(t); u_right(t); u_back(t)];
    eps_m = u ./ Lg;

    A = [ones(size(x_gauge)) x_gauge y_gauge];
    coef = A \ eps_m;

    strain_p = coef(1) + coef(2)*printedCenters(:,1) + coef(3)*printedCenters(:,2);
    strain_i = coef(1) + coef(2)*infillCenters(:,1)  + coef(3)*infillCenters(:,2);
    strain_s = coef(1) + coef(2)*barX + coef(3)*barY;

    %% Concrete and steel constitutive response

    % Printed concrete (experimental curve)
    sig_p = zeros(size(strain_p));
    comp = strain_p < 0;
    ep = strain_p(comp);
```

```
    % the material constitutive model for the printed concrete was provided
    sig_temp = interp1(strain_mat, stress_mat, ep, 'linear','extrap');
    sig_temp(-ep > e0_3dpc) = -fc_3dpc;
    sig_p(comp) = sig_temp;

    % Infill concrete (nonlinear model)
    sig_i = zeros(size(strain_i));
    comp_i = strain_i < 0;
    ei = strain_i(comp_i);

    % the stress-strain response of infill concrete was obtained experimentally through c
    sig_i(comp_i) = -(-7575125.27*ei.^2 - 42838.85*ei);
    sig_i(strain_i > 0) = 0;
    sig_i(-strain_i > e0_infill) = -fc_infill;

    % Steel (elastic-perfectly plastic)
    sig_s = Es * strain_s;
    sig_s = max(min(sig_s,fy),-fy);

    %% Force and moment integration

    Fp = sig_p * meshArea;
    Fi = sig_i * meshArea;
    Fs = sig_s .* barArea;

    resistance_history(t) = (sum(Fp)+sum(Fi)+sum(Fs))/1000;

    disp_avg_history(t) = mean(eps_m)*210;

    Mx_plot(t) = ((sum(Fp .* (printedCenters(:,2)/1000)) + ...
                  sum(Fi .* (infillCenters(:,2)/1000)) + ...
                  sum(Fs .* (barY/1000))) / 1e3)/1000;

    My_plot(t) = ((sum(Fp .* (printedCenters(:,1)/1000)) + ...
                  sum(Fi .* (infillCenters(:,1)/1000)) + ...
                  sum(Fs .* (barX/1000))) / 1e3)/1000;
end


% EXTRACTION OF LOADING BRANCH
% Only the monotonic loading portion up to peak load is considered.

[~, peakIdx] = max(load_exp);

% STRAIN CONTOUR VISUALIZATION
```

```
% The strain field at peak load is reconstructed and plotted
% over the cross-section.

u_peak = [u_left(peakIdx); u_right(peakIdx); u_back(peakIdx)];
eps_peak = u_peak ./ Lg;

A = [ones(size(x_gauge)) x_gauge y_gauge];
coef_peak = A \ eps_peak;

xx = linspace(-a, a, 300);
yy = linspace(-a, a, 300);
[XX, YY] = meshgrid(xx, yy);

ZZ = coef_peak(1) + coef_peak(2)*XX + coef_peak(3)*YY;

mask_outer = inpolygon(XX, YY, boundary_outer(:,1), boundary_outer(:,2));
ZZ(~mask_outer) = NaN;

%% Plot results

keepIdx = 1:peakIdx;

figure;
plot(-disp_avg_history(keepIdx), load_exp(keepIdx),'LineWidth',1.5); hold on;
plot(-disp_avg_history(keepIdx), -resistance_history(keepIdx),'LineWidth',1.5);
xlabel('Disp (mm)'); ylabel('Load (kN)');
legend('Exp','Model'); grid on;

figure;
contourf(XX,YY,ZZ,40,'LineColor','none');
colormap(turbo); colorbar; hold on;
plot(boundary_outer(:,1),boundary_outer(:,2),'k','LineWidth',2);
plot(boundary_inner(:,1),boundary_inner(:,2),'r--','LineWidth',1.5);
scatter(barX,barY,40,'k','filled');
axis equal;
```

Appendix F Modified fibre section analysis for 60PC printed columns - MATLAB script

```
clear; clc; close all;

%% FILE SELECTION
% Select the Excel file containing the experimental displacement/load data.
[filename, pathname] = uigetfile('*.xlsx;*.xls', ...
    'Select displacement/load Excel file');
if isequal(filename,0)
    return;
end

fullpath = fullfile(pathname, filename);
fprintf('Loading data from:\n%s\n\n', fullpath);

%% OUTPUT NAMING
% Store the base file name for saving figures and results.
[~, baseName, ~] = fileparts(fullpath);
outputFolder = pathname;

%% READ EXPERIMENTAL DATA
% Import time, displacement, and load history from the selected file.
rawData = readtable(fullpath);

time    = rawData{:,1};
disp1   = rawData{:,2};
disp2   = rawData{:,3};
disp3   = rawData{:,4};
load_kN = rawData{:,5};

% Gauge geometry used to convert measured displacements to strain.
Lg = [210; 210; 300];
x_gauges = [-175; 175; 0];
y_gauges = [0; 0; 175];
A_gauge = [ones(size(x_gauges)), x_gauges, y_gauges];

% Section dimensions and mesh parameters.
W  = 350;
H  = 350;
```

```
Rf = 100;
slot_w = 100;
slot_h = 250;
gap = 50;

cellSize = 10;
meshArea = cellSize^2;

a = W/2;
r = Rf;

%% OUTER FILLETED BOUNDARY
% Define the perimeter of the outer section using four filleted corners.
c1 = [ W/2-r,  H/2-r];
c2 = [-W/2+r,  H/2-r];
c3 = [-W/2+r, -H/2+r];
c4 = [ W/2-r, -H/2+r];

x = [];
y = [];

t1 = linspace(3*pi/2, 2*pi, 100);
x = [x, c4(1) + r*cos(t1)];
y = [y, c4(2) + r*sin(t1)];

t2 = linspace(0, pi/2, 100);
x = [x, c1(1) + r*cos(t2)];
y = [y, c1(2) + r*sin(t2)];

t3 = linspace(pi/2, pi, 100);
x = [x, c2(1) + r*cos(t3)];
y = [y, c2(2) + r*sin(t3)];

t4 = linspace(pi, 3*pi/2, 100);
x = [x, c3(1) + r*cos(t4)];
y = [y, c3(2) + r*sin(t4)];

x(end+1) = x(1);
y(end+1) = y(1);

boundary_outer = [x(:), y(:)];

%% SLOT BOUNDARIES
% Define the two internal slot regions that represent the infilled zones.
slot_r = slot_w/2;
```

```
straight = slot_h - 2*slot_r;

theta_top = linspace(pi,0,80);
theta_bot = linspace(0,pi,80);

x_left  = -(gap/2 + slot_w/2);
x_right =  (gap/2 + slot_w/2);

make_slot = @(xc) deal( ...
    [xc + slot_r*cos(theta_top), ...
     xc + slot_r*ones(1,80), ...
     xc + slot_r*cos(theta_bot), ...
     xc - slot_r*ones(1,80)], ...
    [straight/2 + slot_r*sin(theta_top), ...
     linspace(straight/2,-straight/2,80), ...
     -straight/2 - slot_r*sin(theta_bot), ...
     linspace(-straight/2,straight/2,80)] );

[XL,YL] = make_slot(x_left);
[XR,YR] = make_slot(x_right);

boundary_left_slot  = [XL(:), YL(:)];
boundary_right_slot = [XR(:), YR(:)];

%% FIBRE MESH GENERATION
% Generate a uniform fibre mesh over the full section.
xEdges = -a:cellSize:a-cellSize;
yEdges = -a:cellSize:a-cellSize;

xC = xEdges + cellSize/2;
yC = yEdges + cellSize/2;
[Xc, Yc] = meshgrid(xC, yC);
centers = [Xc(:), Yc(:)];

%% MATERIAL PROPERTIES
% Printed concrete uses an experimental stress-strain curve.
% Infill concrete uses a nonlinear compressive model.
% Steel is modeled as elastic-perfectly plastic.

fc_infill = 58.5709;
e0_infill = 0.002441407;
Es = 206000;
fy = 475;

%% IMPORT PRINTED CONCRETE MATERIAL CURVE
```

```
% Read and sort the stress-strain data for interpolation.
[file_p, path_p] = uigetfile('*.xlsx;*.xls', ...
    'Select PRINTED concrete stress-strain file');
if isequal(file_p,0)
    return;
end

mat_p = readmatrix(fullfile(path_p, file_p));
strain_p = mat_p(:,1);
stress_p = mat_p(:,2);

[strain_p, idx] = sort(strain_p);
stress_p = stress_p(idx);

sigma_3dpc_fun = @(eps) interp1( ...
    strain_p, stress_p, eps, ...
    'linear', 'extrap');

%% REINFORCEMENT LAYOUT
% Define the bar locations and corresponding bar areas.
barX = [-85; 85; -85; 85];
barY = [-85; -85; 85; 85];
barA = 100;
barArea = barA * ones(size(barX));

%% REGION CLASSIFICATION
% Identify fibres that belong to the outer printed region and to the slots.
in_outer = inpolygon( ...
    centers(:,1), centers(:,2), ...
    boundary_outer(:,1), boundary_outer(:,2));

in_left_slot = inpolygon( ...
    centers(:,1), centers(:,2), ...
    boundary_left_slot(:,1), boundary_left_slot(:,2));

in_right_slot = inpolygon( ...
    centers(:,1), centers(:,2), ...
    boundary_right_slot(:,1), boundary_right_slot(:,2));

in_slots = in_left_slot | in_right_slot;

concrete3DPCCenters = centers(in_outer & ~in_slots, :);
concreteInfillCenters = centers(in_outer & in_slots, :);

%% REMOVE FIBRES OCCUPIED BY REBARS
```

```
% Exclude fibre centers that fall within the rebar cross-sectional area.
exclude_infill = false(size(concreteInfillCenters,1),1);

for i = 1:length(barX)
    rb = sqrt(barArea(i)/pi);
    dx = concreteInfillCenters(:,1) - barX(i);
    dy = concreteInfillCenters(:,2) - barY(i);
    exclude_infill = exclude_infill | ...
        ((dx.^2 + dy.^2) <= rb^2);
end

concreteInfillCenters = ...
    concreteInfillCenters(~exclude_infill,:);

%% PREPARE COORDINATES FOR ANALYSIS
% Store fibre and steel coordinates in both mm and m for moment calculations.
x_3dpc = concrete3DPCCenters(:,1);
y_3dpc = concrete3DPCCenters(:,2);
x_infill = concreteInfillCenters(:,1);
y_infill = concreteInfillCenters(:,2);

x_3dpc_m = x_3dpc/1000;
y_3dpc_m = y_3dpc/1000;
x_infill_m = x_infill/1000;
y_infill_m = y_infill/1000;
barX_m = barX/1000;
barY_m = barY/1000;

%% PREALLOCATION
% Allocate storage for force, deformation, and moment histories.
nSteps = length(time);

avgDeform = zeros(nSteps,1);
Mx_model  = zeros(nSteps,1);
My_model  = zeros(nSteps,1);
F_model   = zeros(nSteps,1);

F_3dpc_hist   = zeros(nSteps,1);
F_infill_hist = zeros(nSteps,1);
F_steel_hist  = zeros(nSteps,1);

maxLoad = -Inf;
maxLoadIdx = 1;
maxCoef = [0;0;0];
```

```
fprintf('Processing %d time steps...\n\n', nSteps);

%% SECTIONAL ANALYSIS LOOP
% Fit a linear strain plane from the measured gauge strains at each step.
% Then compute stresses in each fibre and integrate them to obtain
% axial resistance and bending moments.

for i = 1:nSteps
    %% Gauge strains
    % Convert measured displacements to strains using gauge lengths.
    u = [disp1(i); disp2(i); disp3(i)];
    eps_m = u ./ Lg;

    %% Plane strain coefficients
    % Solve for the linear strain field coefficients.
    if rank(A_gauge) == 3
        coef = A_gauge \ eps_m;
    else
        coef = [mean(eps_m); 0; 0];
    end

    %% Fibre strains
    % Evaluate the strain field at the printed concrete, infill concrete,
    % and reinforcement locations.
    strain_3dpc = ...
        coef(1) + coef(2)*x_3dpc + coef(3)*y_3dpc;

    strain_infill = ...
        coef(1) + coef(2)*x_infill + coef(3)*y_infill;

    strain_steel = ...
        coef(1) + coef(2)*barX + coef(3)*barY;

    %% Printed concrete stress
    % Use the interpolated experimental stress-strain relationship.
    sig_3dpc = sigma_3dpc_fun(strain_3dpc);

    %% Infill concrete stress
    % Use a nonlinear compressive model for the infill region.
    sig_infill = zeros(size(strain_infill));
    comp_infill = strain_infill < 0;
    epsc = -strain_infill(comp_infill);
    ratio = epsc / e0_infill;

    sig_infill(comp_infill) = ...
```

```
    -fc_infill .* (2*ratio - ratio.^2);

sig_infill(comp_infill & ...
    (-strain_infill > e0_infill)) = -fc_infill;

%% Steel stress
% Model reinforcement as elastic-perfectly plastic.
sig_steel = Es * strain_steel;
sig_steel = max(min(sig_steel, fy), -fy);

%% Force integration
% Integrate fibre stresses over the concrete and steel areas.
F_3dpc_vec   = sig_3dpc * meshArea;
F_infill_vec = sig_infill * meshArea;
F_steel_vec  = sig_steel .* barArea;

F_3dpc_total   = sum(F_3dpc_vec);
F_infill_total = sum(F_infill_vec);
F_steel_total  = sum(F_steel_vec);

totalResistance = ...
    F_3dpc_total + ...
    F_infill_total + ...
    F_steel_total;

F_3dpc_hist(i)   = F_3dpc_total/1000;
F_infill_hist(i) = F_infill_total/1000;
F_steel_hist(i)  = F_steel_total/1000;

%% Moment integration
% Compute moments about the global axes from the fibre force resultants.
Mx_model(i) = ...
    sum(F_3dpc_vec .* y_3dpc_m)/1e6 + ...
    sum(F_infill_vec .* y_infill_m)/1e6 + ...
    sum(F_steel_vec .* barY_m)/1e6;

My_model(i) = ...
    sum(F_3dpc_vec .* x_3dpc_m)/1e6 + ...
    sum(F_infill_vec .* x_infill_m)/1e6 + ...
    sum(F_steel_vec .* barX_m)/1e6;

%% Average deformation
avgDeform(i) = mean(u);

%% Total model resistance
```

```
    F_model(i) = totalResistance/1000;

    %% Peak load tracking
    % Store the strain state corresponding to the maximum experimental load.
    if load_kN(i) > maxLoad
        maxLoad = load_kN(i);
        maxLoadIdx = i;
        maxCoef = coef;
    end
end

%% PRINT PEAK CONTRIBUTIONS
% Report the individual force contributions at the peak experimental load.
fprintf('PEAK LOAD CONTRIBUTIONS\n');
fprintf('Peak Experimental Load : %.2f kN\n\n\n', ...
    load_kN(maxLoadIdx));
fprintf('3DPC Contribution      : %.2f kN\n', ...
    -F_3dpc_hist(maxLoadIdx));
fprintf('Infill Contribution    : %.2f kN\n', ...
    -F_infill_hist(maxLoadIdx));
fprintf('Steel Contribution     : %.2f kN\n', ...
    -F_steel_hist(maxLoadIdx));
fprintf('Total Model Resistance : %.2f kN\n', ...
    -F_model(maxLoadIdx));

%% EXTRACT LOADING BRANCH
% Retain only the response up to the peak experimental load.
[maxLoadExp, maxLoadExpIdx] = max(load_kN);

keepIdx = 1:maxLoadExpIdx;

time       = time(keepIdx);
avgDeform  = avgDeform(keepIdx);
load_kN    = load_kN(keepIdx);
F_model    = F_model(keepIdx);
Mx_model   = Mx_model(keepIdx);
My_model   = My_model(keepIdx);

%% STRAIN FIELD AT PEAK LOAD
% Reconstruct the strain distribution at the peak load for visualization.
xx = linspace(-a, a, 300);
yy = linspace(-a, a, 300);
[XX, YY] = meshgrid(xx, yy);

ZZ_max = ...
```

```
    maxCoef(1) + ...
    maxCoef(2)*XX + ...
    maxCoef(3)*YY;

mask = inpolygon( ...
    XX, YY, ...
    boundary_outer(:,1), ...
    boundary_outer(:,2));
ZZ_max(~mask) = NaN;

%% GLOBAL RESPONSE PLOTS
% Plot load-deformation and moment histories for the loading branch.
figMain = figure('Color','w', ...
    'Position', [100 100 1400 900]);

tiledlayout(2,3, ...
    'Padding','compact', ...
    'TileSpacing','compact');

nexttile;
hold on;
box on;
plot(-avgDeform, load_kN, ...
    'DisplayName', 'Experiment');
plot(-avgDeform, -F_model, ...
    'DisplayName', 'Fiber Model');
xlabel('Average Deformation (mm)');
ylabel('Load (kN)');
title('Load vs Average Deformation');
legend('Location', 'best');
grid on;

nexttile;
hold on;
box on;
plot(-avgDeform, Mx_model);
xlabel('Average Deformation (mm)');
ylabel('M_x (kN-m)');
title('Moment M_x vs Average Deformation');
grid on;

nexttile;
hold on;
box on;
plot(-avgDeform, My_model);
```

```
xlabel('Average Deformation (mm)');
ylabel('M_y (kN-m)');
title('Moment M_y vs Average Deformation');
grid on;

%% STRAIN MAP PLOT
% Display the peak-load strain contour with the section geometry and bars.
nexttile([1 2]);
hold on;
box on;

contourf(XX, YY, ZZ_max, ...
    40, 'LineColor', 'none');
colormap(turbo);
cb = colorbar;
cb.Label.String = 'Strain';

plot(boundary_outer(:,1), ...
     boundary_outer(:,2), ...
     'k-', 'LineWidth', 2);

plot(boundary_left_slot(:,1), ...
     boundary_left_slot(:,2), ...
     'r--', 'LineWidth', 1.5);

plot(boundary_right_slot(:,1), ...
     boundary_right_slot(:,2), ...
     'r--', 'LineWidth', 1.5);

%% Mesh overlay
% Draw the concrete fibre mesh inside the printed region.
for i = 1:size(concrete3DPCCenters,1)
    rectangle( ...
        'Position', ...
        [concrete3DPCCenters(i,1)-cellSize/2, ...
         concrete3DPCCenters(i,2)-cellSize/2, ...
         cellSize, cellSize], ...
        'EdgeColor', 'w', ...
        'LineWidth', 0.25);
end

%% Rebars
% Plot reinforcement bars at their centroid locations.
theta_bar = linspace(0,2*pi,100);
rb = sqrt(barA/pi);
```

```
for i = 1:length(barX)
    xb2 = barX(i) + rb*cos(theta_bar);
    yb2 = barY(i) + rb*sin(theta_bar);
    plot(xb2, yb2, ...
        'k-', 'LineWidth', 1.6);
end

scatter(barX, barY, ...
    40, 'k', 'filled');

xline(0, '--', ...
    'Color', [0.5 0.5 0.5]);
yline(0, '--', ...
    'Color', [0.5 0.5 0.5]);

axis equal;
xlim([-a a]);
ylim([-a a]);
xlabel('x (mm)');
ylabel('y (mm)');
title(sprintf( ...
    'Strain Map at Maximum Load (%.1f kN)', ...
    maxLoadExp));

sgtitle(sprintf( ...
    'Dual-Material Fiber Analysis - %s', ...
    filename), ...
    'Interpreter', 'none');

%% SAVE FIGURES AND RESULTS
% Save the main figure and export the response history to Excel.
print(figMain, '-dpng', '-r600', ...
    fullfile(outputFolder, ...
    [baseName, ...
    '_LoadDeformation_Moments_StrainMap.png']));

savefig(figMain, ...
    fullfile(outputFolder, ...
    [baseName, ...
    '_LoadDeformation_Moments_StrainMap.fig']));

resultsTable = table( ...
    time, abs(avgDeform), abs(load_kN), ...
    abs(F_model), Mx_model, My_model, ...
```

```
    'VariableNames', ...
    {'Time_s', ...
     'AvgDeform_mm', ...
     'LoadExp_kN', ...
     'LoadModel_kN', ...
     'Mx_kNm', ...
     'My_kNm'});

outputFile = strrep( ...
    fullpath, ...
    '.xlsx', ...
    '_dual_material_slots_only.xlsx');

writetable(resultsTable, outputFile);
fprintf('Results saved to:\n%s\n\n', outputFile);
```

Appendix G Potentiometer and load response of small circular columns

This appendix provides all data collected by the potentiometers attached to the small-scale circular columns, as well as the columns' axial load resistance. These plots show the strain gauge measurements for the small circular columns and the deviation of the readings at different load levels for each column.

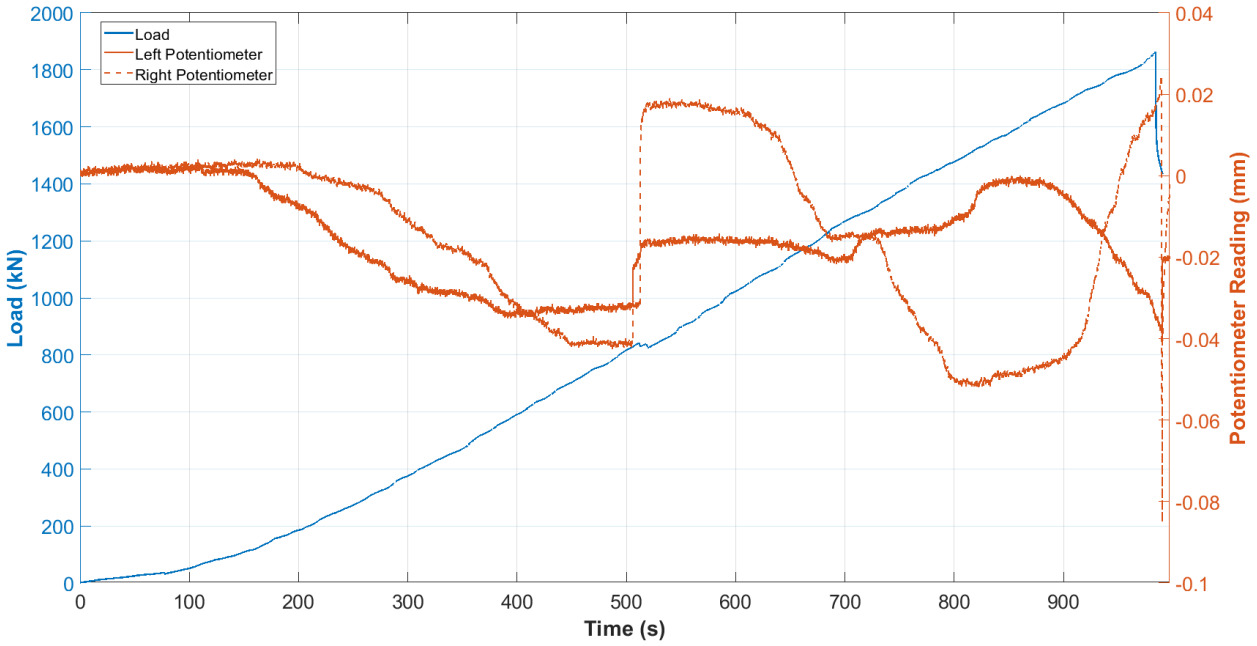


Figure G.1: Load and potentiometer response of cast-in-place column - specimen 3 (CCC1)

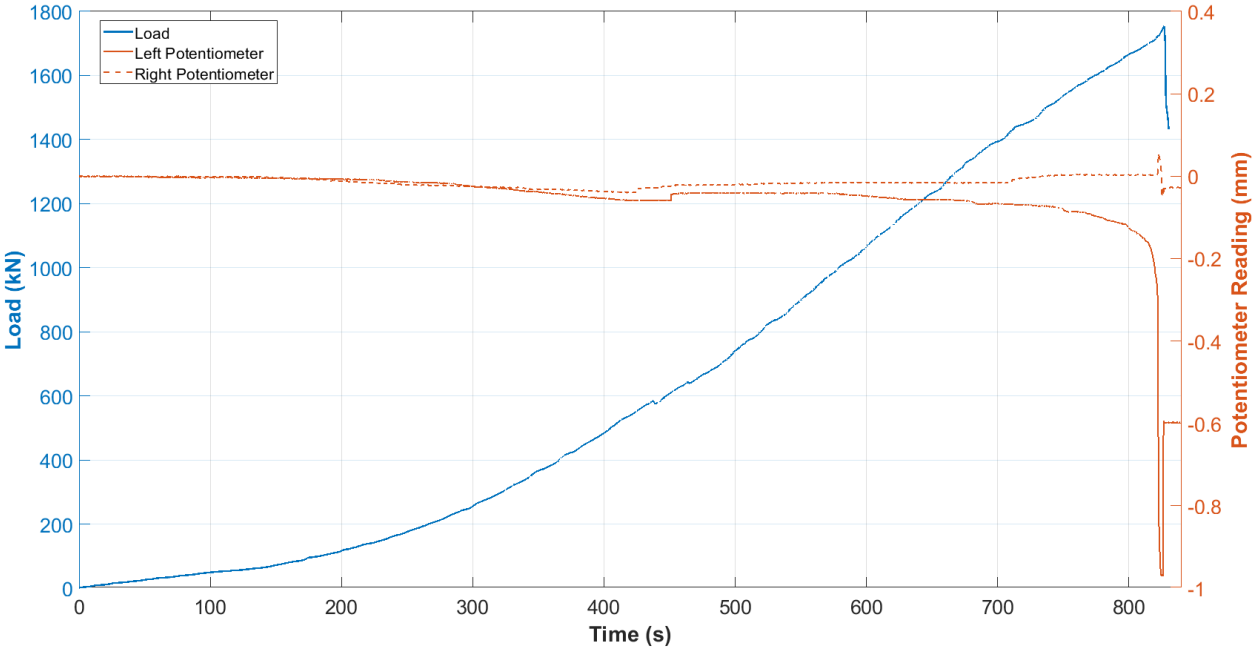


Figure G.2: Load and potentiometer response of cast-in-place column - specimen 2 (CCC2)

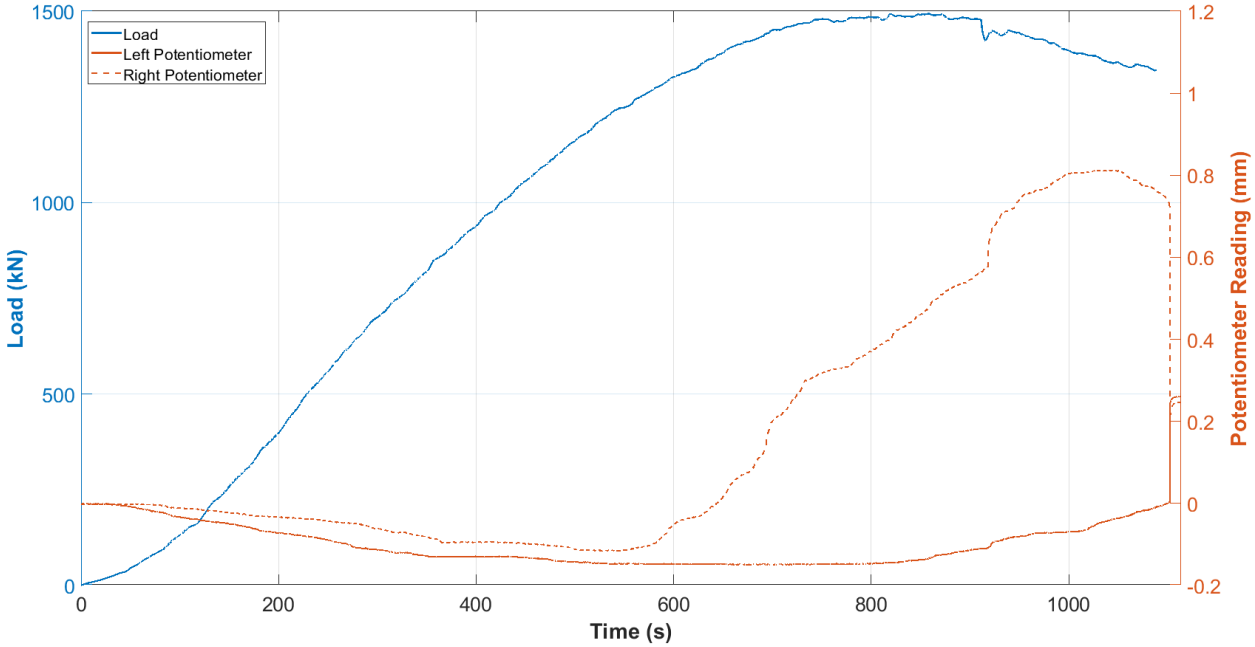


Figure G.3: Load and potentiometer response of cast-in-place column - specimen 1 (CCC3). This column was tested multiple times.

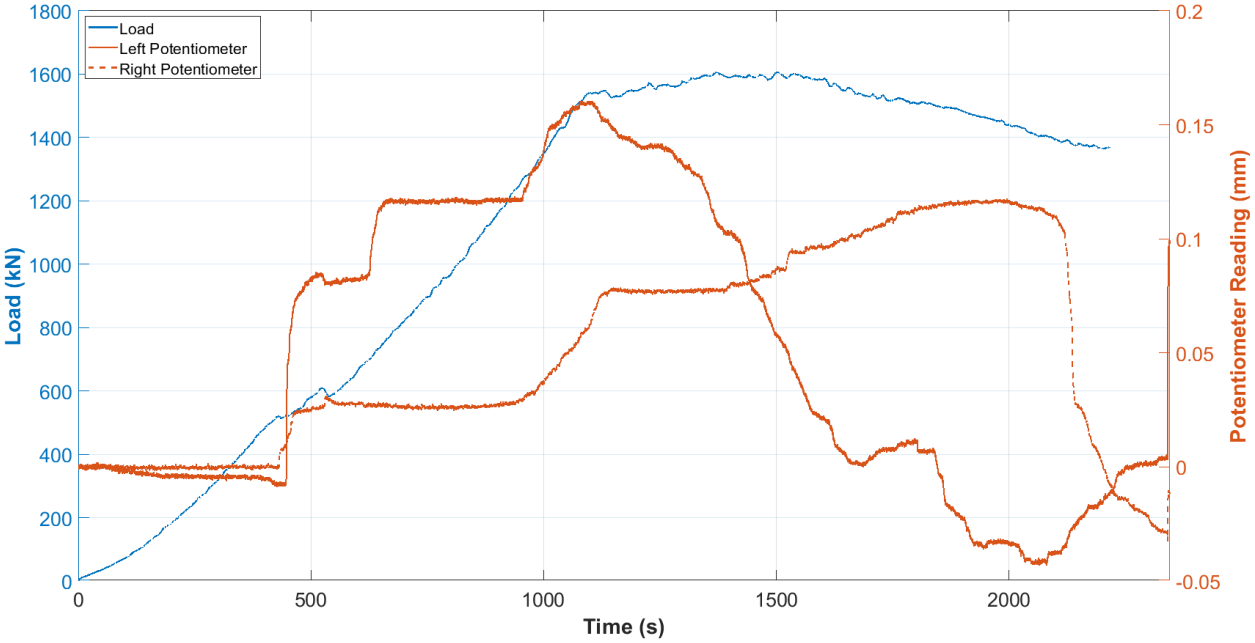


Figure G.4: Load and potentiometer response of 3D printed column - specimen 1 (3DPC1)

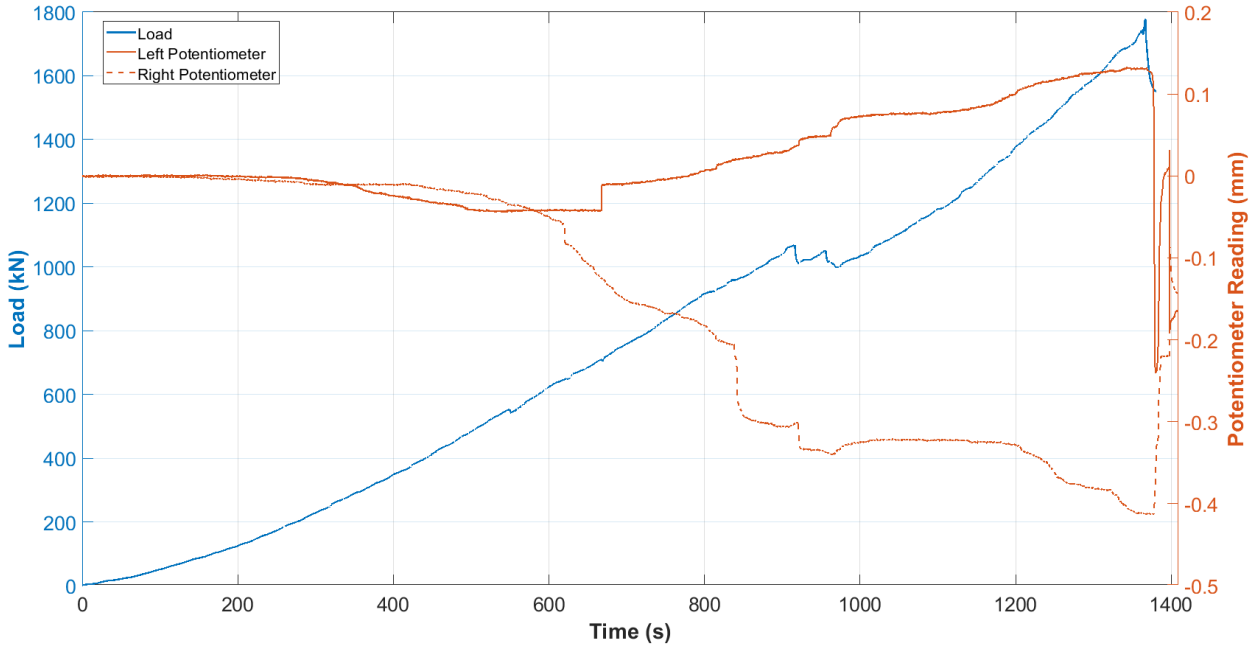


Figure G.5: Load and potentiometer response of 3D printed column - specimen 2 (3DPC2)

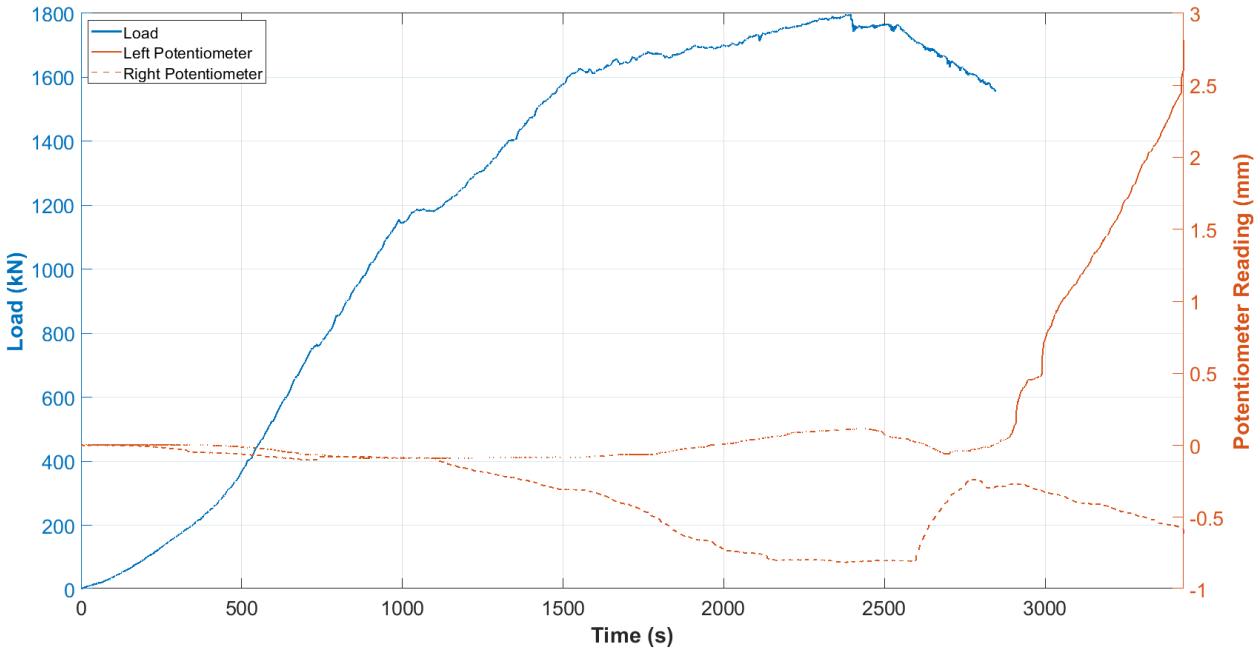


Figure G.6: Load and potentiometer response of 3D printed column - specimen 3 (3DPC3)